Minute-scale power forecasts of offshore wind farms based on long-range lidar measurements and turbine operational data

Frauke Theuer

Von der Fakultät für Mathematik und Naturwissenschaften
der Carl von Ossietzky Universität Oldenburg
zur Erlangung des Grades und Titels einer

DOKTORIN DER NATURWISSENSCHAFTEN
DR. RER. NAT.

angenommene Dissertation

von Frau Frauke Theresa Theuer
geboren in Osnabrück

Carl von Ossietzky
Universität
Oldenburg

Gutachter: Prof. Dr. Martin Kühn
Zweitgutachterin: Prof. Dr. Charlotte Bay Hasager
Tag der Disputation: 09.06.2022

Abstract

The share of renewable energies in the power system has been steadily increasing during the last years and is expected to further do so in the future. Hereby, offshore wind energy plays an important role. One main challenge of this energy transition is the high volatility of the feed-in from renewable sources such as wind and solar power, which can threaten grid stability and power system security. With regard to offshore wind, this effect is enhanced by the small geographical dispersion of large offshore wind farms.

In general, power forecasts are being used to support the balancing of supply and demand. In this context, the need for minute-scale forecasts is increasing. For such short lead times typically statistical methods are used. However, they fail during rare or extreme events, such as power ramps. These cases are of high interest for system security and electricity trading, which makes the accurate prediction of both amplitude and timing important. Recently, remote sensing-based methods have been investigated to extend the applicability of physical methods to shorter forecast horizons and to provide a competitive alternative to statistical approaches.

Therefore, the main objective of this thesis was the further development of probabilistic minute-scale power forecasts for offshore wind farms based on lidar measurements and turbine operational data. This was achieved by four main contributions. Firstly, a probabilistic forecasting methodology, previously developed for high-resolution dual-Doppler radar observations, was further extended to the specific requirements of single long-range lidar scans with lower spatial-temporal sampling. Its conceptual feasibility was demonstrated using measurements from an offshore wind farm. Secondly, the forecast's uncertainty, in particular related to height extrapolation of wind speed and atmospheric stability, was characterized. Forecast skill was improved by several enhancements of the initial approach, e. g. by incorporating turbine measurements or hybrid methods. Thirdly, the forecast availability and skill for wake-influenced turbines in a large wind farm were increased by combing lidar measurements and high-frequency operational data to an observer-based forecast. Finally, the forecasts of individual wind turbines were aggregated to a probabilistic forecast of the wind farm power using a copula approach.

It can be concluded that probabilistic power forecasts based on single-Doppler lidar scans have the potential to outperform the statistical benchmark persistence during unstable stratification and provide a more feasible alternative to radar-based approaches. Moreover, wind turbine operational data can strongly benefit forecast skill: Firstly, when considered in the lidar-based forecast to reduce uncertainties related to wind speed extrapolation. Secondly, when extending lidar-based forecasts to observer-based forecasts by integrating SCADA-based forecasts. And thirdly, when combined with observer-based forecasts in a hybrid approach. In general, forecast skill and availability were found to be strongly dependent on turbine location, this includes a dependency on wake exposure, and on lidar trajectories. One main result was the differentiation of forecast skill and superiority over persistence during different atmospheric conditions, characterized by atmospheric stability, turbulence intensity and wind speed increments. This suggests a high value of lidar-based approaches in particular during ramp events and provides an important basis for decision-making by end-users.

Future work needs to aim at increasing lidar data availability, for instance, by further developing lidar devices or improving trajectories. Such measures would also enhance forecast skill and horizon. Further, forecasts need to be developed methodological in particular with regard to wind vector propagation and wake effects. And finally, they need to be embedded into existing decision-making processes used for electricity trading and power system balancing.

Zusammenfassung

Der Anteil der erneuerbaren Energien im Stromnetz ist in den letzten Jahren stetig gestiegen und wird voraussichtlich auch in Zukunft weiter steigen. Dabei spielt die Offshore-Windenergie eine wichtige Rolle. Eine große Herausforderung dieser Energiewende ist die hohe Volatilität der Einspeisung aus erneuerbaren Quellen wie Wind- und Solarenergie, die die Netzstabilität und die Sicherheit des Stromsystems gefährden kann. Bei der Offshore-Windenergie wird dieser Effekt durch die geringe geografische Streuung großer Offshore-Windparks noch verstärkt.

Im Allgemeinen werden Leistungsprognosen genutzt, um den Ausgleich von Einspeisung und Verbrauch zu unterstützen. In diesem Zusammenhang steigt der Bedarf an Prognosen im Minutenbereich. Für solche kurzen Vorhersagehorizonte werden in der Regel statistische Methoden verwendet. Diese versagen jedoch bei seltenen oder extremen Ereignissen, wie z. B. Leistungsrampen. Diese Fälle sind für die Systemsicherheit und den Stromhandel von großem Interesse, weshalb eine genaue Vorhersage sowohl ihrer Amplitude als auch des Zeitpunkts ihres Eintreffens wichtig ist. In letzter Zeit wurden Methoden basierend auf Fernerkundungsverfahren untersucht, um die Anwendbarkeit physikalischer Methoden auf kürzere Vorhersagehorizonte zu erweitern und eine wettbewerbsfähige Alternative zu statistischen Ansätzen zu entwickeln.

Das Hauptziel dieser Arbeit war daher die Weiterentwicklung von probabilistischen Kürzestfrist-Leistungsprognosen für Offshore-Windparks auf Basis von Lidarmessungen und Betriebsdaten von Turbinen. Dies wurde durch vier Hauptbeiträge erreicht. Erstens wurde eine probabilistische Prognosemethode, die zuvor für hochauflösende dual-Doppler Radarmessungen entwickelt worden war, auf die spezifischen Anforderungen von langreichweitigen single Lidarscans mit geringerer räumlich-zeitlicher Auflösung erweitert. Ihre konzeptionelle Umsetzbarkeit wurde anhand von Messungen in einem Offshore-Windpark demonstriert. Zweitens wurde die Unsicherheit der Vorhersage, insbesondere in Bezug auf die Höhenextrapolation der Windgeschwindigkeit und die atmosphärische Stabilität, charakterisiert. Die Vorhersagegenauigkeit wurde durch verschiedene Erweiterungen des ursprünglichen Ansatzes verbessert, z. B. durch das Einbeziehen von Turbinenmessungen

oder hybride Methoden. Drittens wurde die Vorhersageverfügbarkeit und -genauigkeit für vom Nachlauf beeinflusste Turbinen in einem großen Windpark durch die Kombination von Lidarmessungen und hochfrequenten Betriebsdaten zu einer beobachterbasierten Vorhersage erhöht. Schließlich wurden die Vorhersagen für einzelne Windturbinen mit Hilfe eines Copula-Ansatzes zu einer probabilistischen Vorhersage der Windparkleistung aggregiert.

Es kann geschlussfolgert werden, dass probabilistische Leistungsvorhersagen, die auf single-Doppler Lidarscans basieren, das Potenzial haben, die statistische Benchmark Persistenz während instabiler Schichtung zu übertreffen und eine praktikablere Alternative zu Radar-basierten Ansätzen darstellen. Darüber hinaus können Betriebsdaten von Windenergieanlagen die Vorhersagegenauigkeit erheblich verbessern: Erstens wenn sie in den Lidar-basierten Vorhersagen berücksichtigt werden, um Unsicherheiten im Zusammenhang mit der Höhenextrapolation der Windgeschwindigkeit zu verringern. Zweitens wenn Lidar-basierte Vorhersagen durch die Intergrierung von SCADA-basierten Vorhersagen zu beobachtergestützten Vorhersagen erweitert werden. Und drittens bei der Kombination mit beobachtergestützten Prognosen in einem hybriden Ansatz. Im Allgemeinen wurde festgestellt, dass die Vorhersagegenauigkeit und -verfügbarkeit stark vom Standort der Turbine, das schließt eine Abhängigkeit von der Beeinflussung durch Nachläufe ein, und den Lidar-Trajektorien abhängt. Eines der Hauptergebnisse war die Differenzierung der Vorhersagegenauigkeit und der Überlegenheit gegenüber der Persistenz während verschiedener atmosphärischer Bedingungen, gekennzeichnet durch atmosphärische Stabilität, Turbulenzintensität und Windgeschwindigkeitsinkremente. Dies deutet auf den hohen Wert von Lidar-basierten Ansätzen insbesondere während Rampenereignissen hin und stellt eine wichtige Grundlage für die Entscheidungsfindung der Endnutzer/innen dar.

Zukünftige Forschung muss darauf abzielen, die Datenverfügbarkeit der Lidargeräte zu verbessern, z. B. durch die Weiterentwicklung von Lidar-Geräten oder die Verbesserung von Messtrajektorien. Außerdem müssen die Vorhersagen methodisch weiterentwickelt werden, insbesondere im Hinblick auf die Advektion von Windvektoren und Nachlaufeffekte. Und schließlich müssen sie in bestehende Entscheidungsprozesse eingebettet werden, die für den Stromhandel und den Ausgleich im Stromsystem genutzt werden.

Contents

List of Figures

List of Tables

List of Abbreviations

Abbreviation	**Definition**
ANN	Artifical Neural Networks
AoI	Area of Influence
ARIMA	Autoregressive Integrated Moving Average
ARMA	Autoregressive Moving Average
CNN	Convolutional Neural Network
CNR	Carrier-to-Noise Ratio
crps	continuous ranked probability score
DBU	Deutsche Bundesstiftung Umwelt
DLR	Deutsches Zentrum für Luft- und Raumfahrt
DCNN	Deep Convolutional Neural Network
EMOS	Ensemble Model Output Statistics
GT I	Global Tech I
IEC	International Electrotechnical Commission
LF	Lidar-based forecast
Lidar	Light detection and ranging
LOS	Line-of-sight
MAE/mae	Mean Absolute Error
MOS	Model Output Statistics
MOST	Monin Obukhov Similarity Theory
NWP	Numerical Weather Prediction
OF	Observer-based forecast
OSTIA	Operational Sea Surface Temperature and Sea Ice Analysis

OWP	Offshore Windpark
PF	Profile fit-based forecast
PPI	Plan Position Indicator
Radar	Radio detection and ranging
RE	Renewable Energies
RHI	Range Height Indicator
RMSE/rmse	Root-Mean-Squared Error
SCADA	Supervisory Control and Data Acquisition
SF	SCADA-based forecast
SST	Sea Surface Temperature
SVM	Support Vector Machines
T	Turbine
TDF	Temperature difference-based forecast
TF	Tendency-based forecast
TI	turbulence intensity
TP	Transition piece
TSO	Transmission System Operator
UTC	Coordinated Universal Time
VAD	Velocity Azimuth Display
WIMS	Windenergierelevante Meteorologie- und Strömungsberechnungen
WRF	Weather Research and Forecasting Model

List of Symbols

Symbol	Description	Units
a	maximal number of propagation steps (Ch.2)	-
a	calibration parameter (Ch.4)	-
b	calibration parameter (Ch.4)	-
b	bin index for hybrid model (Ch.5)	-
Bias/bias	bias	variable dependent
c	calibration parameter	-
c_{ex}	height extrapolation factor	-
c_{h}	height extrapolation factor	-
$\overline{\mathrm{crps}}$	average continuous ranked probability score	variable dependent
$\overline{\mathrm{crps}}_{\mathrm{ref}}$	reference $\overline{\mathrm{crps}}$	variable dependent
crps ss	$\overline{\mathrm{crps}}$ skill score	variable dependent
C	copula function	-
d	calibration parameter	-
D	rotor diameter	m
f	truncated Gaussian distribution	-
fc	forecast	variable dependent
$\overline{\mathrm{fc}}$	ensemble mean	variable dependent
$\mathrm{fc}_{\mathrm{OF}}$	observer-based forecast generated	variable dependent
$\mathrm{fc}_{\mathrm{pers}}$	persistence forecast	variable dependent
$\mathrm{fc}_{\mathrm{weighting}}$	forecast generated using the weighting approach	variable dependent
fc_{σ^2}	variance of ensemble members	variable dependent
F	cumulative distribution function	-

g	gravitational acceleration	$\mathrm{m\,s^{-2}}$
h	turbine index	-
H	Heaviside step function	-
i	time index	-
i	index of variables contributing to uncertainty (Ch.3)	-
j	turbine index	-
J	calibration cost function (Ch.4)	-
J	weighting approach cost function (Ch.5)	-
k	forecast lead time	s
l	index of time steps for bias correction	-
L	Obukhov length	m
m	number of turbines	-
M	number of random samples from multivariate normal distribution	-
n	index of lidar scan	-
N	number of forecasts/ time steps	-
N	number of repetitions for Monte Carlo simulations (Ch.3)	-
N_t	number of time steps for bias correction	-
N_c	number of time steps for calibration	-
N_q	number of quantile steps	-
obs	observation	variable dependent
p	tuning parameter for weighting factor	-
P	power	W
P_r	wind turbine rated power	W
P_total	total wind farm power	W
q	index of quantile steps	-
quantile mae	quantile mean absolute error	-
r	range gate	m
$\mathrm{rmse_{ref}}$	reference rmse	variable dependent

rmse ss	rmse skill score	variable dependent
R_{AoI}	radius of area of influence	m
R^2	regression coefficient	-
Ri_{b}	bulk Richardson number	-
t	time	s
t_n	scan initialization time	s
t_{n}	length of Copula training data set	-
t_{syn}	synchronization time	s
T_{r}	measurement reset time	s
T_{tot}	total scanning duration	s
T_{v}	virtual temperature at sea level	K
T_ϑ	scan measuring time	s
u	horizontal wind speed (Ch.3)	$\mathrm{m\,s^{-1}}$
$u_{100\,\mathrm{m}}$	WRF wind speed at 100 m height	$\mathrm{m\,s^{-1}}$
u_{corr}	bias-corrected wind speed	$\mathrm{m\,s^{-1}}$
u_{h}	horizontal wind speed	$\mathrm{m\,s^{-1}}$
u_{hh}	wind speed at hub height	$\mathrm{m\,s^{-1}}$
u_{LOS}	line-of-sight wind speed	$\mathrm{m\,s^{-1}}$
u_{m}	wind speed at measurement height (Ch.3, Ch.4)	$\mathrm{m\,s^{-1}}$
u_{meas}	wind speed at measurement height (Ch.2)	$\mathrm{m\,s^{-1}}$
u_{obs}	observed wind speed	$\mathrm{m\,s^{-1}}$
u_{sc}	SCADA-based forecasted wind speed	$\mathrm{m\,s^{-1}}$
$\bar{u}_{\mathrm{sc}}$	ensemble average of SCADA-based forecasted wind speed	$\mathrm{m\,s^{-1}}$
u^*	friction velocity	$\mathrm{m\,s^{-1}}$
v	wind vector index	-
w	weighting factor (Ch.4)	-
w	weight of individual forecast for the hybrid model (Ch.5)	-
$\hat{w}$	normalized weighting factor (Ch.4)	-
x	parameter in stability correction term (Ch.2)	-

x	observation (Ch. 4)	variable dependent
x_0	observed wind power (Ch.2)	W
z	height	m
z_0	roughness length	m
z_{hh}	hub height	m
z_{m}	measurement height (Ch.3, Ch.4)	m
z_{meas}	measurement height (Ch.2)	m
z_{TP}	transition piece height	m
Z	minimum number of valid wind vectors	-
α_{c}	Charnock parameter	-
β	stability correction term constant	-
γ	stability correction term constant	-
δu	difference between wind speed at measurement height and hub height	$\mathrm{m\,s^{-1}}$
δz	difference between measurement height and hub height	m
$\frac{\delta x}{\delta y}$	partial derivative	variable dependent
ΔH	humidity uncertainty	%
ΔL	Obukhov length uncertainty	m
Δp	pressure uncertainty	Pa
Δr	spatial distance between the position of turbines	m
ΔT	temporal resolution of semi-Langrangian advection	s
ΔT_0	water temperature uncertainty	K
ΔT_{TP}	air temperature uncertainty	K
Δu_{hh}	uncertainty of wind speed at hub height	$\mathrm{m\,s^{-1}}$
Δu_{m}	uncertainty of wind speed at measurement height	$\mathrm{m\,s^{-1}}$
Δu_{TP}	uncertainty of wind speed at TP height	$\mathrm{m\,s^{-1}}$
Δx	uncertainty of input variables	variable dependent
Δy	total uncertainty	variable dependent
Δz_0	roughness length uncertainty	m
Δz_{m}	measurement height uncertainty	m

$\Delta\tau$	length of time step for bias correction	s
$\Delta\Theta$	virtual potential temperature difference	K
$\Delta\Psi_{\mathrm{m}}$	uncertainty of stability correction term at measurement height	-
$\Delta\Psi_{\mathrm{hh}}$	uncertainty of stability correction term at hub height	-
ζ	stability parameter	-
ϑ	azimuth angle	$^\circ$
Θ_0	virtual potential temperature at sea level	K
Θ_{TP}	virtual potential temperature at transition piece height	K
κ	Von Kármán-constant	-
μ	mean of distribution	variable dependent
μ_{CNR}	mean of 2D Gaussian	-
μ_{LOS}	mean of 2D Gaussian	-
ν	parameter fitted for empirical covariance matrix	-
σ	standard deviation of distribution	variable dependent
σ_{CNR}	standard deviation of 2D Gaussian	-
σ_{LOS}	standard deviation of 2D Gaussian	-
σ_{mc}	standard deviation of Monte Carlo simulation	$\mathrm{m\,s^{-1}}$
Σ	covariance matrix	-
ϕ	probability density function of standard normal distribution	-
Φ	cumulative distribution function of standard normal distribution	-
φ	elevation angle	$^\circ$
χ	wind direction	$^\circ$
$\chi_{100\,\mathrm{m}}$	WRF wind direction at 100 m height	$^\circ$
Ψ	stability correction term of logarithmic wind speed profile	-
Ψ_{hh}	stability correction term at hub height	-
Ψ_{m}	stability correction term at measurement height	-

Chapter 1

Introduction

1.1 The importance of minute-scale power forecasts

In July 2021 the European Union (EU) sharpened its climate target plan to reduce greenhouse gas emissions by 55 % until 2030 compared to 1990. That requires an increase of the overall share of renewable energies (RE) to 38 %-40 % until 2030 (European Commission, Directorate-General for Climate Action, 2020). In 2020 16.4 % of the EU's electricity demand was covered by wind energy, 3 % of offshore wind (WindEurope, 2021). The installed capacity of wind energy, in 2020 at 220 GW with 25 GW offshore wind, is expected to increase further in the coming years (WindEurope, 2021). The EU Offshore Renewable Strategy aims at a minimum of 60 GW offshore wind capacity by 2030 and 300 GW by 2050 (European Commission and Directorate-General for Energy, 2020). Evidently, wind energy plays an increasingly important role in the EU's energy transition.

The increasing amount of renewable energies in our power system introduces challenges such as the large number of decentralized feed-in, limited transmission grid capacity and the strong volatility of wind and solar power (Rechsteiner, 2021). Offshore wind energy is of particular interest considering the large number of high-capacity wind farms clustered in small areas, e. g. the North Sea. The small geographical dispersion of installed capacity leads to a high correlation between the turbines' power output and thus increased volatility of feed-in (Malvaldi et al., 2017; Potisomporn and Vogel, 2021).

In this context, minute-scale wind power forecasts gain increasing importance to support grid integration of wind energy into our power system, electricity trading and wind turbine or wind farm control. We will address those areas of application in more detail below and summarize them in Table 1.1.

1.1.1 Physical balancing

To assure grid stability, power supply and demand need to be balanced at all times. Thus, in cases where the supply does not match the demand, balancing control actions are performed by the Transmission System Operator (TSO) to maintain the grid frequency and avoid, in the worst case, power outages (Lange and Focken, 2006; Scharff, 2015; Zieher et al., 2015). With the increasing share of renewable energies in the system, i. e. highly volatile feed-in from wind and solar, the physical balancing has become more complex. Common measures to support grid balancing are curtailment, i. e. the sudden reduction of the actual power below the physically available power, of, for instance wind turbines, and redispatch, i. e. shut-down or start-up of fossil power plants on a short notice (Joos and Staffell, 2018). In 2020, 3 % of the German RE feed-in, in total 6146 GWh, most of which was wind energy, were curtailed at a cost of 761.2 Mio €. Redispatch costs amounted to a total of 443 Mio € that same year (Bundesnetzagentur, 2021). Both of these measures reduce the ecological and economical value of RE and should thus be avoided. Commonly, power forecasts are used to support the physical balancing of the transmission grid through the optimization of reserve schedules and thereby the reduction of redispatch costs (Lange and Focken, 2006; Zieher et al., 2015). Considering the increased volatility of supply also on shorter time scales, minute-scale forecasts are gaining importance in this context. While the majority of curtailment is a consequence of grid congestions, accurate forecasts of possible feed-in can support the scheduling of curtailment measures, and thereby to some extent reduce the amount of curtailed wind power (Bird et al., 2016). Further, it can be argued that RE need to contribute more actively to the system security as their share in our energy system increases, for instance by providing ancillary services. This could be done through control strategies that allow the system to respond autonomously to imbalances and support frequency control (Attya et al., 2018). For this purpose reliable minute-scale forecasts of possible feed-in power are required. Such forecasts also enable the wind farm operator to participate in control power markets. For instance, the provision of minute reserve power by wind farms was recently tested in a pilot project in Germany (50Hertz et al., 2016).

1.1.2 Economic balancing

With the liberalization of European electricity markets, electricity trading started to play an increasingly important role in the power system. In European countries the electricity market can be divided into the futures and forwards market, the spot market and the balancing market. While futures and forwards are traded on time horizons from weeks

Table 1.1: A summary of the three areas of application for minute-scale power forecasts and the related advantages for different end-users.

area of application	end-user	advantages of minute-scale forecasts
physical balancing	TSO	optimization of reserve schedules
		reduction of balancing control actions
		improved voltage and frequency control
		reduction of curtailment and redispatch
		reduced uncertainty due to probabilistic forecasts
		improved grid stability during ramp events
	wind farm operator	provision of reserve power
economic balancing	electricity trader	reduction of penalty payments
		reduced uncertainty due to probabilistic forecasts
		improved trading during ramp events
	TSO	reduced need for balancing power
		reduced price volatility
wind farm and wind turbine control	wind farm operator	reduced turbine loads
		increased power output
		increased revenues

to several years ahead of delivery, the spot market aims at shorter time horizons. It consists of the day-ahead market and the intraday market. On the day-ahead market bids can be placed until noon for all hours of the following day (Scharff, 2015). On the intraday market those bids can be adjusted as new information, e. g. provided by forecasts, becomes available. This happens continuously and until the so-called gate closure time of the market. Gate closure times range from 90 minutes (e. g. in Turkey) to 5 minutes (e. g. in Germany) before delivery (Würth et al., 2019) and have been continuously decreasing during the last years with the increasing share of RE. Finally, supply and demand are matched on the balancing market and market participants causing imbalances are penalized (Scharff, 2015). Consequently, inaccurate predictions of power production can cause high costs for electricity traders, and minute-scale forecasts can therefore be of high value.

However, not only electricity traders benefit from more accurate wind power forecasts. Due to the nature of the intraday market, trading decisions impact electricity prices. It was shown that in areas with an overall high wind penetration larger wind power

forecasting errors result in higher volatility of electricity prices on the intraday market (Spodniak et al., 2021; Hu et al., 2021). Intuitively, in situations where wind power was overestimated, thus less wind power than expected is available, prices on the intraday market increase. Vice versa, in situations where wind power was underestimated, the opposite is true and electricity prices decrease (Hu et al., 2021). High price volatility creates uncertainty in the market and is thus not desirable.

In general, the concept of intraday trading is an important measure to support grid stability. Despite a substantial increase in wind and solar power capacity, balancing volume and costs significantly decreased in Germany from 2008 to 2015, referred to as the German Balancing Paradox (Hirth and Ziegenhagen, 2015). While this can, to some extent, be explained by improved wind and solar power forecasting, studies indicate a relation to an increase in intraday trading (Koch and Hirth, 2019).

1.1.3 Wind farm and wind turbine control

Main objectives of wind turbine and wind farm control are active and reactive power control and voltage and frequency control of wind farms (cf. Section 1.1.1), power maximisation and load alleviation (Vali, 2019). Hereby, controllers rely on wind field parameters such as wind speed, wind direction and shear. Conventional controllers are based on feedback and therefore able to react to changes in wind field parameters only after they occur (Hau and von Renouard, 2006). For lidar-assisted approaches, wind field information is collected upstream of the wind turbine, thus with a certain preview time, which allows for a proactive adjustment of wind turbine or wind farm operation (Schlipf, 2016). The possible preview time is directly related to the lidar device used and varies from few seconds to minutes (Würth et al., 2019).

For yaw control, in particular wind direction estimates are used to align the wind turbine with the mean wind direction and thereby increase the turbine's power output (Bossanyi, 2019). Accurate minute-scale predictions of wind direction can help to optimize yaw control and reduce the number of yaw alignments. In the context of wind farms, yaw control is increasingly being explored for the purpose of wake-steering. This involves adjusting the yaw of an upstream turbine so that its wake is deflected away from the downstream turbines in order to increase the overall output of the wind farm (Rott et al., 2018; Simley et al., 2021). The optimization of yaw angles strongly depends on wind direction information. Changes in wind direction not considered by the controller can in the worst case lead to an overall reduction of power. Therefore, accurate predictions of wind direction are considered valuable for wake steering.

1.2 Approaches to wind power forecasting

This section introduces different approaches to wind power forecasting. We will explain the differences between physical and statistical methods with regard to their methodology, spatial and temporal resolution, lead times and areas of application. Furthermore, deterministic and probabilistic forecasts are addressed.

1.2.1 Forecast horizon and forecasting methodology

Forecasting approaches can be divided into physical methods and statistical methods. The choice of method depends on the input data available, the attempted spatial and temporal resolution of the forecast and the forecast horizon (Giebel et al., 2011; Lange and Focken, 2006). Physical methods, i. e. Numerical Weather Prediction (NWP) models, use observational data, e. g. meteorological data, and the governing equations of the atmosphere to draw conclusions regarding future wind speed and power values (Sweeney et al., 2019). They are computationally expensive and have a comparably low temporal and spatial resolution. Often, they are subject to phase errors, spatial errors or a bias, which can be improved by statistical post-processing (Sweeney et al., 2019; Giebel et al., 2011). Physical models are typically applied for time horizons from a few hours to several days ahead, for which they outperform statistical models (Würth et al., 2019; Giebel et al., 2011).

Statistical models utilize historical data, for instance turbine operational data, met mast data or meteorological data, to derive forecasts. They are applied for horizons from a few seconds to several hours ahead (Sweeney et al., 2019). Typical statistical models are time series models such as ARMA (autoregressive moving average), ARIMA (autoregressive integrated moving average) or persistence (Torres et al., 2005; Grigonytė and Butkevičiūtė, 2016; Würth et al., 2019). Persistence is the most simple statistical model, assuming currently observed values will persist until the time of the forecast. In minute-scale forecasting, and in this thesis, persistence is used as a benchmark. Often, statistical methods are black box-models, for instance machine learning approaches such as convolutional or artifical neural networks (CNN, ANN) or support vector machines (SVM) (Giebel et al., 2011; Pichault et al., 2021a; Sweeney et al., 2019).

One approach to increase the information contained in the forecast and to overcome shortcomings of individual approaches is the use of hybrid models (Chang, 2014). It is, for example, common to combine NWP models and statistical models or forecasts with different lead times (Giebel et al., 2011; Sweeney et al., 2019).

While statistical models, in particular persistence, are hard to outperform for fore-

cast horizons on the minute-scale, they are not able to forecast rare or extreme events accurately. That means, sudden and strong in- or decreases of power caused by the passing of fronts, thunderstorms, low-level jets or turbine shut-downs, so-called power ramps, cannot be predicted well by statistical models (Valldecabres et al., 2020; Pichault et al., 2021b; Cutler et al., 2007). However, they are particularly crucial for grid stability and electricity trading (Lacerda et al., 2017). While NWP models are often able to predict the occurrence of power ramps, they are frequently subject to phase, spatial or amplitude errors (Sweeney et al., 2019).

1.2.2 Deterministic and probabilistic forecasts

Forecasts can be either of deterministic or probabilistic nature. Deterministic forecasts are point forecasts that provide a single value for each time step. Probabilistic forecasts on the other hand additionally provide uncertainty information in the form of quantiles, probability density functions or predictive distributions (Gneiting et al., 2007). This uncertainty information is considered useful for end-users as it supports decision making processes (Dowell and Pinson, 2016). In the context of wind power forecasting, uncertainty information can for instance be used to optimize revenues in electricity trading or minimize the number of required balancing actions (Lange and Focken, 2006). When evaluating probabilistic forecasts it is distinguished between their sharpness and calibration. While sharpness evaluates the spread of probabilistic forecasts, calibration assesses the consistency of the forecasts' and observations' statistics. In general, it is desired to enhance the sharpness of a probabilistic forecasts, while subject to calibration (Gneiting et al., 2007).

1.3 Remote sensing-based wind speed and power forecasts

In order to bridge the gap between physical methods with longer forecast horizons and statistical methods, in particular with regard to the forecasting of ramp events, remote sensing-based forecasts have been conceptually researched during the last years. Generally, remote-sensing based methodologies rely on wind speed and wind direction information at some point upstream of the target wind turbine or wind farm that is used to derive information about wind speed and consequently wind power at the target wind turbine in the future. In the following, we will review the requirements for remote sensing for forecasting with regard to scanning speed and range, device positioning and measurement

trajectories, evaluate lidar and radar devices' abilities to fulfill these demands and give an overview on current research on lidar- and radar-based forecasting.

1.3.1 Wind field measurements with remote sensing devices

Remote sensing-based forecasts use temporally and spatially highly resolved wind fields measured upstream of the wind farm to derive information at a location downstream at some time in the future. Lidar (light detection and ranging) and radar (radio detection and ranging) devices are available for that purpose. The wind speed is determined by emitting a laser beam or radio waves, respectively, that are reflected by particles moving with the wind. While the lidar's laser beam is reflected on aerosols in the air, the radio waves are backscattered by meteorological particles with high humidity, such as water droplets or ice crystals (Schroeder et al., 2017). Based on the signal's backscattered frequency and considering the Doppler effect, the line-of-sight wind velocity can be determined (Werner, 2005).

For lidar-based forecasting, typically scanning lidars are utilized. Here, especially due to the length and shape of the used laser pulse, wind speed information is obtained from a long and narrow volume with a nearly Gaussian shaped weighting. The expansion of this probe volume depends on the lidar type and its settings and typically lies in a range of several tens of metres (Frehlich, 2013). Similarly, radar devices measure within a cone-shaped volume defined by the range resolution in the order of 10 m to 20 m and the beam opening angle with common values in the order of 0.5° (Schroeder et al., 2017; Valldecabres et al., 2018a). A scanning Doppler lidar of type Leopshere Windcube 200S placed on an offshore wind turbine and a Doppler radar positioned at the shore are shown in Figure 1.1.

Commercial compact long-range lidars are capable of measuring wind fields with high spatial and temporal resolution up to distances of 14 km. Doppler radars on the other hand reach measuring distances up to 32 km and are in this regard clearly superior to lidar devices (Nygaard and Newcombe, 2018). Considering forecasting applications, larger measuring ranges directly result in higher forecast horizons. Radar devices' shortcomings compared to lidars are their significantly higher cost and larger size, which makes them currently unsuitable for offshore applications (Würth et al., 2019) and limits their utilization for offshore wind power forecasts to locations near the coast. Studies also indicated a lower data availability of radar devices, in particular during clear-air situations (Vignaroli et al., 2017; Hirth et al., 2017). Low data availability, in turn, implies low forecast availability.

For forecasting approaches typically plan position indicator (PPI) scans are performed

Figure 1.1: (left) A scanning lidar of type Leosphere Windcube 200S placed on a wind turbine in the offshore wind farm Riffgat. (right) Doppler radar positioned on the shore close to the wind farm Westermost Rough. Right subfigure adapted from Valldecabres et al. (2018a).

to measure the incoming wind field of a wind farm. Here, the elevation angle is constant while the device scans an azimuth sector upstream. Radar devices are capable to scan a large number of elevation angles in 1 to 2 minutes, allowing to cover a volumetric region in front of the wind farm, including also the rotor area. Opposed to that, lidar devices can measure only one elevation angle when aiming at a similar scanning duration and at maximizing their range. Typically, elevations are set to 0° or a small positive angle. In light of these limitations, the trajectory planning and positioning of lidar devices need to be considered carefully. This could be done by parameter studies using large eddy simulations (LES) in combination with a lidar simulator (Ortensi et al., 2022).

In addition to the high demand for especially offshore wind power forecasts (Section 1.1), offshore locations are particularly suitable for the application of remote sensing-based forecasts due to the unobstructed view of the devices and the less complex terrain and consequently flow. Lidars can be placed either on a turbine platform, on the nacelle of a wind turbine or on any other offshore structure such as substations or light houses. In all of these scenarios a height correction of wind speed is required, namely from platform height to hub height in case of horizontal scans, from varying heights dependent on range gate for elevated scans and even for nacelle-based devices as a consequence of a thrust dependent tilt of the lidar. Dynamic height variations due to turbine thrust also affect lidars placed on turbine transition pieces and have a significant impact on measurement height that increases with range (Rott et al., 2022). Therefore, for lidar-based forecasting, thrust correction and wind speed correction to hub height need to be an essential part of

the methodology. The mentioned lidar set-ups, corresponding trajectories and tilt-related height uncertainties are visualized in Figure 1.2. The figure further indicates uncertainty in measurement height related to the tide.

Another implication of the lidars' slower scanning speeds compared to radar devices is an increased time shift within the measured scans. This becomes a problem when one aims at temporally higher resolved forecasts. Spatio-temporal interpolation techniques can help to synchronize wind fields in time (Beck and Kühn, 2019).

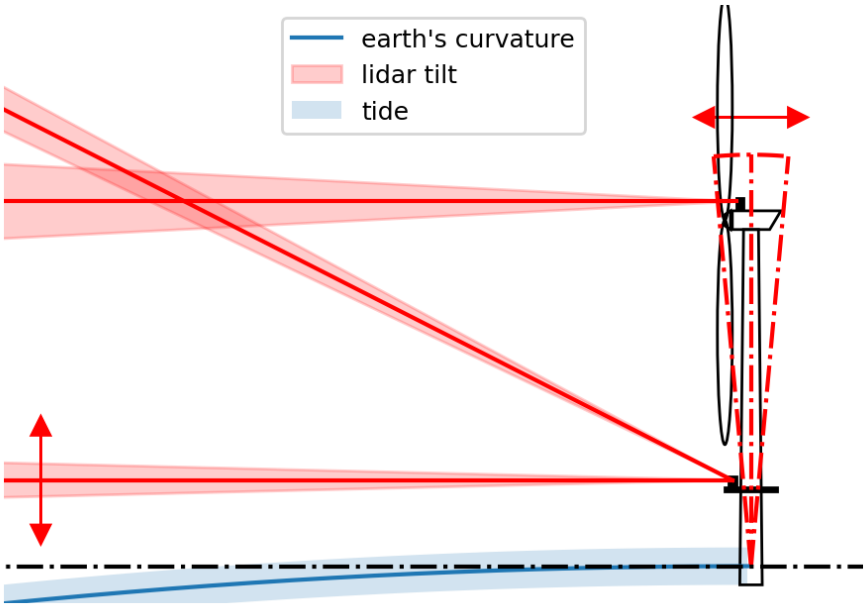

Figure 1.2: Possible lidar set-ups and trajectories at an offshore wind turbine for the purpose of minute-scale forecasting. Measurement height uncertainty related to the thrust-dependent tilt of the device and due to the tide are visualized as red and blue shaded areas respectively. The blue curved line indicates the Earth's curvature. Figure adapted from Schneemann et al. (2021).

A single lidar or radar device is not able to measure the three-dimensional wind speed, but only its one-dimensional projection, namely the line-of-sight (LOS) wind speed. Wind field reconstruction methodologies can determine horizontal wind direction and wind speed information. The commonly applied Velocity-Azimuth-Display (VAD) algorithm, for instance, assumes a homogeneous wind direction and a negligible vertical wind speed component to determine 2D wind field information by fitting a cosine function to LOS wind speeds of a PPI scan (Werner, 2005). A similar method is Volume Velocity Processing (VVP), where wind field components are determined using multivariate regression. Here, basis functions rely on the assumption that wind components change linearly in an analysis volume (Xin and Reuter, 1998). More sophisticated, however, computation-

ally expensive wind field reconstruction methods are 4D-Variational Data Assimilation (Var) (Sun et al., 1991) and 2D-Var (Chan and Shao, 2007). In these approaches a cost function describing the differences between observations and measurements is minimized while subject to certain constraints (Gao et al., 2006).

Using two remote sensing devices with a relative opening angle of at least approximately 30° that scan the same area within the same time frame, two-dimensional wind field information can be retrieved. These set-ups are referred to as dual-Doppler measurements. Compared to single-Doppler measurements dual set-ups have the large advantage to yield accurate local horizontal wind directions. This is in particular valuable for propagation techniques that rely on local wind speed and wind direction information (cf. Section 1.3.2). While the fast radar scans allow to extract local 2D information with high spatio-temporal resolution in a dual set-up (Valldecabres et al., 2018a), 2D information retrieved from dual-Doppler lidar scans is subject to temporal and spatial averaging as a consequence of the devices lower scanning speed (Van Dooren et al., 2016).

1.3.2 State-of-the-art of remote sensing-based forecasts

Lidar- and radar-based forecasting approaches rely on wind vector propagation. That means the wind field measured at an upstream position is used to derive wind speed information at a downstream position in the future. As mentioned previously, the maximum forecast horizon is directly related to the wind speed and the maximum measuring distance. After wind field reconstruction and propagation, wind speed forecasts can be used in combination with a power curve to derive power forecasts.

The simplest advection technique is based on Taylor's frozen turbulence hypothesis, which assumes the wind field propagates with its mean wind speed while preserving turbulent structures (Taylor, 1938). Valldecabres et al. (2018b) used single PPI lidar scans measured with small elevation angles and Taylor's hypothesis to forecast wind speed 5 minutes ahead at a coastal site. They additionally applied a height, roughness and orography correction to account for terrain specific effects. During neutral atmospheric conditions their lidar-based forecast outperformed persistence and ARIMA in terms of deterministic scores. Würth et al. (2018) applied Taylor's frozen turbulence on horizontal PPI lidar scans to predict wind power up to 20 minutes ahead. Opposed to Valldecabres et al. (2018b), the authors generated forecasts at an onshore site. As a consequence of the complex terrain, the lidar-based method was not able to outperform the benchmark persistence in this case. Also Pichault et al. (2021a) determined deterministic wind farm power forecasts using Taylor's hypothesis and slightly elevated single lidar scans at an onshore site. To optimize forecast performance a damping parameter, which was trained

using almost 10 month of data, was incorporated into a smart persistence model. As a second approach the authors present a Deep Convolutional Neural Network (DCNN) based on lidar scans and turbine operational data. Both methodologies were able to outperform the benchmarks persistence and ARIMA throughout a variety of conditions analysed.

Zhou et al. (2018) applied a more flexible version of Taylor's hypothesis to track gust patches and predict their impact on wind turbines. Both impact time and location could be forecasted well. Also in lidar-assisted control, Taylor's frozen turbulence is commonly applied to account for the time lag from lidar measurements to the turbine (Schlipf et al., 2013; Schlipf, 2016).

A different propagation technique was applied to lidar data by Beck and Kühn (2019). The authors used a semi-Langrangian advection technique to synchronize lidar scans in time. Langrangian advection describes the motion of individual air parcels in the flow, thus each particle is propagated with its own wind speed and direction. Doing so causes a non-uniform distribution of particles that can result in large numerical uncertainties when interpolated back to the initially evenly spaced grid. Semi-Langrangian advection works around this problem by propagating in small time steps and interpolating back to the original grid after each step, thus propagating a new set of particles each time step (Durran, 1999). In their work, Beck and Kühn (2019) use semi-Lagrangian advection to generate synchronized lidar wind fields by weighting and combining forward and backward propagated lidar scans.

In all of the above-mentioned studies, wind fields measured by single-Doppler lidar devices were utilized. All forecasting approaches relied on Taylor's frozen turbulence hypothesis to derive deterministic wind speed and power forecasts. While other advection techniques were explored using lidar data, they were not yet used for minute-scale forecasting. In their work, Valldecabres et al. (2018a) have significantly developed remote sensing-based forecasts further. The authors were the first to use dual-Doppler radar data to generate probabilistic power forecasts of free-flow turbines of an offshore wind farm. The 2D wind field information retrieved from the dual set-up was found to be well suited for Lagrangian advection and suggested the development of a probabilistic forecast. The fast scanning speed of the radar devices further allowed to cover a volumetric region in front of the wind farm and consequently the propagation of wind vectors, i. e. horizontal wind speed and wind direction information, at hub height. Mass conservation, vorticity and diffusion were neglected. The radar-based forecast was able to outperform the benchmarks persistence and climatology in terms of probabilistic scores for a 5-minute-ahead forecast. In their analysis the authors showed the impact of the radar coverage on forecast skill. In Valldecabres et al. (2020) the authors extended their probabilistic forecast to all

wind turbines of the wind farm with an emphasis on ramp events. They implemented a correction based on directional turbine efficiency to account for wake effects.

A first step to extend this method also to single-lidar data was made by Würth (2021). They applied a similar methodology to generate probabilistic forecasts of 10-minute averages of wind speed and power of an offshore wind turbine and for lead times up to 30 minutes. The authors utilized horizontal nacelle-based lidar scans and found that the lidar-based approach performs well for a 1 min to 10 min horizon.

Recently, remote sensing-based methods have gained attention for the prediction of ramp events, when statistical method fail. Previously, Hirth and Ziegenhagen (2015) have shown the ability of a Doppler radar to capture ramp events at an onshore wind farm. Also in Valldecabres et al. (2020) the detection accuracy of ramp events by a dual-Doppler radar set-up at a near coastal site was high. The authors further showed that their radar-based forecast's skill compared to persistence is particularly large during ramp events and for free-flow turbines. Also aggregated wind farm power could be forecasted more accurately in a deterministic framework during ramp events using the radar-based approach. Also Würth (2021) concluded that their method is in particular suitable to predict wind ramps. Furthermore, the lidar-based deterministic wind farm power forecast introduced by Pichault et al. (2021a) showed most skilfull results compared to statistical benchmarks during ramp events.

Another interesting approach to minute-scale forecasting was introduced by Rott et al. (2020). The authors used high-frequency operational data of turbines of an offshore wind farm for flow reconstruction and minute-scale wind speed and wind direction forecasting. They applied a Lagrangian advection technique, neglecting diffusion and external forces, in combination with temporal and spatial weighting and a bias correction. Deterministic wind speed forecasts were able to outperform persistence for lead times from 30 s to 120 s. The authors found that the value of their SCADA-based (Supervisory Control and Data Acquisition-based) forecast compared to persistence increases with forecast horizon.

The combination of lidar- or radar-based forecasts with other data sources, such as SCADA data or possibly also data from met masts, would allow to cover a wider range of wind directions, possibly increase forecast horizon and is expected to be more robust against missing or low quality data. Further, including information of the inner-farm region, i. e. wind turbine operational data, in forecasting approaches can support the prediction of wake effects.

1.4 Objectives and research questions of this thesis

Based on the review of the requirements for minute-scale power forecasting, the current state-of-the art of remote sensing-based forecasts and the advantages and disadvantages of radar and lidar devices, the objectives of this thesis were defined. The overall aim of this thesis is the development of a probabilistic minute-scale wind power forecast of offshore wind farms based on lidar measurements and turbine operational data. Lidar-based minute-scale forecasts aim to improve the integration of volatile wind power into the power grid, to increase grid stability and system security, to support electricity trading and to optimize wind farm and wind turbine control. To achieve this, we focus on answering five research questions, namely:

I) How can single long-range lidar measurements with limited measurement range and scanning speed be used to derive probabilistic power forecasts of free-flow offshore wind turbines?

II) How can the impact of atmospheric conditions on forecast skill and forecast uncertainty be mitigated?

III) How can lidar measurements and turbine operational data facilitate high probabilistic forecast availability and skill for turbines distributed in a wind farm?

IV) How can forecasts of individual wind turbines be aggregated to generate skilful probabilistic forecasts of wind farm power?

V) In what way can observer-based power forecasts and persistence be combined to a hybrid model to exploit the benefits of each individual method to the fullest?

1.5 Structure of the thesis

This thesis begins with an introduction, motivating the work and highlighting the research needs (Chapter 1). Further, three peer-reviewed journal articles and one peer-reviewed conference proceeding aim to answer the research questions stated above in Chapters 2-5.

- As established in Chapter 1, remote sensing-based power forecasts have been conceptually researched in the past years. A promising methodology for probabilistic wind power forecasts was developed based on radar measurements (Valldecabres et al., 2018a, 2020). However, to reduce costs and increase feasibility for offshore deployment, an extension of the methodology to lidar data is required. The first journal

article (Theuer et al., 2020b, Chapter 2) introduces a probabilistic lidar-based power forecast that accounts in particular for low data availability in far ranges, time shifts within lidars scans and a difference between measuring height and hub height (research question I). We evaluate this method for free-flow turbines of an offshore wind farm. The first journal article further performs an initial analysis of forecast skill in relation to atmospheric stability and lidar trajectories (research question II). As a consequence of scanning speed and range, wind conditions and wind farm layout, the extension of forecast horizon beyond 5 minutes was not feasible and thus not pursued in the further work.

- Results of the first article indicated the high potential of lidar-based probabilistic forecasting methodologies, however, also revealed uncertainties related to wind speed extrapolation to hub height during certain atmospheric conditions. In a more general context, it highlighted the need for a distinction of forecast skill under different conditions. Therefore, in the second journal article (Theuer et al., 2021, Chapter 3) we introduced two alternative forecasting approaches, performed an extensive uncertainty analysis and evaluated forecast skill under varying atmospheric conditions (research question II). A characterization of forecast skill dependent on different conditions is important to understand the limitations and advantages of the proposed method, also when considering its operational use.

- In the first two journal articles, the lidar-based forecast was solely applied to free-stream wind turbines of an offshore wind farm. To generate accurate forecasts also for wake-influenced wind turbines, one of the newly introduced forecasting approaches implicitly considers wake effects. It is in the third article (Theuer et al., 2022a, Chapter 4) applied to all wind turbines of the wind farm. To further increase forecast availability and skill it is extended to an observer-based forecast using high-frequency operational data of offshore wind turbines (research question III). Probabilistic wind power forecasts of individual wind turbines are further calibrated and finally aggregated utilizing a copula approach (research question IV).

- All three journal articles have shown the advantages of persistence over the lidar-, respectively observer-based forecasts during stable atmospheric conditions and vice versa in unstable cases. This suggests the complementary use of both methods, instead of relying on one individual approach. In the fourth article (Theuer et al., 2022b, Chapter 5), we therefore develop two hybrid methods that combine persistence and the observer-based forecast (research question V). All methods are further extended to a one-year long period, mimicking the atmospheric conditions at the

wind farm site, in order to evaluate their potential benefit over a longer time period.

Finally, a conclusion and outlook, summarizing the main findings with regard to the research questions and elaborating on necessary future research steps, concludes the thesis in Chapter 6.

Chapter 2

Minute-scale power forecast of offshore wind turbines using long-range single-Doppler lidar measurements[a]

Decreasing gate closure times on the electricity stock exchange market and the rising share of renewables in today's energy system causes an increasing demand for very short-term power forecasts. While the potential of dual-Doppler radar data for that purpose was recently shown, the utilization of single-Doppler lidar measurements needs to be explored further to make remote-sensing-based very short-term forecasts more feasible for offshore sites. The aim of this work was to develop a lidar-based forecasting methodology, which addresses a lidar's comparatively low scanning speed. We developed a lidar-based forecast methodology using horizontal plan position indicator (PPI) lidar scans. It comprises a filtering methodology to recover data at far ranges, a wind field reconstruction, a time synchronization to account for time shifts within the lidar scans and a wind speed extrapolation to hub height. Applying the methodology to seven free-flow turbines in the offshore wind farm Global Tech I revealed the model's ability to outperform the benchmark persistence during unstable stratification, in terms of deterministic as well as probabilistic scores. The performance during stable and neutral situations was significantly lower,

[a]The content of this chapter is identical to the peer-reviewed version of the following journal article published in Wind Energy Science: Theuer, F., van Dooren, M. F., von Bremen, L., and Kühn, M.: Minute-scale power forecast of offshore wind turbines using long-range single-Doppler lidar measurements, *Wind Energy Science*, 5, 1449–1468, https://doi.org/10.5194/wes-5-1449-2020, 2020.

which we attribute mainly to errors in the extrapolation of wind speed to hub height.

2.1 Introduction

With the increasing penetration of renewable energies in the power system, the demand for very short-term power forecasts is continuously rising. Transmission system operators (TSOs) need to ensure grid stability by balancing supply and demand of power at all times. In this regard, very short-term forecasts are an important tool to support power system management and reduce curtailment costs (Liang et al., 2016). Further, minute-scale forecasts hold significant value for energy market applications (Cali, 2011), especially with gate closure times nowadays being as short as only 5 min, for example in Germany, Belgium and France (EPEXSPOT, 2020). Also, the provision of ancillary services, e. g. the supply of reserve power by wind farms (50Hertz et al., 2016), would benefit from improved very short-term forecasts. Probabilistic forecasts additionally provide uncertainty information and are thus especially useful to support decision-making processes (Dowell and Pinson, 2016). While for forecast horizons of several hours or days physical models such as numerical weather prediction (NWP) models are typically used, on shorter timescales, i. e. lead times ranging from minutes to several hours, statistical models are applied (Giebel et al., 2011). For lead times of a few to several hours, this includes mainly time series models, Kalman filters and model output statistics (MOS) (Sweeney et al., 2019). The simplest statistical model for even shorter lead times is persistence, which assumes the future value will be equal to the current one. Persistence is often referred to as a benchmark in very short-term forecasting (Würth et al., 2019). Other statistical models such as ARMA (autoregressive moving average) take a higher number of past values and past forecasting errors into account (Torres et al., 2005). ARIMA (autoregressive integrated moving average) models additionally difference the time series to achieve stationarity (Grigonytė and Butkevičiūtė, 2016). Further, spatial correlation approaches, machine learning algorithms and neural networks are gaining importance for very short-term forecasts (Lenzi et al., 2018; Huang and Kuo, 2018). To overcome the limitations of individual models, combinations of different methodologies, so-called hybrid models, are being increasingly researched (Zhou et al., 2018).

As a promising alternative to statistical methods, recently very short-term forecasts based on remote sensing measurements have gained attention (Sweeney et al., 2019). The basic concept is to measure incoming wind fields in far distances upstream and thus several minutes before reaching the turbine or wind farm, allowing the derivation of wind speed and power forecasts in the very short term. Lidar-based forecasts (LFs)

have for example been used by Valldecabres et al. (2018b) to predict nearshore wind speeds and they outperformed the benchmark persistence. Würth et al. (2018) used lidar measurements at an inland location to predict wind power, however, they were not able to outperform persistence, which the authors attributed to the complex terrain. A skilful probabilistic power forecast was recently developed by Valldecabres et al. (2018a), utilising dual-Doppler radar measurements performed by a radar system located at the shoreline, scanning the flow around an offshore wind farm. Using the same radar set-up Valldecabres et al. (2020) moreover detected and probabilistically forecasted ramp events at free-stream as well as waked wind turbines.

While Doppler radars are capable of measuring in distances of up to 32 km (Nygaard and Newcombe, 2018) with high temporal and spatial resolution and provide volumetric 2D wind field information in the case of a dual set-up (Hirth et al., 2017), such devices are also rather expensive, comparatively large and thus not easily deployable at far-offshore sites (Würth et al., 2019). Studies also indicated their reduced data availability in comparison to lidars, especially during clear-air situations (Vignaroli et al., 2017; Hirth et al., 2017). Therefore, the use of Doppler lidar measurements instead of Doppler radar measurements is considered an interesting and probably more feasible alternative, especially with regard to offshore applications. Today, compact industrial scanning lidar systems are able to measure at distances of up to 10 km (Leosphere, 2018). Hereby, the maximal measuring distance is closely related to the measurement accumulation time. To enlarge the maximal range of the measurements, the accumulation time needs to be increased and thus the overall scanning speed is reduced. While radars can perform volumetric measurements, i. e. measurements with several different elevation angles, with a repetition time of the order of a few minutes, the slow scanning speed of current lidars restricts measurements to a single elevation angle when aiming to perform scans within a time frame of approximately 1 to 2 min. Consequently, depending on the positioning of the lidar system and the choice of elevation angle, the device's measuring height does not match the hub height of the turbine. Also, platform or turbine movements can contribute to a static as well as dynamic misalignment (Bromm et al., 2018). Using such lidar measurements for wind speed and power prediction thus necessitates the use of a wind speed correction to hub height. As opposed to dual-Doppler radar measurements, the use of a single lidar device only allows the retrieval of one-dimensional wind speed information. Reasons for single-Doppler lidar measurements are for example cost reduction or a wind farm layout that does not favour a dual set-up. Consequently, a reliable wind speed reconstruction methodology is essential to retrieve horizontal wind speed information from single lidar measurements.

Our objective in this paper is to investigate whether and how one can use long-range single-Doppler lidar measurements to forecast the power of offshore wind turbines on short time horizons in a probabilistic manner. We adapt a remote sensing-based forecast methodology to meet the requirements of single-Doppler lidar measurements. We especially implement adjustments to account for (i) low data availability in far ranges, (ii) time shifts within the lidar scans and (iii) deviations between measuring height and hub height. We validate the method by means of a case study based on measurements at an offshore wind farm and by distinguishing between different atmospheric conditions. To address their performance, we compare lidar-based forecasts against the benchmark persistence.

The paper is structured as follows: Sect. 2.2 describes lidar scans used for minute-scale forecasting. In Sect. 2.3 the forecasting methodology is developed. Section 2.4 provides an overview of the case study analysed here, evaluates the proposed methodology and presents the results of probabilistic and deterministic power forecasts. In Sect. 2.5 we discuss possible sources of uncertainty and the impact of atmospheric stability and the measurement set-up on the results before the conclusions (Sect. 2.6) are drawn.

2.2 Planar long-range lidar measurements

For the purpose of forecasting, typically horizontal plan position indicator (PPI) lidar scans, i. e. with an elevation angle of $\varphi = 0°$, are used. Hereby, the lidar device can be placed either on the nacelle or transition piece (TP) of a wind turbine or a nearby platform. The aim is to cover an area upstream of the wind farm, preferably in the main wind direction. Scan parameters, i. e. averaging time and azimuthal resolution are chosen to maximize the measurement distance while keeping the scanning time as short as possible. Scan orientations need to be adjusted according to the wind direction. For each measurement, typically the line-of-sight (LOS) velocity, carrier-to-noise ratio (CNR) as well as azimuth angle, range gate, and time information are available.

For the case study presented in Sect. 2.4 of this paper, such a typical set-up was used. Without loss of generality of the methodology introduced in Sect. 2.3, we are describing the main parameters of this lidar campaign to provide a realistic example. Lidar scans were performed at the offshore wind farm Global Tech I (GT I) located in the German North Sea from August 2018 until February 2020 with a Leosphere Windcube 200S (Serial no. WLS200S-024) lidar system positioned on the transition piece of the westerly located turbine T2 as depicted in Fig. 2.1. The lidar was placed at a height of about 24.6 m a.m.s.l. (above mean sea level). Scans were performed with an azimuthal resolution of 2°,

averaging time of 2 s per measurement, a pulse length of 400 ns and range gates ranging from 500 m to 8000 m with 35 m spacing. The lidar scan spanned a sector of 150°, thus the duration of one scan was $T_{\mathrm{tot}} = 156\,\mathrm{s}$, i. e. measuring time $T_{\vartheta} = 150\,\mathrm{s}$ plus a measurement reset time of approximately $T_{\mathrm{r}} = 6\,\mathrm{s}$. One of four different scan orientations (Fig. 2.1b) was chosen manually according to the wind direction. A more detailed analysis of the lidar data will follow in Sect. 2.4.1.

Besides horizontal PPI lidar scans ($\varphi = 0°$), high-elevation scans with $\varphi = 13.57°$, measuring the inflow of turbine T2, were performed. Here, it was measured with an azimuthal resolution of 1° and an averaging time of 0.2 s per measurement. At hub height, measurements were performed with a distance to the rotor larger than $2.4D$ and therefore outside of the induction zone, as recommended by the International Electrotechnical Commission's (IEC) standard for power curve measurements (IEC, 2017). A total azimuth range of 180°, varying from 134° to 313° was spanned, which means it took about 36 s to perform one scan and approximately 8 s to reset the measurement. Mean wind speeds and wind directions with an averaging period of 44 s at hub height were determined by applying a velocity azimuth display (VAD, see Sect. 2.3.1) algorithm to each scan. Only situations with wind directions ranging from 180° to 270° were considered for further analysis. The 44 s mean wind speeds were used to construct a probabilistic power curve in Sect. 2.3.5.

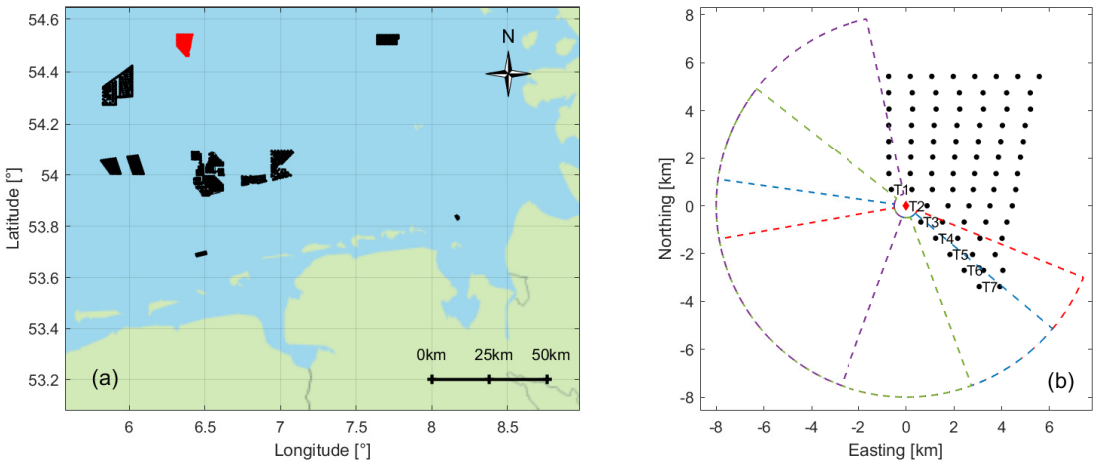

Figure 2.1: (a) Position of the offshore wind farm Global Tech I (GT I) in red. Other wind farms in the North Sea, which were operational during the measurement campaign, are shown in black. In (b) the layout of GT I is depicted with turbines marked as black dots. The lidar is positioned on the transition piece (TP) of turbine T2 marked in red and defined as the origin of the coordinate system. The four measuring trajectories are depicted in colour. Forecasts were generated for turbines T1-T7.

2.3 Methodology

Figure 2.2 gives an overview of the proposed lidar-based forecast methodology. First, a wind field reconstruction algorithm was applied to retrieve horizontal wind field information from line-of-sight measurements of the angular scans (Sect. 2.3.1). To keep as many data from far ranges as possible, a dynamic data filtering approach was used. The low scanning speed required time synchronization within each lidar scan, which was realized by means of a propagation algorithm (Sect. 2.3.2). Subsequently, an advection technique was applied to determine a wind speed forecast with lead time k (Sect. 2.3.3). The wind speed forecast was defined by selecting wind vectors arriving within a predefined area of influence (AoI). This set of wind vectors formed the basis of the probabilistic wind speed and power forecast. In the next step, wind vectors were extrapolated from measuring height to hub height (Sect. 2.3.4). Finally, hub height wind speeds were translated into a probabilistic power forecast utilizing a probabilistic power curve (Sect. 2.3.5).

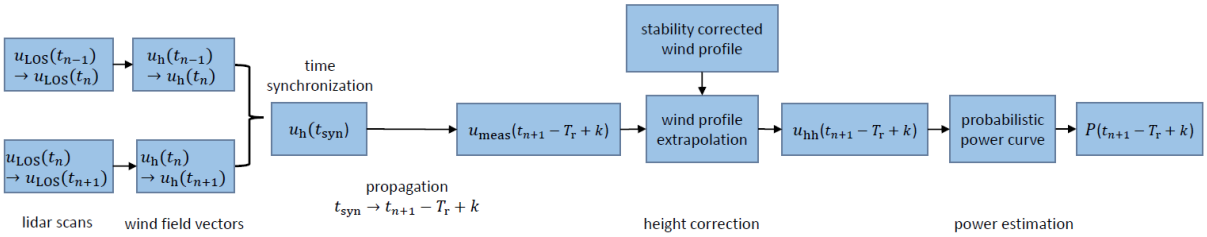

Figure 2.2: Schematics of the lidar-based forecast methodology. Line-of-sight wind speed measurements $u_{\mathrm{LOS},n}$ measured within a time interval $[t_n, t_{n+1} - T_\mathrm{r}]$ were filtered and a wind field reconstruction was performed. Using two consecutive lidar scans, the horizontal wind speeds $u_{h,n}$ were then synchronized at time t_syn. A propagation technique was applied to propagate wind vectors to $t_{n+1} - T_\mathrm{r} + k$ with end time of the scan t_{n+1}, measurement reset time T_r and lead time k. Wind speed forecasts u_meas were further extrapolated to hub height and transferred to power forecasts by means of a probabilistic power curve.

2.3.1 Lidar data filtering and wind field reconstruction

When performing lidar measurements several factors such as meteorological conditions, hard targets and device limitations can lead to invalid measurements. Typically, the carrier-to-noise-ratio (CNR) is used as an indicator for the backscattered signal's quality. Low CNR values hereby indicate low data quality and are commonly neglected by means of threshold filters (Aitken et al., 2012). However, when applying a CNR-threshold filtering approach, a significant number of valid data, especially from far distances, are excluded (Valldecabres et al., 2018b). As long measurement distances are most important for this

work, we combined a CNR threshold filter and a dynamic filtering approach. Our choice of CNR-thresholds is hereby based on similar ones suggested in literature (Valldecabres et al., 2018b; Würth et al., 2018). All measurements with CNR $> 0\,\mathrm{dB}$ and CNR $< -30\,\mathrm{dB}$ were neglected, measurements with $-26.5\,\mathrm{dB} <$ CNR $< -5\,\mathrm{dB}$ were always considered valid, and remaining values were filtered using the dynamic density filter developed by (Beck and Kühn, 2017). Here, CNR and line-of-sight (LOS) wind speed measurements were first normalized and sorted in a 2D plane before a 2D Gaussian function with standard deviations σ_{CNR} and σ_{LOS} and mean values μ_{CNR} and μ_{LOS} was fitted to the normalized values. Finally, those values positioned outside of an ellipse defined by the semi-axes $2.75\,\sigma_{\mathrm{CNR}}$, $2.75\,\sigma_{\mathrm{LOS}}$ and the centre position μ_{CNR} and μ_{LOS} were discarded.

After filtering, the global wind direction was determined by performing a VAD-like fit individually for each range gate in a certain scan. To do so, homogeneity across range gates was assumed and the vertical wind speed component neglected (Werner, 2005). Range gates with fewer than 15 valid lidar measurements were discarded. A one-dimensional wind speed projection on the prevailing wind direction of the range gate r was performed using

$$u_{\mathrm{h}}(r,\vartheta) = \frac{u_{\mathrm{LOS}}(r,\vartheta)}{\cos(\vartheta - \chi(r))}. \tag{2.1}$$

Values with

$$75^\circ < |\vartheta - \chi| < 105^\circ, \tag{2.2}$$

where ϑ denotes the azimuth angle of the lidar's scanner and χ the wind direction, were neglected as they show large error values due to the almost perpendicular orientation of wind direction and azimuth angle. We will refer to those as critical angles or the critical region in the following. Apart from that, remaining outliers with values deviating more than 2.75 standard deviations σ from the mean wind speed of the scan were neglected (Felder et al., 2018). Only scans with an overall data availability of at least 80 % were considered for the forecast. For further analysis, the results were interpolated onto a Cartesian grid with 25 m spacing. Figure 2.3 shows an example of a reconstructed wind field.

2.3.2 Time synchronization of lidar scans

When the time shift within a lidar scan is larger than the averaging time (1 min) of the forecasted values, one cannot assume the scan to be quasi-instantaneous, which is commonly done when considering wind speed averages from lidar scans. Several approaches to account for the time shift within the scan have been tested, all aiming to synchronize

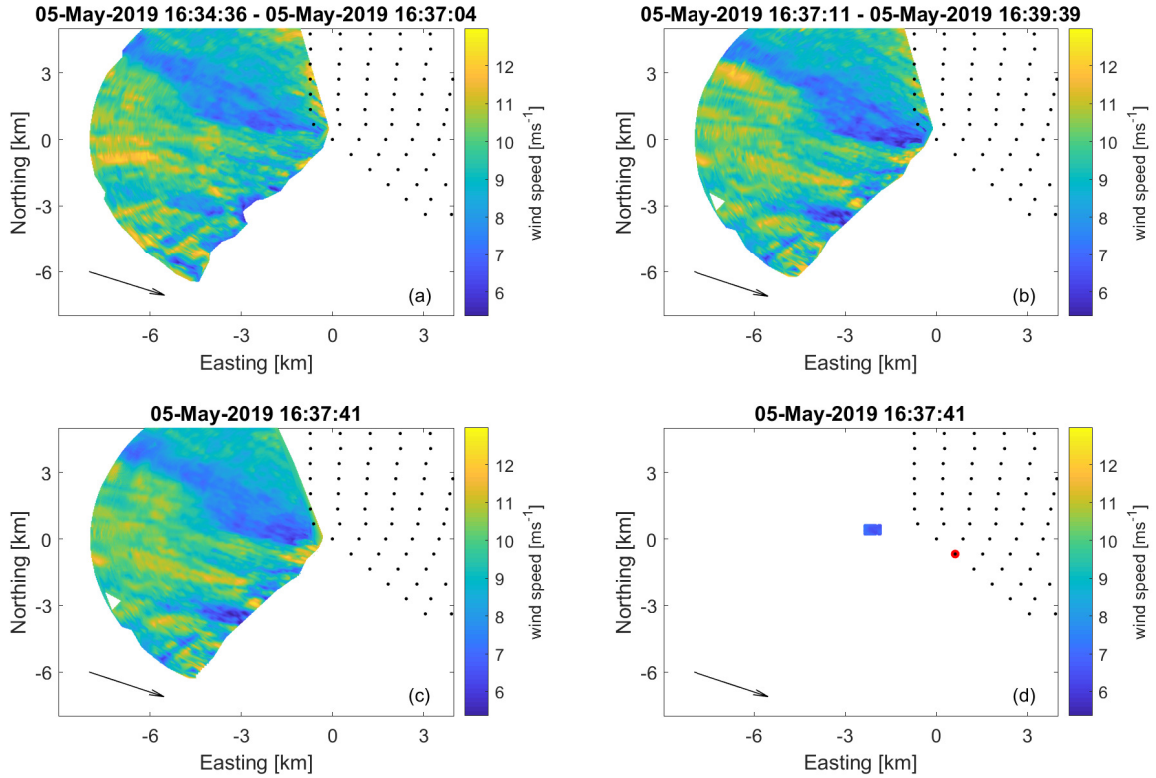

Figure 2.3: Time synchronization and wind speed forecast of an exemplary scan. Panels (a) and (b) depict two consecutive lidar scans at GT I with black dots indicating the positions of the turbines. In (c) the time-synchronized scan determined as a combination of the forward-propagated scan (a) and the backwards-propagated scan (b), is shown. In (d) a point cloud of wind vectors that will reach T3 marked in red after a forecasting horizon of 5 min±30 s is visualized. The mean wind direction of the scan is shown in black.

the scan in time before applying the propagation methodology (Sect. 2.3.3). We found the most accurate results applying a time synchronization developed by Beck and Kühn (2019), which is visualized in Fig. 2.4. Here, lidar scans were propagated by means of a semi-Lagrangian advection technique. Propagated scans were generated with a temporal resolution of ΔT. Each propagation was a combination of a forward- and a backwards-propagated scan, weighted according to a trigonometric function following the suggestion of Beck and Kühn (2019). The weighting was dependent on the time passed since the initialization of the original scan. Hereby, backward propagations were only taken into account after one-fifth of the total scanning time T_{tot}. The total scanning time consists of the measuring time T_{ϑ} and the measurement reset time T_{r}. A 3D natural-neighbour interpolation (Sibson, 1981) was applied to the sequence of propagated scans, determining the horizontal wind speed u_{h} across the scanned domain and at time t_{syn}. Figure 2.4 shows the current lidar scan initialized at time t_n and the previous one initialized at

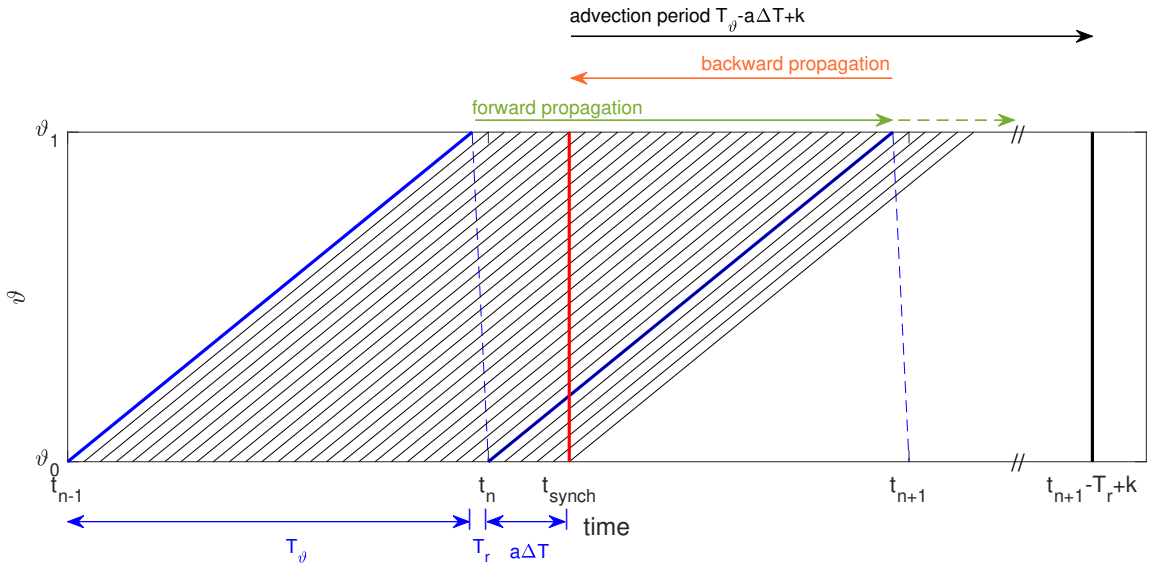

Figure 2.4: Time synchronization of the lidar scan initialized at t_n shown in blue to time $t_{\text{syn}} = t_n + a\,\Delta T$ shown in red. The scanning domain is here visualized as azimuth angle ϑ over time. The synchronized scan is interpolated using propagated lidar scans with a temporal resolution of ΔT. The measurement reset time T_{r} is indicated as the dashed blue line. Propagated scans, which are shown in grey, are a combination of a forward and backward propagation weighted according to a trigonometric function. Green and orange arrows above the figure indicate to which of the propagated scans both forward and backward propagation and to which only a forward propagation contributes. The synchronized scan at t_{syn} can thus be reconstructed using only the two consecutive lidar scans initialized at t_n and t_{n-1}. t_{syn} should be chosen to minimize the wind vector advection period to the forecast time $t_{n+1} - T_{\text{r}} + k$ with lead time k, indicated as a black arrow. Figure adapted from Beck and Kühn (2019).

$t_{n-1} = t_n - T_{\text{tot}}$ in blue. The scanning domain is visualized as azimuth angle ϑ over time. The propagation steps in between the two scans, performed with the temporal resolution ΔT, are shown in grey. Backward and forward propagations are indicated as orange and green arrows. The red line indicates the synchronization time step t_{syn} at which the natural-neighbour interpolation was performed. For the purpose of forecasting, t_{syn} should be chosen to stay within the region of the weighting function that puts no weight to backwards-propagated scans that were measured after the forecast's initialization time, thus $t_{\text{syn}} \in [t_n, t_n + a\,\Delta T]$. Here a denotes the maximal number of propagation steps possible, while avoiding backwards propagation. That means the time synchronization can be performed by two consecutive lidar scans only, avoiding the need for a future scan. We chose the maximal $t_{\text{syn}} = t_n + a\,\Delta T$ to minimize the wind vector advection period as indicated by the black arrow in Fig. 2.4.

2.3.3 Wind speed forecast

To generate a wind speed forecast the methodology developed by Valldecabres et al. (2018a) was utilized. A Lagrangian advection technique, based on the assumption that wind vectors propagate with their local horizontal wind speed and wind direction (Germann and Zawadzki, 2002), was applied. It was thus assumed that the wind field vectors do not change their trajectory with time. As a consequence of the wind field reconstruction explained in Sect. 2.3.1, the direction of wind vectors was the same for all azimuth angles and varied only with range gate. Apart from that, we neglected vorticity, mass conservation and diffusion (Germann and Zawadzki, 2002; Valldecabres et al., 2018a). To develop a wind speed forecast with lead time k, wind field vectors were propagated in time and space from their original position at the synchronized time step t_{syn} to the last time step of the scan $t_{n+1} - T_{\mathrm{r}}$ and further to $t_{n+1} - T_{\mathrm{r}} + k$.

Vectors arriving within a previously defined area of influence around the turbine of interest and within a time interval of $t_{n+1} - T_{\mathrm{r}} + k \pm 30\,\mathrm{s}$ were selected and used for the wind speed forecast. Hereby, wind vectors originating inside of the wind farm area were neglected. Further, we considered vectors to be able to only contribute to one turbine, i. e. the first turbine they reached. An example of such a point cloud is shown in Fig. 2.3d. The AoI was defined as a circle centred around the turbine's position and its radius was optimized by minimizing the average continuous ranked probability score (crps; see Sect. 2.4.4) (Gneiting et al., 2007) of a 1-minute-ahead wind speed forecast at a reference free-flow turbine as suggested by Valldecabres et al. (2018a). That means the forecast was optimized with respect to its probabilistic rather than its deterministic scores. Further, the minimum required number of wind vectors reaching the turbine was determined by applying the same methodology. Forecasts based on fewer vectors were considered invalid.

At this point, two orders of the methodological steps are possible, i. e. propagating wind vectors at varying heights that are different from the height of interest to the target turbines before extrapolating to hub height or performing the extrapolation prior to the wind vector propagation. Each of the two possibilities is associated with specific errors. In this case study, we chose to propagate wind vectors before the wind speed extrapolation as this yielded more accurate results. The consequences of this approach will be discussed in Sect. 2.5.1.

2.3.4 Wind speed extrapolation to hub height

As the lidar was positioned at TP height, an extrapolation to the hub height was needed. A logarithmic wind profile including a stability correction $\Psi(\frac{z}{L})$ (Peña et al., 2008) was

used to do so.

$$u_{\mathrm{h}} = \frac{u^*}{\kappa}\left(\ln\left(\frac{z}{z_0}\right) - \Psi\left(\frac{z}{L}\right)\right) \tag{2.3}$$

$$u^* = \sqrt{\frac{z_0\, g}{\alpha_{\mathrm{c}}}} \tag{2.4}$$

The wind profile includes the horizontal wind speed u_{h}, roughness length z_0, height z, the gravitational acceleration g and the Obukhov length L. The friction velocity u^* is expressed in terms of the Charnock parameter α_c, which describes the relation between wind speed and roughness of the sea surface and was set to $\alpha_{\mathrm{c}} = 0.011$ as suggested by Smith (1980) for far-offshore conditions. The von Kármán constant is defined as $\kappa = 0.4$.

The atmospheric stability for each lidar scan was determined using the methodology described by Sanz Rodrigo et al. (2015). Air and sea surface temperature, pressure and relative humidity values were used to determine the virtual potential temperature difference $\Delta\Theta = \Theta_{\mathrm{TP}} - \Theta_0$ between TP height Θ_{TP} and the sea surface Θ_0 as well as the virtual temperature at sea level T_{v}. The wind speed u_{TP} was defined as lidar measurements at the closest range gate of 500 m. The stability estimation was performed using 30 min moving averages of all variables. Here, first the bulk Richardson number Ri_{b} was calculated, which was then transferred into the stability parameter ζ as defined by Grachev and Fairall (1997) and finally the Obukhov length L according to Eqs. (2.5)-(2.7).

$$Ri_{\mathrm{b}} = \frac{g}{T_{\mathrm{v}}}\frac{0.5\, z_{\mathrm{TP}}\Delta\Theta}{u_{\mathrm{TP}}^2} \tag{2.5}$$

$$\zeta = \begin{cases} \frac{10Ri_{\mathrm{b}}}{1-5Ri_{\mathrm{b}}} & Ri_{\mathrm{b}} > 0 \\ 10Ri_{\mathrm{b}} & Ri_{\mathrm{b}} \leq 0 \end{cases} \tag{2.6}$$

$$L = \frac{0.5\, z_{\mathrm{TP}}}{\zeta} \tag{2.7}$$

For the calculation of the stability correction term Ψ the definition (Paulson, 1970; Holtslag and De Bruin, 1988) shown below was used.

$$\Psi = \begin{cases} 2\ln\left(\frac{1+x}{2}\right) + \ln\left(\frac{1+x^2}{2}\right) - 2\arctan(x) + \frac{\pi}{2} & L < 0, \text{ where } x = (1-\gamma\frac{z}{L})^{1/4} \\ -\beta\frac{z}{L} & L \geq 0 \end{cases} \tag{2.8}$$

with $\beta = 6$ and $\gamma = 19.3$ as suggested by Högström (1988). The roughness length z_0 was determined by fitting the wind speed profile to the wind speed measurements u_{TP}, using

the calculated Obukhov length L.
With the height of the measurement z_{meas} the wind speed at hub height u_{hh} can then be expressed as

$$u_{\mathrm{hh}} = u_{\mathrm{meas}} \frac{\ln(\frac{z_{\mathrm{hh}}}{z_0}) - \Psi(\frac{z_{\mathrm{hh}}}{L})}{\ln(\frac{z_{\mathrm{meas}}}{z_0}) - \Psi(\frac{z_{\mathrm{meas}}}{L})} = u_{\mathrm{meas}}\, c_{\mathrm{h}}. \tag{2.9}$$

In the following, we will refer to c_{h} as the height extrapolation factor.

2.3.5 Probabilistic wind power forecast

The forecasted wind speed distribution was finally transformed into a wind power distribution. To do so, a probabilistic power curve constructed using high-elevation lidar scans (Sect. 2.2) and high-frequency SCADA power data of turbine T2 (Sect. 2.4.1) was applied. Usually, 10 min wind speed and power averages are used to construct power curves; however, we used 44 s mean values, in accordance with the measurement time per scan, to capture the power curve's associated uncertainties more accurately (Gonzalez et al., 2017). Wind speed values were air density corrected as described by Ulazia et al. (2019) and according to IEC 61400-12-1 (IEC, 2017). Air pressure and temperature values were hereby corrected to hub height applying temperature gradients of the ISO standard atmosphere as suggested by ISO2533 (ISO, 1987). The mean value and standard deviation of power within wind speed intervals of $0.5\,\mathrm{m\,s^{-1}}$ width were determined (Gonzalez et al., 2017). These values were further used to define a normal cumulative distribution function (cdf) of power for each wind speed interval. Figure 2.5 shows the normalized probabilistic power curve with standard deviations of power indicated by error bars. For each value of the forecasted wind speed distribution, i. e. for each wind vector reaching the area of influence, one power value was randomly selected using the normal cdf of its corresponding wind speed interval. A resampling technique with replacement (Efron, 1979) was applied to the resulting power distribution, randomly selecting 10 000 power values, as suggested by Valldecabres et al. (2018a).

2.4 Results

In the following, we will first introduce the case study at the offshore wind farm Global Tech I, then analyse the method's advantages and limitations, and afterwards assess the quality of a 5 min ahead lidar-based deterministic as well as probabilistic wind power forecast of the free-flow turbines T1-T7, based on the mentioned case study.

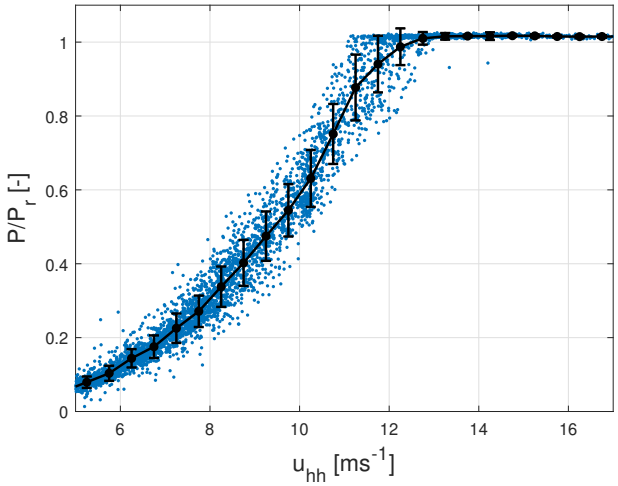

Figure 2.5: Normalized probabilistic power curve of wind turbine T2 with average power and its standard deviation in black for each wind speed interval.

2.4.1 Case study at the offshore wind farm Global Tech I

Power forecasts at Global Tech I were analysed as a case study. The wind farm consists of 80 wind turbines of the type Adwen 5-116 with a rotor diameter of $D = 116\,\mathrm{m}$, a hub height of $z_{\mathrm{hh}} = 92\,\mathrm{m}$ and a rated power of $P_{\mathrm{r}} = 5\,\mathrm{MW}$. The total capacity of the wind farm is $P_{\mathrm{total}} = 400\,\mathrm{MW}$. 1 Hz SCADA data, including power and wind direction values of all wind turbines, as well as information regarding the turbines' operational status, were available for the period of the measurement campaign. Wind speed values were not measured but estimated by the SCADA system based on power, pitch angle and the turbine power curve. Further, information regarding the SCADA data quality was available and used to remove low-quality data. In the following analysis, we used 1 min mean values of wind speed and power within the interval $t \pm 30\,\mathrm{s}$ to validate wind speed as well as power forecasts for seven wind turbines in the first south-westerly row marked in Fig. 2.1. We refer to those turbines as T1-T7 in the following.

A forecast was generated for each lidar scan, thus with a temporal resolution of approximately 2.5 minutes. Forecasts within the interval from 8 March to 31 May 2019 were evaluated. Here, we only considered situations in power production mode below rated wind speed. For further analysis, only scans with a total spatial availability of at least 80 % after applying the filtering algorithms (Sect. 2.3.1) were considered. The total availability was considered to be 100 % if data at all measured range gates and azimuth angles between 140° and 300° were valid. Missing data beyond these azimuth limits was considered not to impact the quality of the forecast gravely and thus neglected when determining the total spatial availability. In total, 17 024 lidar scans with a mean availability of 89.7 % were used for the analysis. The wind speed and direction distribution of those

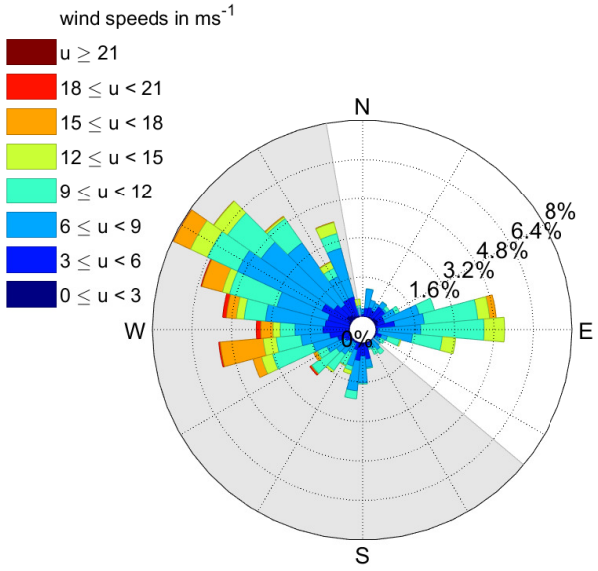

Figure 2.6: Wind speed and direction distribution of the used data set at the wind farm Global Tech I. Shown are mean wind speed and direction values for all lidar scans with a data availability of at least 80 % within the period from 8 March to 31 May 2019. The grey shaded area indicates wind directions that were considered for further analysis.

situations considered are visualized in Fig. 2.6. North-westerly winds from 250° to 320° were identified as the prevailing wind direction. Wind speeds mainly lay between $6\,\mathrm{m\,s^{-1}}$ and $12\,\mathrm{m\,s^{-1}}$. As a consequence of the wind farm's layout, we only used scans with wind directions $130° < \chi \leq 350°$, indicated as grey shaded area in Fig. 2.6.

To perform the time synchronization an interpolation time step $\Delta T = 6\,\mathrm{s}$ was chosen. With a scanning time of $T_{\mathrm{tot}} = 156\,\mathrm{s}$, we chose the synchronization time as $t_{\mathrm{syn}} = t_n + 5\Delta T = t_n + 30\,\mathrm{s}$ in order to avoid the need for a backwards propagation as explained in Sect. 2.3.2. Time-synchronized wind vectors were propagated with a lead time of $k = 300\,\mathrm{s}$ to generate a wind speed forecast. For a forecast to be valid, at least a number of $Z = 20$ wind vectors needed to be available. The radius of the area of influence was set to $R_{\mathrm{AoI}} = 0.2D = 23.2\,\mathrm{m}$, following the methodology described in Sect. 2.3.3, with T2 as the reference turbine.

L was determined using meteorological measurements: air pressure, humidity and air temperature measurements were performed using two sensors (Vaisala PTB330 and Vaisala HMP155) from July 2018 until February 2020, both positioned at the height of the lidar at about 24.6 m. Additionally, sea surface temperature (SST) data, which showed a good agreement with on-site buoy measurements performed at an earlier time

(Schneemann et al., 2020), was available from the OSTIA data set (Good et al., 2020). SST data are available at noon every day and were linearly interpolated to match the timestamps of the lidar scans. Interpolations were performed utilizing both past and future values with respect to the initialization time. The interpolated SST data are in this context understood as an artificial buoy measurement. L was then used to extrapolate wind vectors from measuring height to hub height following Sect. 2.3.4.

During the measurement campaign, a slight elevation misalignment of the lidar was detected. Using a so-called sea surface levelling method the magnitude of pitch and roll of the lidar, i. e. the tilt of the geographical coordinate system, was determined as proposed by Rott et al. (2017). The inclinations were hereby found to be related to the mean wind speed and wind direction, i. e. the thrust and the yaw orientation of the turbine. Pitch and roll, defined as clockwise rotations around the x and y axes, were $0.02°$ and $-0.11°$ for the turbine in idling mode and $0.02° \pm 0.15°$ respectively $-0.11° \pm 0.11°$ during power production, depending on the mean wind speed. As even small errors in the elevation will lead to large differences in the measurement height, especially for far measurement distances, we accounted for the misalignment by means of a correction function. The correction function used the power production of the turbine and the mean wind direction to determine pitch and roll. These values were then used to estimate the corrected measuring height across the scanned area. Height differences due to the curvature of the Earth were considered as well. An additional uncertainty was introduced by the tide, which varied approximately $\pm 0.6\,\mathrm{m}$. For simplicity, we neglected this influence.

The measuring height z_{meas} in Eq. (2.9) therefore varied with range gate and azimuth for each scan. Heights of wind vectors contributing to wind speed forecasts in this analysis spanned between a height of 20 m and 65 m, with a mean height of 36 m.

Wind vectors extrapolated to hub height were transformed in a final step to wind power values using the methodology and power curve introduced in Sect. 2.3.5. For the evaluation of the probabilistic wind power forecasts, we distinguished between stable or neutral and unstable atmospheric stratification. Situations with values of $-1\,000\,\mathrm{m} < L < 0\,\mathrm{m}$ were classified as unstable, while those with $0\,\mathrm{m} < L < 1\,000\,\mathrm{m}$ were defined as stable (Van Wijk et al., 1990). All other cases were defined as neutral.

2.4.2 Evaluation of methodology

Here, we aim to present the results of the individual methodical steps introduced previously. We assessed how the use of single-Doppler lidar measurements and the low scanning speed affected the lead time, availability and skill of the forecast. Further, the impact of the extrapolation to hub height was analysed (Theuer et al., 2020a). The data availability

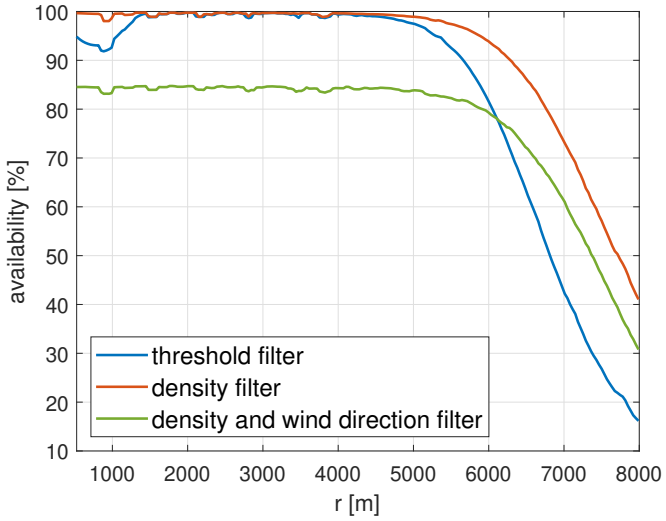

Figure 2.7: Data availability dependent on range gate when applying the threshold filter (blue) and the density filter (red). In green the availability after applying the density filter and neglecting the critical angles and wind speed outliers is depicted.

of all valid lidar scans dependent on range gate, applying different filtering methodologies, is compared in Fig. 2.7. Clearly, the availability of data was increased for far ranges when applying the density filter (red line) as compared to a CNR-threshold filter (blue line) with $-26.5\,\mathrm{dB} < \mathrm{CNR} < -5\,\mathrm{dB}$. While the data availability at a range gate of 7 km has already decreased to 42 % for the threshold filter, it still lies at 73 % when using the density filter. Also at close range gates from 500 m to 1450 m, the availability was increased from about 95 % to almost 100 %. The green line depicts the data availability after applying the density filter and additionally neglecting all other invalid data. That included the removal of wind speed outliers; however, the dominant effect was the omission of values within the critical region as described in Sect. 2.3.1. For the given measurement set-up and range gates up to 6 km, the availability was reduced to approximately 85 % of the density-filtered data. At 7 km it has decreased to 61 %. As the data availability was already reduced for far distances, the impact of further filtering was smaller compared to near ranges with higher data availability.

The number of observations at each measurement point in the polar coordinate system of the lidar before filtering is shown in Fig. 2.8a. Clear differences in the number of observations are visible as a consequence of the four scanning trajectories of the lidar (Fig. 2.1b). In accordance with the wind direction distribution (Fig. 2.6), north-westerly sectors were covered more frequently than southerly sectors. Figure 2.8b visualizes the number of observations after filtering not only dependent on range gate, but also on the azimuth angle. The single-Doppler lidar set-up caused the need to apply a VAD-fit and

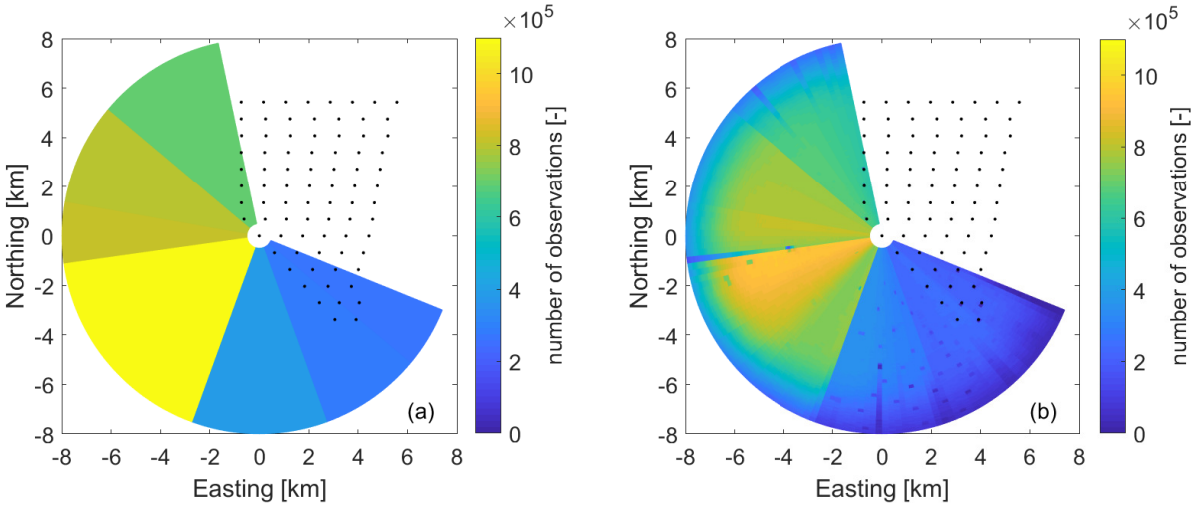

Figure 2.8: Distribution of measurements across the measurement domain as a result of varying lidar trajectories. The number of observations at each measurement point in the polar coordinate system of the lidar is visualized (a) before and (b) after data filtering. Filtering includes the density filter, the exclusion of critical regions and filtering of wind speed outliers.

as a consequence to filter certain regions of the scan, earlier referred to as critical regions. As an effect, data availability was significantly reduced. For instance, for the vicinity of the prevailing wind direction of approximately 300° (Fig. 2.6) the critical region defined by Eq. (2.2) ranges from 15° to 45° and 195° to 225°, i. e. the sectors perpendicular to the wind direction. Consequently, at an azimuth of 220° the availability was degraded from 1 085 000 observations to only 732 200, thus by about 32 %. Figure 2.9a shows how the availability of measurements impacted the number of valid forecasts for turbines T1-T7, depending on the scan's mean wind direction. The black line indicates the total number of valid scans, thus the maximal number of possible forecasts, available for the wind direction intervals. Compared to this, the number of valid forecasts is much lower for wind directions larger than 250° for turbines T5-T7. The forecast's quality, i e. the mean absolute error (MAE; Sect. 2.4.3), is also decreased for those wind directions, especially for T6 and T7 (Fig. 2.9b). Here, the lidar scans mainly covered the north-westerly inflow direction of the wind farm. Consequently and due to the layout of the wind farm, the area from which wind vectors are propagated to turbines T5-T7 in particular was not covered well by the lidar scan, resulting in reduced forecast availability and quality.

Also for wind directions ranging from 160° to 200°, the quality of forecasts at T5-T7 is lower compared to the other turbines. A similar problem occurred here as the turbines are placed within the scan area (Fig. 2.8). For the mentioned wind directions the area from which wind vectors can be propagated is thus considerably smaller, resulting in fewer available vectors and consequently higher forecast errors. Furthermore, vectors

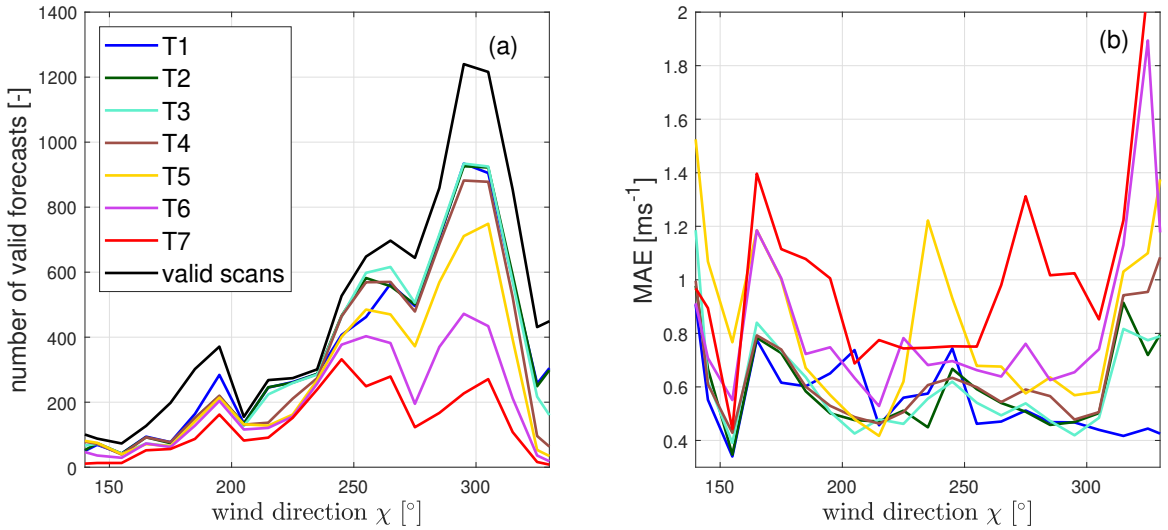

Figure 2.9: Number of valid forecasts (a) and mean absolute error (MAE; see Sect. 2.4.3) (b) for turbines T1-T7 as a function of wind direction χ sector of 10° width. The black line in (a) depicts the maximal number of possible forecasts, i. e. the number of valid scans, available for each wind direction.

contributing to the wind speed forecast originate from far range gates. Typically, in higher range gates the lidar has larger measurements errors and additionally the tangential distance between measurements is greater, resulting in less accurate interpolations to the Cartesian grid.

For wind directions larger than 310° an increasing MAE and a decreasing number of valid forecasts can be observed for turbines T2-T7. This is likely related to the interference with wakes. Due to the wind farm layout some vectors were advected through the wind farm area before reaching the target turbine. Even though wind vectors blocked by other turbines were not considered here, this simple advection technique cannot represent the more complex flow within the wind farm. A similar problem occurs for wind directions smaller than 150°, in this case mainly affecting T1-T5.

The application of the time synchronization method introduced in Sect. 2.3.2 extended the wind vector propagation time of the 5 min ahead forecast from 300 s to 420 s. The synchronization time t_{syn} was set to 30 s after the initialization of the scan (Sect. 2.4.1). That means, to reach the last time step of the scan at 150 s, not considering the measurement reset time, a propagation of an additional 120 s was required. The total scanning time hereby determines the additional propagation time. That means low scanning speeds reduce the maximal forecast lead times, in this case by 2 minutes.

Based on the data availability at different range gates, the maximal possible lead time of the forecast was determined. Even though we only considered partial load situations,

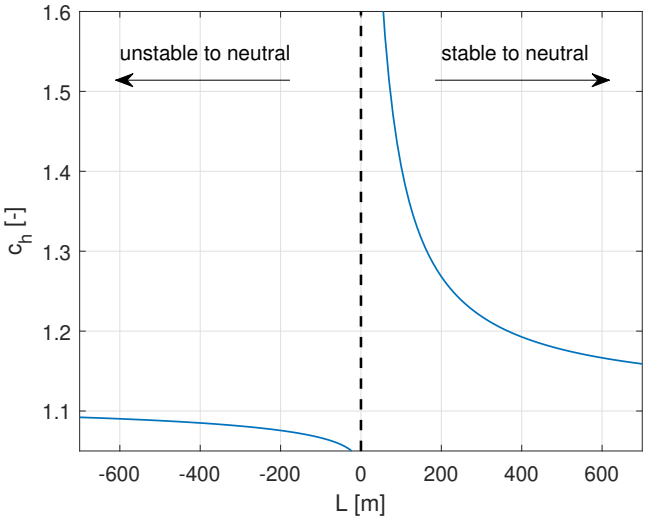

Figure 2.10: Dependence of the height extrapolation factor c_h on the Obukhov length L. In this example an extrapolation from 24.6 m to 92 m with a roughness length of $z_0 = 0.0002\,\mathrm{m}$ is shown.

i. e. situations with mean wind speeds up to $12\,\mathrm{m\,s^{-1}}$, higher wind speeds may have contributed to the wind speed distribution. Excluding those by choosing a too large lead time would thus falsify the results. Considering $15\,\mathrm{m\,s^{-1}}$ wind speeds, the measuring range needs to extend to 4 500 m for 5 min ahead forecasts and to 9 000 m for predictions with a lead time of 10 min. Taking into account the additional propagation time of 120 s, the measuring range would even need to be extended to 6 300 m and 10 800 m respectively. Due to the layout of the wind farm, turbines are often placed inside the scan, which can – depending on wind direction – lead to a reduction of the maximal possible advection distance. Taking this into account, combined with the fact that the data availability decreases with range, it is not possible to generate forecasts with lead times larger than 5 min using the available lidar scans.

The wind speed extrapolation to hub height is, following the method introduced in Sect. 2.3.4, mainly dependent on stability. Figure 2.10 shows the dependence of the height extrapolation factor c_h, calculated with Eq. (2.9), on Obukhov lengths L assuming an extrapolation from a height of 24.6 m to 92 m and a roughness length of $z_0 = 0.0002\,\mathrm{m}$. While the slope of the curve becomes small when approaching Obukhov lengths L with large magnitudes, thus neutral situations, especially for very stable cases $L \to 0$ the change of the correction factor with L is considerably larger. This consequently means misestimations of Obukhov length L have a larger impact on the wind speed extrapolation in stable situations. In order to determine this effect, we distinguished between stability cases in the following analysis. While during 55.5 % of the valid scans unstable atmospheric

stratification was observed, in 18.2 % the atmosphere was defined as neutral. Stable situations were observed in 26.3 % of the cases. To be able to evaluate unstable cases, during which we expect the highest errors in persistence compared to stable and neutral ones, separately and to level the number of analysed cases, we chose to combine stable and neutral situations for the analysis.

2.4.3 Deterministic wind power forecast

Deterministic forecast evaluation

Wind speed point forecasts were calculated as the mean of the predicted wind speed distributions. Forecasts (fc) were verified with 1 min mean SCADA data (obs) and using the root-mean-squared error (RMSE), mean absolute error (MAE) and bias. N denotes the total number of forecasts considered.

$$\mathrm{RMSE} = \sqrt{\frac{1}{N}\sum_{i=1}^{N}(\mathrm{fc}_i - \mathrm{obs}_i)^2} \tag{2.10}$$

$$\mathrm{MAE} = \frac{1}{N}\sum_{i=1}^{N}|(\mathrm{fc}_i - \mathrm{obs}_i)| \tag{2.11}$$

$$\mathrm{Bias} = \frac{1}{N}\sum_{i=1}^{N}(\mathrm{fc}_i - \mathrm{obs}_i) \tag{2.12}$$

As a reference, the benchmark persistence was used, which assumes the future value at $t+k$ equals the current value at time t, i. e. $\mathrm{fc}(t+k) = \mathrm{obs}(t)$.

Unstable stratification

Figure 2.11 compares 1 min mean SCADA wind power values of turbine T3 with persistence and the lidar-based forecasts (LF) in unstable atmospheric conditions. Both methods show an overall good agreement between forecast and observation with $R^2 = 0.80$ respectively $R^2 = 0.86$, with the LF's scatter being slightly smaller than that of persistence. The LF outperforms persistence in terms of RMSE and MAE. The lidar forecast's bias of 0.52 % is slightly larger than that of persistence with 0.31 %. The magnitude of the error is increasing with increasing power for both persistence and the lidar-based forecast. As the wind speed forecasting error was not found to increase with wind speed, the increase in error with power is attributed solely to the cubic nature of the power curve.

Table 2.1 summarizes the results of turbines T1-T7 for unstable situations for all valid forecasts and also shows the scores for only simultaneously available forecasts. During

unstable atmospheric stratification and for all available forecasts, the LF outperforms persistence for turbines T1-T4 in terms of RMSE and MAE, with the lowest RMSE observed for T1 and the largest improvement as compared to persistence for T3 with 20.1 %. The bias of those turbines is slightly larger than of persistence but rather small and not suggesting a systematic over- or underestimation of power caused by the model. T5 shows lower forecast skill and outperforms persistence only in terms of RMSE. The quality of the LF at T6 and T7 is below that of T1-T4 with a strongly reduced number of valid forecasts N. We attribute this to the turbines' position in an area not covered well by the lidar scans, which means fewer wind vectors can be propagated to the target turbines (Sect. 2.4.2). In Fig. 2.8b it can be observed that especially regions close to these turbines have low data availability. Low wind speeds, possibly originating from those areas, are thus not represented well in the wind speed distributions causing an overestimation of wind speed and power. Also for only simultaneously available forecasts, the LF outperforms persistence for all turbines except T6 and T7. The difference in quality is less distinct in that case, with the RMSE increasing by a factor of 1.8 instead of 2.4 from T3 to T7. While some of the quality differences observed for all available cases can thus be explained by the varying time intervals considered, this also confirms that forecast accuracy depends on the availability of wind vectors.

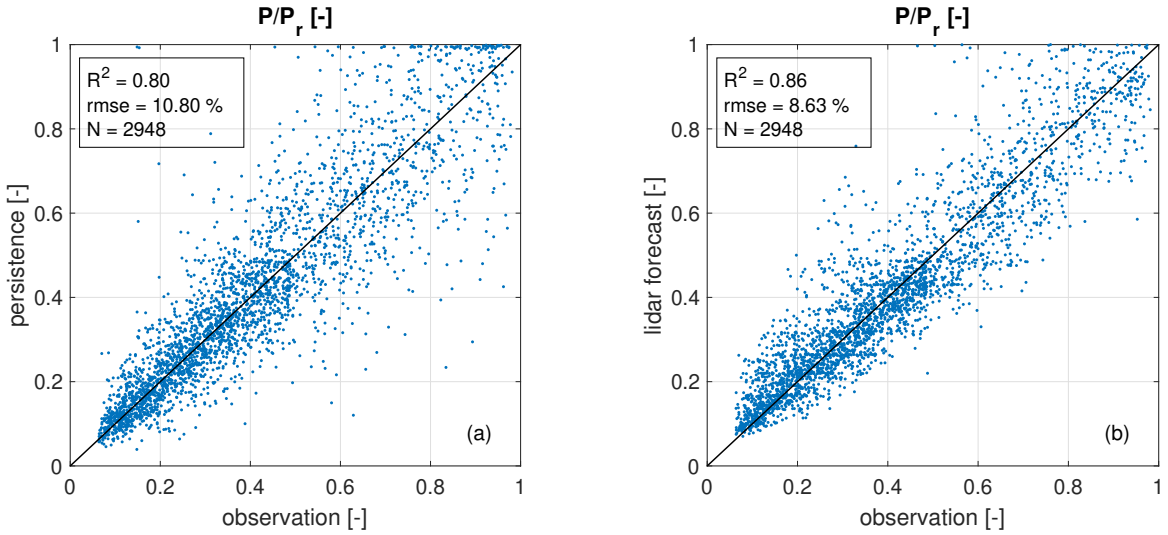

Figure 2.11: Comparison of 5 min ahead power forecasts at turbine T3 with 1 min mean SCADA data for (a) persistence and (b) the lidar-based forecast for *unstable* stratification. Values are given as a fraction of the turbine's nominal power.

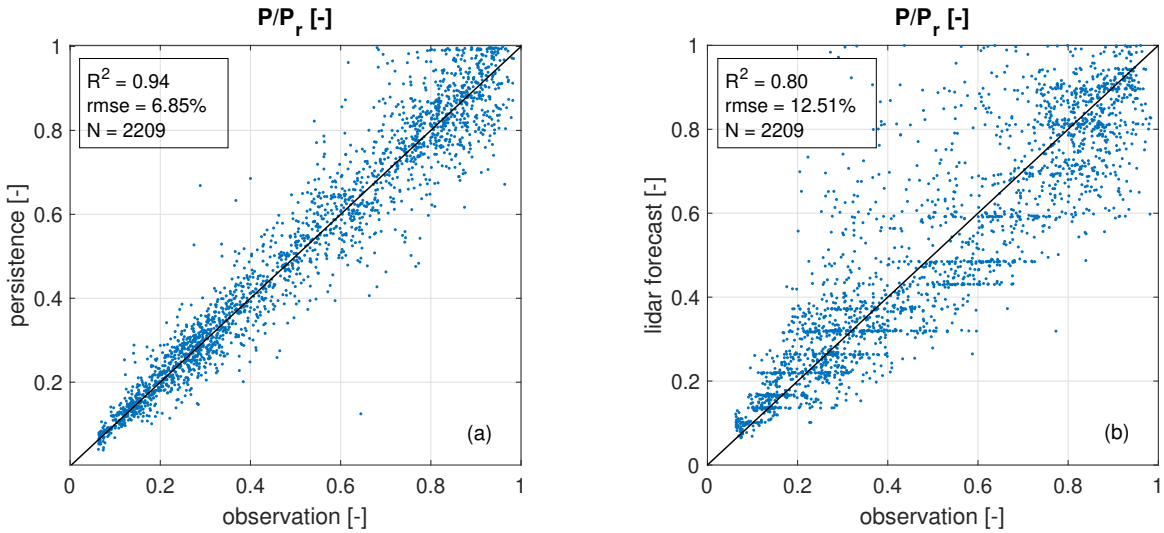

Figure 2.12: Comparison of 5 min ahead power forecasts at turbine T3 with 1 min mean SCADA data for (a) persistence and (b) the lidar-based forecast for *stable and neutral* stratification. Values are given as a fraction of the turbine's nominal power.

Table 2.1: Number of valid forecasts N, RMSE, MAE and bias for turbines T1-T7 for the lidar-based forecast and persistence during *unstable* stratification for all available forecasts and all simultaneously available ones. Scores are given in percent of the turbines' nominal power with the lowest values in bold.

		T1	T2	T3	T4	T5	T6	T7
	N	2510	2840	2948	2710	2048	640	297
RMSE [%]	lidar-based	**7.20**	**8.81**	**8.63**	**9.54**	**11.39**	13.87	21.07
	persistence	8.37	9.99	10.80	10.95	12.09	**10.94**	**11.35**
MAE [%]	lidar-based	**5.02**	**6.20**	**6.17**	**6.91**	8.53	10.53	16.67
	persistence	5.45	6.75	7.34	7.72	**8.63**	**8.28**	**8.88**
Bias [%]	lidar-based	-1.16	0.86	0.52	-0.24	-1.65	4.81	10.37
	persistence	**0.41**	**0.36**	**0.31**	**0.26**	**0.09**	**-1.54**	**-1.69**
	N	45	45	45	45	45	45	45
RMSE [%]	lidar-based	**9.26**	**9.75**	**7.91**	**7.73**	**8.23**	10.54	14.08
	persistence	10.52	9.80	12.78	10.14	12.10	**9.94**	**12.28**
MAE [%]	lidar-based	**6.77**	**6.84**	**5.92**	**6.28**	**5.97**	**7.63**	11.00
	persistence	8.08	6.97	9.72	8.10	10.08	7.92	**9.32**
Bias [%]	lidar-based	-4.31	-1.20	**-2.69**	-1.01	-2.37	**-0.29**	**-2.45**
	persistence	**-1.78**	**0.10**	-3.88	**-0.31**	**-2.28**	-2.08	-3.75

Stable and neutral stratification

Figure 2.12 shows the comparison of SCADA data and LF as well as persistence forecasts for stable and neutral atmospheric conditions at turbine T3. While the overall agreement

Table 2.2: Number of valid scans N, RMSE, MAE and bias for turbines T1-T7 for the lidar-based forecast and persistence during *stable and neutral* stratification. Scores are given in percent of the turbines' nominal power with the lowest values in bold.

		T1	T2	T3	T4	T5	T6	T7
	N	2013	2197	2209	2102	1273	1219	554
RMSE [%]	lidar-based	12.57	12.23	12.51	13.16	13.52	14.61	16.01
	persistence	**6.87**	**6.90**	**6.85**	**7.29**	**7.78**	**6.56**	**6.36**
MAE [%]	lidar-based	8.77	8.64	8.95	9.46	9.72	10.77	11.88
	persistence	**4.56**	**4.80**	**4.75**	**5.08**	**5.14**	**4.64**	**4.26**
Bias [%]	lidar-based	1.26	1.39	**0.18**	**0.01**	1.05	2.85	6.66
	persistence	**0.56**	**0.55**	0.39	0.78	**0.55**	**0.44**	**0.35**

between observation and forecast is good for persistence, larger scatter, a higher RMSE and MAE are observed for the LF. The plateaus, which can be observed in Fig. 2.12b, are an artefact of the transformation from wind speed to power. In cases where most wind vectors are placed within the same wind speed bin, the forecasted power will be close to the average power value of the corresponding wind speed interval (Fig. 2.5). Generally, persistence clearly outperforms the LF during stable and neutral conditions in terms of RMSE and MAE as summarized in Table 2.2. While the lidar forecast's bias for T3-T5 is lower than that of persistence, it shows a large overestimation of power, especially for T6 and T7. Similar to unstable cases, the quality and number of valid lidar-based forecasts decrease for turbines positioned in areas not well covered by the lidar scan. As in particular areas close to the turbines are not represented well (Fig. 2.8b), wind speed and power are being overestimated.

The quality of persistence is much better compared to unstable situations, due to lower wind speed fluctuations characteristic in stable situations (Stull, 2017). The lidar forecast's skill, however, is considerably lower compared to unstable situations. We attribute this to the extrapolation of wind speed to hub height. Variations in Obukhov length L and measuring height z_{meas} have a larger impact on the height extrapolation factor for stable situations compared to unstable situations, leading to larger errors in the case of misestimations. We will discuss this in more detail in Sect. 2.5.1.

2.4.4 Probabilistic wind power forecast

Probabilistic forecast evaluation

Probabilistic forecasts are generally evaluated by means of their sharpness and calibration. Sharpness describes the broadness of its distribution, while calibration estimates the consistency between the statistics of forecasts and observations (Gneiting et al., 2007). Both calibration and sharpness are estimated with the average crps:

$$\overline{\text{crps}} = \frac{1}{N}\sum_{i=1}^{N}\int_{-\infty}^{\infty}[F_i(x) - H(x - x_{0,i})]^2 dx. \tag{2.13}$$

Here, F denotes the cdf of the forecasted wind power, x_0 the observed wind power and H the Heaviside step function with $H(x - x_0) = 0$ for $x < x_0$ and $H(x - x_0) = 1$ otherwise.

To assess the forecast's calibration quantile-quantile reliability diagrams (Hamill, 1997) were used. A reliability diagram determines what percentage of the observations lies below a certain quantile of the forecasted distribution. Ideally, $j\,\%$ of the observation should lie below the jth percentile of the forecasts. Additionally, confidence intervals were estimated by means of a resampling technique to account for the varying number of values per bin and the varying number of valid forecasts for the different turbines (Hamill, 1997; Wilks, 2011). Again, forecasts were verified with 1 min mean SCADA data.

Also for the evaluation of probabilistic forecasts, persistence was used as a reference. Here, we generated a probabilistic persistence forecast by adding the errors of the 19 previous time steps to the forecast, as suggested by Gneiting et al. (2007).

Unstable stratification

In Table 2.3 the average crps of persistence and the LF are compared for turbines T1-T7 for unstable situations for all available forecasts as well as all simultaneously available ones. Here, forecasts of turbines T1-T4 are sharper and better calibrated than persistence, while for T6 and T7 persistence outperforms the LF. When considering only simultaneously available forecasts, persistence only outperforms the LF forecast for T7. These results are in good agreement with the deterministic scores, indicating that the LF achieves better quality in unstable conditions as long as sufficient wind field data are available.

An exemplary time series of the lidar forecast for unstable stratification is shown in Fig. 2.13. The turbine's 1 min mean SCADA power, the LF's mean values and persistence are plotted in blue, red and green, respectively. Each marker represents one forecast, generated with a temporal resolution of about 2.5 min. Shaded grey areas around the lidar forecast's mean indicate 5 % to 95 % prediction intervals in 10 % steps. Generally, the

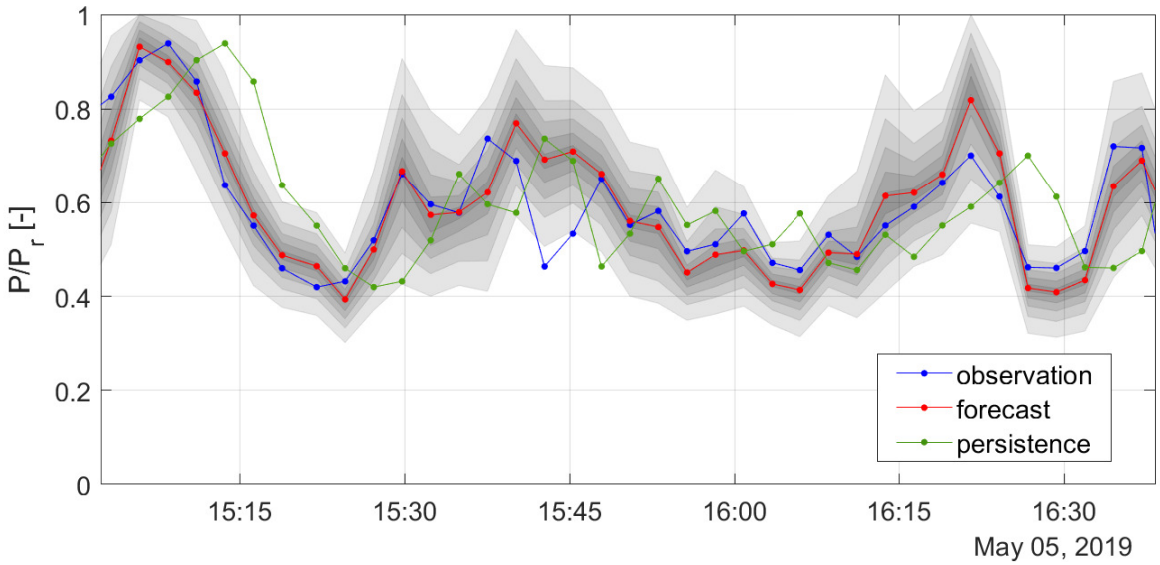

Figure 2.13: An example 1.5 h time series of 5 min ahead lidar power forecast for unstable stratification at turbine T3 shown in red. Confidence intervals are visualized as shaded grey areas from 5 % to 95 % in 10 % intervals. The blue curve shows 1 min mean SCADA data of T3, and the green curve persistence.

LF is able to follow the observed power more accurately than persistence does. Starting at 15:09 UTC a ramp event occurs, with a power drop from 92 % to 42 % within a time interval of 13.5 min. The LF predicts the ramp event quite accurately. Another extreme power drop of 40 % within 5 min can be observed at 16:21 UTC, also captured well by the lidar forecast. For both cases, persistence strongly overestimates the power. The width of the prediction intervals ranges from 18 % to 48 %. Broader intervals might be an indicator of higher uncertainties associated with the forecast. At all times except for two time steps, the intervals are able to capture the true power fluctuations. In 26 of the 37 depicted forecasts, the observed power lies within the 25 %-75 % interval and in five cases within the 45 %-55 % interval.

In Fig. 2.14 the reliability diagram of turbines T1-T7 is depicted for persistence as well as the lidar-based forecast for the unstable cases. For none of the seven turbines is persistence well calibrated, but it shows large discrepancies with the diagonal black line, which would indicate a perfect calibration. For T3 about 27 % lie below the 5 % quantile, while only 73 % lie below the 95 % quantile. All turbines have very similar reliability. The calibration of the LFs is in general better than for persistence, especially for turbines T2 to T4. For low quantiles, for all turbines $7\% - 14\%$ of the LFs lie below the 5 % quantile. Also taking the narrow confidence intervals assigned to those values into account, here the forecasts are comparatively well calibrated. For high quantiles, the turbines show large differences in reliability. While T3 is relatively well calibrated with 86 % below the

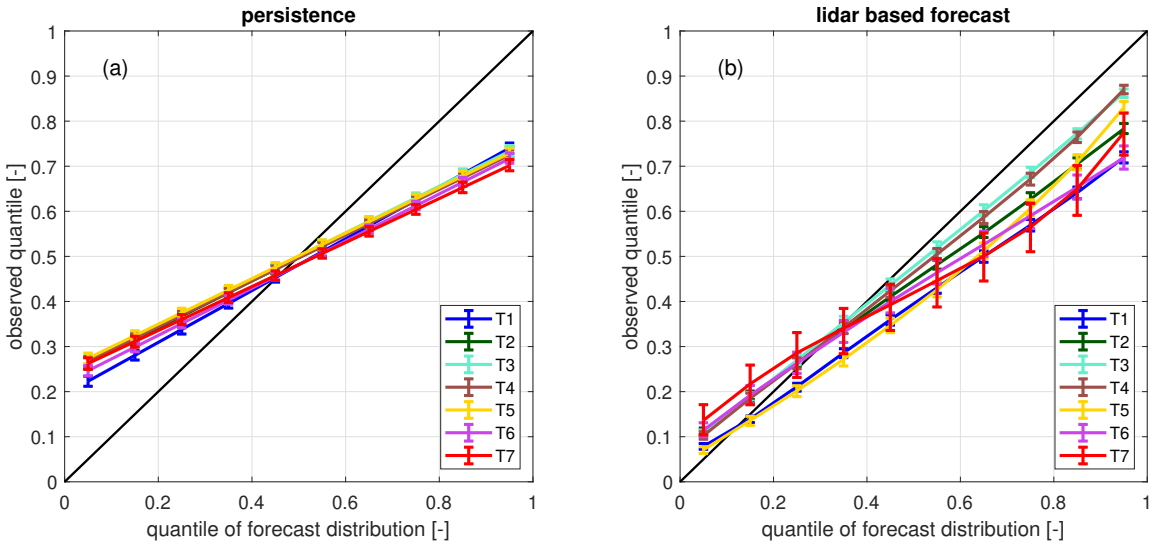

Figure 2.14: Reliability diagrams of all free-flow turbines of (a) the lidar-based forecast and (b) persistence for *unstable* stratification. The 95 % confidence intervals are visualized as error bars.

95 % quantile, T7 is hardly calibrated with a value of 77 %. The generally too low values for large quantiles suggest that a higher probability needs to be assigned to higher power values (Hamill, 1997).

Table 2.3: Number of valid forecasts N and average crps for turbines T1-T7 for the probabilistic lidar-based forecast and persistence during *unstable* stratification for all available forecasts and all simultaneously available ones. The crps is given in percent of the turbines' nominal power with the lowest values in bold.

		T1	T2	T3	T4	T5	T6	T7
	N	2510	2840	2948	2710	2048	640	297
$\overline{\text{crps}}$ [%]	lidar-based	**6.86**	**8.78**	**8.25**	**9.01**	**11.54**	12.35	19.22
	persistence	7.53	9.17	10.11	10.62	11.58	**11.49**	**11.61**
	N	45	45	45	45	45	45	45
$\overline{\text{crps}}$ [%]	lidar-based	**10.37**	**11.51**	**10.14**	**10.94**	**12.08**	**12.09**	18.54
	persistence	11.41	12.57	12.93	14.23	14.03	12.41	**12.60**

Stable and neutral stratification

We compare the average crps for stable and neutral conditions of persistence and the LF in Table 2.4. Here, persistence is generally more accurate than the LF. Again, persistence's quality is considerably better compared to unstable situations, while that of the LF is strongly reduced. The reliability diagrams depicted in Fig. 2.15 demonstrate

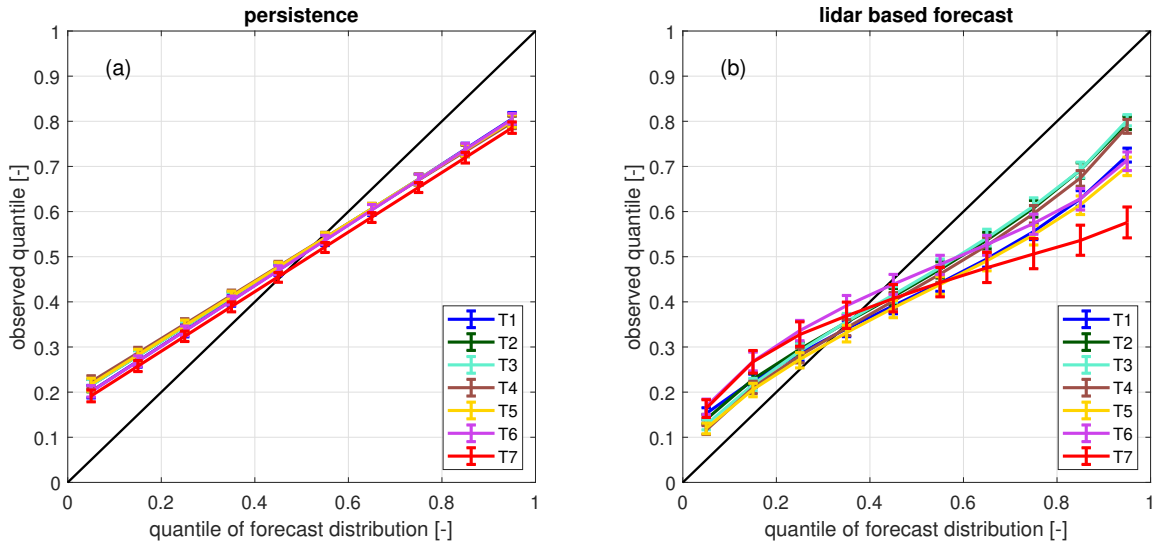

Figure 2.15: Reliability diagrams of all free-flow turbines of (a) the lidar-based forecast and (b) persistence for *stable and neutral* stratification. The 95 % confidence intervals are visualized as error bars.

Table 2.4: Number of valid forecasts N and average crps for turbines T1-T7 for the probabilistic lidar-based forecast and persistence during *stable and neutral* stratification. The crps is given in percent of the turbines' nominal power with the lowest values in bold.

		T1	T2	T3	T4	T5	T6	T7
	N	2013	2197	2209	2102	1273	1219	554
$\overline{\text{crps}}$ [%]	lidar-based	10.93	10.46	10.61	11.14	15.16	12.78	22.80
	persistence	**6.13**	**6.63**	**6.60**	**6.98**	**6.83**	**6.46**	**3.89**

that persistence is also better calibrated in stable and neutral cases, however, still about 20 % of the forecasts lie below the 5 % quantile while only about 80 % lie below the 95 % quantile. Again, all turbines show similar results. Using the LF, especially at high quantiles, fewer observations than expected lay below the respective quantiles, indicating that higher probabilities need to be assigned to larger values (Hamill, 1997). T2-T4 are best calibrated with 79 %-80 % below the 95 % quantile. For all other turbines, in particular those positioned in areas with low lidar scan coverage, results are worse than for persistence.

2.5 Discussion

We introduced a minute-scale forecasting methodology for long-range single-Doppler lidar measurements and used it to predict the power of seven free-flow turbines of the offshore

wind farm Global Tech I. The proposed model was developed as an extension of and an alternative to existing methods and is applicable to far-offshore sites. Emphasis was hereby put onto the use of single-Doppler lidar measurements compared to dual-Doppler radar set-ups. In the following, we discuss the model's ability to skilfully predict power under different atmospheric conditions. Moreover, limitations, possibilities and necessary adjustments concerning the forecast horizon are assessed. Finally, we qualitatively analyse the forecast uncertainty.

2.5.1 Forecasting skill for different atmospheric conditions

While the LF was able to predict wind power more reliably than persistence for unstable situations, the methodology failed when applied during stable stratification. Generally, we would expect the assumptions of a homogeneous wind field and negligible vertical wind speed component, which are the basis of the wind field reconstruction, to be less applicable during unstable situations when high amounts of thermal buoyancy cause strong vertical mixing (Stull, 2017). Also, the Lagrangian advection technique is expected to be more accurate for stable cases as during unstable situations vertical mixing considerably impacts the flow (Würth et al., 2018). Valldecabres et al. (2018b), for instance, found that for far ranges the applied wind field reconstruction methods, more specifically the higher arc length, could act as a low pass filter and consequently smooth out the wind speed fluctuations. This implies that in particular unstable situations cannot be predicted well. We, therefore, suppose that the low forecast skill observed during stable and neutral stratification is not related to the wind field reconstruction, but to the differences of measuring height and target height. That includes in particular errors in the extrapolation of wind speed to hub height. In Sect. 2.4.2 we have already shown that due to the nature of the stability-corrected logarithmic wind profile a mis-estimation of the Obukhov length L may have a strong impact on the forecast quality in stable situations. Other errors are possibly caused by an inaccurate estimation of the roughness length, a wrong estimation of the actual measuring height or a general inapplicability of the logarithmic wind profile. A more detailed analysis of errors associated with wind speed extrapolation of long-range lidar measurements by Theuer et al. (2020a) supports this interpretation.

Further, the height difference causes errors in wind vector advection. We chose to propagate wind vectors to the target turbines prior to the wind speed extrapolation. Vectors were thus propagated with lower wind speed at measuring height compared to that at hub height. This suggests wind vectors arrive at the turbines slightly delayed, with the extent of the delay related to the measuring height. We assume this reduces the forecast skill. As the increase in wind speed with height is larger during stable

stratification, we expect the effect to be more distinct for those cases. In this case study, the alternative, i. e. extrapolating wind speed before propagation, caused even larger errors compared to the ones presented in Sect. 2.4. That means, here the propagation of wind vectors associated with large errors due to wind speed extrapolation has a stronger impact on the forecast accuracy than the advection at lower heights.

For future applications, a more accurate description of the wind profile, especially in stable situations, is required to further improve the forecast skill. That also includes a more accurate estimation of stability and therefore demands reliable meteorological measurements. We thus suggest using buoy measurements for future applications instead of relying on OSTIA SST data (Sect. 2.4.1). Also accurate and undisturbed air temperature measurements at at least two heights might be a good alternative to determine atmospheric stability. Both approaches would incur additional equipment and operational costs. Additional profile information could, for example, be collected using range height indicator (RHI) lidar scans or data from a nearby met mast.

While the benchmark persistence yields good forecasts for stable and neutral situations, it has obvious shortcomings for strongly fluctuating situations and ramp events. Its comparison to the LF model has shown the latter's ability to predict such situations better (Fig. 2.13). In particular the probabilistic forecast has proven to be more skilful compared to persistence as it provides better-calibrated estimations of prediction intervals. We thus consider the lidar-based forecast a valuable addition to the benchmark persistence during unstable situations.

2.5.2 Forecast horizon and scanning trajectory

In this work, we developed a 5 min ahead power forecast. In order for remote-sensing-based forecasts to be useful for power grid balancing and electricity trading, the forecast horizon needs to be extended further (Würth et al., 2019). The accuracy of the lidar-based forecasts is expected to decrease with increasing lead times; however, Würth et al. (2018) found the accuracy of the state-of-the-art persistence to decrease faster. Lidar-based forecasts thus have the potential to bridge the gap between persistence and hour-ahead forecasts.

Small lidar systems suitable for offshore campaigns typically reach measurement distances from 8 km to a maximum of 10 km (Leosphere, 2018). Assuming a measuring distance of 9 km from the turbine's position and not considering reductions of lead time due to time synchronization, LFs can be used to predict a $10\,\mathrm{m\,s^{-1}}$ mean wind speed with variations of $\pm 20\,\%$ with a lead time of 12.5 min, $8\,\mathrm{m\,s^{-1}}$ mean wind can be predicted 15.6 min ahead. However, not only the maximal measurement distance and wind speed

but also the wind farm layout, scan geometry and wind direction have a significant impact on the lead time and quality of the forecast of individual turbines. We showed that forecasts for turbines positioned in an area not covered well by the lidar scan show low quality, and fewer situations can be forecasted compared to those placed in a well-covered area. Due to the limited area, a smaller number of wind vectors can be advected to the turbine of interest, resulting in lower forecast availability and larger biases. This is confirmed by Valldecabres et al. (2018a) who showed how reduced radar availability reduces the wind speeds that could be forecasted, the number of valid forecasts and quality of the forecast's calibration.

A large disadvantage of single-Doppler lidar data is the need to exclude a critical region with $75° < |\vartheta - \chi| < 105°$ as a consequence of the VAD fit (Sect. 2.3.1), which enhances this effect. The extent to which specific turbines are affected also depends on wind direction. Additionally, an inaccurate adjustment of the scanning trajectory to the wind direction can reduce data availability.

Furthermore, the long duration of the scans in this analysis caused the need for a time synchronization and reduced the achievable forecast horizon after the end time of the scan significantly (Sect. 2.3.3). Possibilities to reduce the scan time are (i) an increased scanning speed, which reduces the maximum measurement distance; (ii) a lower azimuthal resolution, which introduces errors to the wind field interpolation especially for far range gates; and (iii) a reduced total azimuth spanned, which further reduces forecast availability and quality for some of the target turbines. To make reliable statements regarding the optimal lidar position and scanning trajectory, a more detailed analysis of forecast quality for different wind directions and scan geometries is necessary. This should also include a study on the effect of reduced scanning time on forecast skill.

2.5.3 Uncertainty estimation and data availability

We already mentioned the errors attributed to the extrapolation of wind speeds to hub height, namely uncertainties in stability and wind profile estimation as well as an inaccurate determination of measuring height. While measuring at hub height would reduce the need for a wind speed extrapolation, it would introduce new challenges such as the correction for significant stationary and dynamic inclination of the scan plane due to the flexibility of the wind turbine tower and its dynamic excitation. In our case study, we had to correct for wind-speed-dependent platform inclination despite the fact that the lidar was positioned on a comparably stiff platform on a tripod foundation of the offshore turbine at GT I.

We further have to consider errors during the wind field reconstruction, including the

estimation of global wind direction by means of a VAD fit, assuming a homogeneous flow and neglecting the vertical wind component. Those wind direction errors; uncertainties in azimuth, elevation and range gate of the lidar system; and errors of the measured line-of-sight velocities all contribute to the uncertainties in the estimation of the horizontal wind field. The use of dual-Doppler instead of single-Doppler lidar data would allow for a more accurate estimation of horizontal wind speed components and would likely decrease the associated errors significantly. We further expect the propagation of wind vectors by means of their local wind speed and direction, both assumed constant along the entire trajectory, to introduce some uncertainties, enhanced by the errors assigned to its input parameters. Especially in situations where wind vectors were partially propagated through the wind farm area and turbines might have been affected by wakes, large errors were observed. Moreover, recent studies suggest the existence of a wind farm blockage effect (Bleeg et al., 2018), which might cause wind vectors to slow down when approaching the wind farm. Another large contribution to the overall forecast error is the transformation from wind speed to power values, as uncertainties in wind speed are magnified due to the cubic nature of the power curve. As discussed earlier, we found the above-mentioned uncertainties to depend not only on the lidar set-up but also on the atmospheric condition. Detailed knowledge of the forecast uncertainty is important to be able to further assess the possibilities and limitations of the proposed method and to reduce sources of error.

The variety of uncertainties associated with the model emphasize the importance of the probabilistic approach as it allows us to account for some of them. The area of influence hereby plays a crucial part to determine the probabilistic forecast. The AoI estimated in this case study is 5 times smaller than the one Valldecabres et al. (2018a) defined in their work, despite applying the same methodology. We explain this by the many factors influencing the crps and consequently AoI, i. e. the lidar wind field, the SCADA time series and the number of wind vectors available to be propagated. The difference in AoI suggests that it needs to be determined individually for each data set.

As already mentioned, the VAD fit caused the estimated wind direction to be constant across azimuth angles and only vary with range gates. This likely had an impact on the individual wind vectors reaching the area of influence. The uniform wind direction across range gates restricted the area from which vectors could be propagated to the target turbines. We assume this led to a mis-estimation, most likely an underestimation, of the spread of the observed wind speeds. Consequently, it is anticipated that the spread of the forecasted wind power distribution is too small. When using dual-Doppler lidar measurements, wind directions could be determined individually for each measurement point and the forecast's distribution represented more accurately.

Another limitation of the LF is its need for high data availability. Lidars send out laser pulses and use the backscattered signal to estimate wind speed. If not enough or too many aerosols are in the air, the signal becomes noisy (Newsom, 2012). That means for example during rain and fog, no accurate lidar measurements will be available and no forecast can be generated. One solution might be the development of a hybrid method that does not solely depend on the availability of lidar measurements.

2.6 Conclusions

We developed a methodology to forecast wind power of individual wind turbines on very short time horizons based on long-range single-Doppler lidar scans as a feasible alternative to existing remote-sensing-based forecasts that is applicable to far-offshore sites. The work is based on a probabilistic forecasting model developed for dual-Doppler radar measurements. It was extended to include a dynamic filtering approach, a time synchronization of the lidar scans and an extrapolation of wind speeds to hub height. The model was tested in a case study at the offshore wind farm Global Tech I. Here, we predicted wind power of seven free-flow wind turbines with a 5 min horizon. The lidar-based forecast was able to predict wind turbine power skilfully compared to the benchmark persistence during unstable atmospheric conditions, as long as sufficient wind field information was available in the region from which the wind vectors were propagated to the turbine of interest. During stable and neutral conditions the forecast quality was reduced. We mainly attribute this to higher uncertainties in the wind speed extrapolation to hub height during stable conditions, as a consequence of the nature of the stability-corrected logarithmic wind profile. To outperform persistence for stable situations, a more accurate description of the wind profile, e. g. using reliable meteorological information, is required.

Future work aims to include the modelling of wake effects in the forecast, allowing one to forecast power not only for free-flow turbines.

Chapter 3

Lidar-based minute-scale offshore wind speed forecasts analysed under different atmospheric conditions[b]

In recent years, the potential of remote sensing-based minute-scale forecasts to improve the integration of wind power into our energy system has been shown. In lidar-based forecasts, the wind speed is extrapolated from the measuring to the forecast height, i.e. the wind turbines' hub height, by assuming a stability-corrected logarithmic wind profile. The objective of this paper is the significant reduction of large forecasting errors associated with the height extrapolation. Hence, we introduce two new approaches and characterize their skill under different atmospheric conditions. The first one is based on an empirical set of parameters derived from lidar data and operational wind turbine data. The second approach derives the wind speed tendency of two consecutive forecasts at the measurement height and applies this to operational wind speed data at hub height. We identified the uncertainty in stability estimates and measurement height as the main cause for large extrapolation errors of the existing lidar-based forecast. Monte Carlo simulations revealed the new approaches' low sensitivity to uncertainty in lidar data processing, propagation and height extrapolation. Forecasting errors of a 5-minute-ahead wind speed forecast of free-flow turbines at an offshore wind farm were significantly reduced for the two newly developed methods as compared to the existing forecast during

[b]The content of this chapter is identical to the peer-reviewed version of the following journal article published in Meteorologische Zeitschrift: Theuer, F., van Dooren, M. F., von Bremen, L., and Kühn, M.: Lidar-based minute-scale offshore wind speed forecasts analysed under different atmospheric conditions, *Meteorologische Zeitschrift*, 31, 13-29, https://doi.org/10.1127/metz/2021/1080, 2021.

stable atmospheric conditions. Persistence could be outperformed during unstable and neutral atmospheric conditions and for situations with higher turbulence intensity. Overall, we found lidar-based forecasts to be less sensitive to atmospheric conditions than persistence. We discuss the importance of accurate vertical wind speed profile estimation, the advantages and shortcomings of the two newly introduced methods and their skill compared to persistence. In conclusion, the additional use of wind turbine operational data can significantly improve minute-scale lidar-based forecasts. We further conclude that the characterization of forecast skill dependent on atmospheric conditions can be valuable for decision-making processes.

3.1 Introduction

The increasing penetration of renewable energies in our power system causes a growing demand for skilful minute-scale wind speed and power forecasts (Würth et al., 2019). Such forecasts can be valuable tools for both the physical balancing, i. e. assuring grid stability, reducing curtailment and providing reserve power (Liang et al., 2016), as well as the economic balancing of power, i. e. for trading purposes (Cali, 2011). A variety of minute-scale forecasting methods has been investigated in the course of many years, including time series models such as persistence, ARMA (autoregressive moving average) and ARIMA (autoregressive integrated moving average) models (Würth et al., 2019; Torres et al., 2005), machine learning approaches and neural networks (Gendeel et al., 2018), spatio-temporal models (Lenzi et al., 2018), as well as hybrid approaches (Zhou et al., 2018). In recent years, potential of remote sensing measurements for minute-scale forecasts has been shown. In particular, scanning lidar or radar devices are used to gather wind field information upstream of wind farms or single wind turbines. Simple advection techniques proved useful to obtain information regarding the wind field reaching the downstream turbines several minutes later. For instance, a dual-Doppler radar-based forecasting methodology utilising radar data measured by two shore-based devices was successfully used to forecast wind power of individual and aggregated turbines in an offshore wind farm (Valldecabres et al., 2018a, 2020). Further, several studies have investigated the use of lidar measurements for minute-scale forecasting offshore (Theuer et al., 2020b), in a near-coastal area (Valldecabres et al., 2018b) and onshore (Würth et al., 2018).

The forecast skill was hereby found to be influenced by several parameters, such as the measurement set-up and wind farm layout, the measuring range and the data availability (Valldecabres et al., 2018a; Theuer et al., 2020b). Würth et al. (2018) found that also the

terrain plays a vital role in the accuracy of the forecast. Roughness as well as buoyancy effects prohibit the propagation of wind vectors across large distances, causing forecasts in complex terrain not to outperform the benchmark persistence. Similarly, buoyancy forces characteristic for unstable atmospheric conditions are expected to impact the advection technique's applicability and are considered responsible for lower forecast quality (Theuer et al., 2020b). Opposed to this, Theuer et al. (2020b) found that the quality of a lidar-based power forecast of free flow turbines in an offshore wind farm showed significantly reduced prediction quality for stable cases. The authors attributed those errors mainly to the extrapolation of wind speed to hub height. Also, Valldecabres et al. (2018b) observed forecasting errors during stable situations that were related to wind speed extrapolation.

A wind speed extrapolation to hub height is necessary for a remote sensing-based forecasting method whenever the measurements are performed at a height different from hub height. Current commercial lidar devices are in this context, contrary to radar devices, only able to measure one elevation angle when aiming to meet the requirements of short scanning periods and large scanning distances and angular ranges. Even when placing the devices on the nacelle of a turbine, dynamic turbine inclination, if recorded properly, would require a wind speed correction to hub height (Bromm et al., 2018). Despite these shortcomings, lidar-based forecasts are favourable compared to radar-based approaches, especially for offshore applications, where measurement devices need to be small and compact.

Typically, wind speed extrapolation is performed by means of a stability-corrected logarithmic wind profile (Peña et al., 2008). Logarithmic profiles are based on physical models, the most commonly used one being the Monin-Obukhov similarity theory (MOST). However, they are still subject to many assumptions, such as a constant wind direction with height (Optis et al., 2014). Additionally, uncertainty is introduced by incorrect input parameters. In a related study by the authors (Theuer et al., 2020a), uncertainty in Obukhov length L was identified as the primary contributor to extrapolation uncertainty, particularly during stable stratification. Also, wind speed uncertainties were found to have a considerable impact on the result. Similarly, Saint-Drenan et al. (2009) found that small errors in temperature estimation cause large errors in the extrapolated wind speed, especially during stable atmospheric conditions. Kelly and Jørgensen (2017) analysed the impact of roughness uncertainty on wind resource estimation. In the context of lidar-based forecasting, measuring height uncertainties are introduced by dynamic inclinations of the lidar device (Rott et al., 2022). Moreover, data processing algorithms can cause misestimations of wind speed (Schneemann et al., 2021).

Our objective in this paper is to significantly reduce errors of an existing lidar-based

forecast that occur under specific atmospheric conditions due to wind speed extrapolation to hub height (Theuer et al., 2020b). Three steps contribute to this. First, we investigate how wind turbine operational data can improve the height extrapolation of two new approaches. Second, we perform an analytical uncertainty estimation of the stability-corrected logarithmic profile and, for each method, Monte Carlo simulations to further account for uncertainties in lidar data processing, propagation and height extrapolation. Finally, we evaluate the different deterministic wind speed forecast methods with real measurements at free-flow turbines of an offshore wind farm. We compare the methods against the benchmark persistence and analyse different atmospheric conditions characterised by stability, wind speed increments and turbulence intensity.

3.2 Data description

To generate wind speed forecasts, we utilised horizontal Plan Position Indicator (PPI) lidar scans, performed at the offshore wind farm Global Tech I (GT I) in the German North Sea (Figure 3.1(a)) from March 2019 until June 2019. Figure 3.1(b) depicts the wind farm's layout with the lidar position marked in red. The wind turbines are of the type Adwen AD 5-116 with a rotor diameter of $D = 116\,\mathrm{m}$, a hub height of $z_{\mathrm{hh}} = 92\,\mathrm{m}$ and a rated power of $P_{\mathrm{r}} = 5\,\mathrm{MW}$. GT I consists of 80 turbines, thus has a total capacity of $P_{\mathrm{total}} = 400\,\mathrm{MW}$. Lidar measurements were performed by one Leosphere WindCube 200S (Serial no. WLS200S-024) placed on the transition piece (TP) of a westerly located wind turbine at a height of approximately 24.6 m above mean sea level. We used scans performed with an elevation of 0°, an averaging time of 2 s per measurement, an azimuthal resolution of 2°, spanning a total sector of 150°, and range gates ranging from 500 m to 8000 m with 35 m spacing. The probe volume length FWHM (full width half maximum) equals approximately 70 m. The scan duration was 150 s, plus an additional measurement reset time of approximately 6 s. Four different scan orientations were distributed within the sector $112° - 300°$ as indicated by the coloured lines in Figure 3.1(b). They were selected manually depending on wind direction. The lidar scans provided information regarding the line-of-sight (LOS) velocity, carrier-to-noise-ratio (CNR), azimuth angle, range gate, and time.

To calculate atmospheric stability, air pressure, as well as humidity and air temperature data were utilised. These were measured by two sensors (Vaisala PTB330 and Vaisala HMP155) positioned close to the lidar. Moreover, the OSTIA (Operational Sea Surface Temperature and Sea Ice Analysis) data set provided sea surface temperature (SST) daily at noon (Good et al., 2020), which was linearly interpolated to the lidar

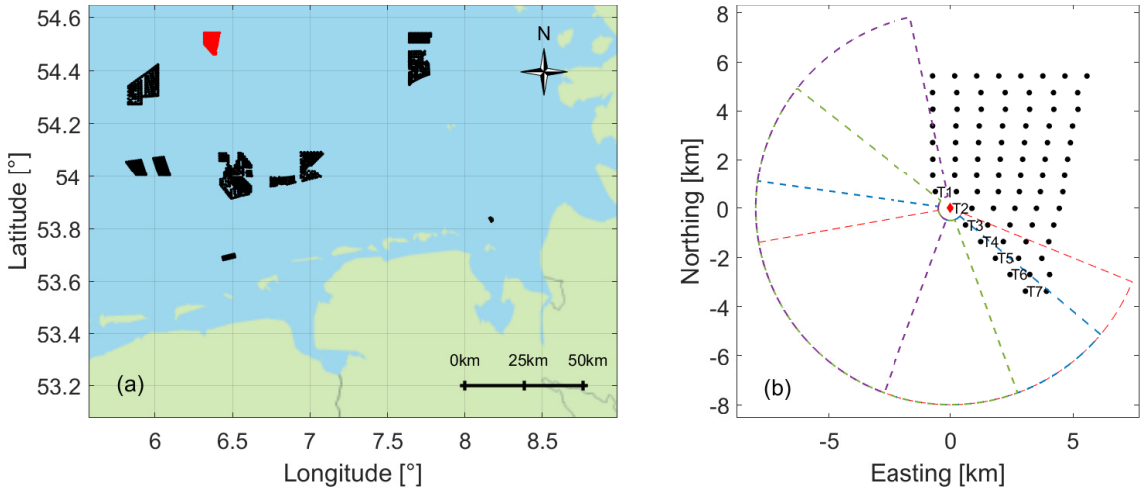

Figure 3.1: (a) Position of the offshore wind farm GTI in red and all other wind farms in the German and Dutch North Sea that were operational during the time of analysis from March 2019 until June 2019 in black. (b) Layout of the wind farm with the lidar's position and its four angular trajectories marked with different colours. Turbine T2 is defined as the origin of the coordinate system.

scans' timestamps.

For forecast evaluation, 1 Hz SCADA (supervisory control and data acquisition) data of the wind farm was available. This included wind direction, power, the operational status and a data quality flag of all turbines. Wind speed values were not measured but estimated from power, pitch angle and the SCADA system's turbine power curve. Forecasts were generated and evaluated by means of 1-minute-mean wind speed values for the seven wind turbines marked as T1-T7 in Figure 3.1(b). We excluded lidar scans with low data availability, situations with low-quality SCADA data, wind directions $\chi < 150°$ and $\chi > 310°$ and turbines operating below the cut-in wind speed of $4\,\mathrm{m\,s^{-1}}$ or above the cut-off wind speed of $25\,\mathrm{m\,s^{-1}}$ at hub height. Further, only situations with simultaneously available forecasts for at least turbines T1-T4 were considered. In total, 6 493 time steps with a temporal resolution of 156 s and distributed over the measurement period with valid forecasts for at least T1-T4 were evaluated in this case study. Figure 3.2 summarises these cases' wind conditions, where wind speed and direction values are mean values across the lidar scans at TP height (Section 3.3.1).

3.3 Methods

In the following, the lidar-based forecasting methodology, the wind speed extrapolation of the existing forecast as well as the extrapolation approaches of the two newly developed

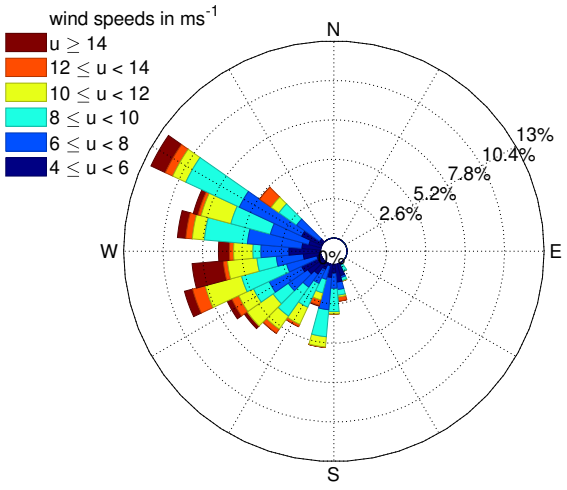

Figure 3.2: Distribution of wind speed and wind direction of the analysed situations. Wind speed and wind direction values are mean values across the scan area at TP height.

methods are introduced. We further explain the different uncertainty estimations of wind speed extrapolation to hub height.

3.3.1 Lidar-based forecasting

We applied a lidar-based forecasting methodology developed by Theuer et al. (2020b) and based on the work of Valldecabres et al. (2018a). First, lidar scans were filtered through a dynamic data filtering approach, which allows recovering data especially in far distances (Beck and Kühn, 2017). Second, we applied a Velocity-Azimuth-Display (VAD) algorithm to determine wind direction values $\chi(r)$ individually for each range gate r. The VAD-like fit is based on the assumption of a homogeneous wind direction across azimuth angles and a negligible vertical wind speed component (Werner, 2005). Wind direction values were further applied to determine horizontal wind speed information u_h at each measurement point using

$$u_\mathrm{h}(r,\vartheta) = \frac{u_\mathrm{LOS}(r,\vartheta)}{\cos(\vartheta - \chi(r))}, \tag{3.1}$$

where ϑ describes the azimuth angle and u_LOS the measured line-of-sight velocity. In a third step, lidar scans were synchronised in time, following a methodology developed by Beck and Kühn (2019) that was proven useful for applications in minute-scale forecasting (Theuer et al., 2020b). This step was necessary due to the device's low scanning speed, causing a time difference of 156 s between two subsequent measurements at some azimuthal position. After time synchronisation, wind vectors were propagated to the tar-

get turbines following a Lagrangian advection scheme (Valldecabres et al., 2018a). That means the vectors were assumed to travel with their local wind speed and wind direction and to maintain their trajectory throughout the advection period. Those reaching a predefined area of influence (AoI) around the target turbine within a time interval of $k \pm 30\,\mathrm{s}$, with lead time k, were selected to contribute to the wind speed forecast. The radius of the area of influence was optimised by minimising the root-mean-squared error (rmse, Section 3.4.3) of a 2.5-minute-ahead wind speed forecast at turbine T2. The AoI is computed individually for each stability class and forecasting approach. Forecasts were considered valid if a number of at least 20 wind vectors reached the AoI within the considered time interval.

The translation from wind speed at measuring height to wind speed at hub height varies for the different forecasting approaches and is explained in the following subsections. Here, measuring heights z_m varied with time and range gate due to a wind turbine rotor thrust dependent tilt of the lidar device (Rott et al., 2022) and the curvature of the Earth.

In a final step, the deterministic wind speed forecast was defined as the mean magnitude of all selected wind vectors that reached the target wind turbine.

Temperature difference-based forecast (TDF approach)

Following Theuer et al. (2020b), wind speed vectors were extrapolated to hub height by means of the logarithmic wind profile

$$u = \frac{1}{\kappa}\sqrt{\frac{z_0\, g}{\alpha_c}}\left(\ln\left(\frac{z}{z_0}\right) - \Psi\left(\frac{z}{L}\right)\right). \tag{3.2}$$

Here g denotes the gravitational acceleration, $\kappa = 0.4$ the von-Kármán constant, L describes the Obukhov length and z_0 the roughness length. The Charnock parameter was chosen as $\alpha_c = 0.011$ (Smith, 1980). L was determined utilising a method described by Sanz Rodrigo et al. (2015) based on the measured temperature difference and is further used to estimate the stability correction term Ψ. A more detailed explanation of the wind speed extrapolation to hub height, the stability estimation and the roughness length estimation can be found in Theuer et al. (2020b). We will refer to the lidar-based forecast using this wind speed extrapolation approach as temperature difference-based forecast (TDF) from now on.

Wind speed profile fit-based forecast (PF approach)

As an alternative to the aforementioned temperature-difference based calculation of L and z_0, we introduce a new approach that estimates the two parameters by fitting the

logarithmic wind speed profile (Equation (3.2)) to two wind speed values at two different heights for each time step. To do so, we utilised hub height SCADA wind speed values as well as propagated wind vectors. Wind vectors were advected to the target turbine at their measuring height as part of the wind speed forecast. For the fit only vectors of past time steps, i. e. measured before the forecast's initialisation, were considered. We used average wind speeds and average heights of wind vectors originating from the 30-minute-period before forecast initialisation, with their magnitude weighted according to their age. Thus, we assume the derived wind speed profiles will persist until the time of the forecast. As weighting function a Gaussian distribution centered around the time of the forecast initialisation and with a standard deviation of 15 minutes was used. Also hub height wind speeds were weighted and averaged. The fit used the previously calculated values of L and z_0 (Section 3.3.1) as an initial guess. However, this methodology is in principle independent of meteorological measurements at the site. Wind speed profile fits were performed individually for each of the analysed turbines. We will refer to this newly introduced approach as profile fit-based forecast (PF) in the following.

Tendency-based forecast (TF approach)

To reduce the extrapolation distance δz, i. e. the difference between measuring height and the height of interest, we introduce the tendency-based forecasting approach (TF). Here, consecutive wind speed forecasts at time instants t_{i-1} and t_i and corresponding measuring heights $z_\mathrm{m}(t_{i-1})$ and $z_\mathrm{m}(t_i)$ are determined using the methodology described at the beginning of Section 3.3.1. Hereby, t_{i-1} describes the current time and t_i the time to be forecasted. The wind speed at hub height dependent on time $u_\mathrm{hh}(t)$ can be expressed by means of the wind speed at measurement height $u_\mathrm{m}(t)$ and a time dependent correction factor $c_\mathrm{ex}(t)$:

$$u_\mathrm{hh}(t) = \frac{\ln\left(\frac{z_\mathrm{hh}}{z_0(t)}\right) - \Psi\left(\frac{z_\mathrm{hh}}{L(t)}\right)}{\ln\left(\frac{z_\mathrm{m}(t)}{z_0(t)}\right) - \Psi\left(\frac{z_\mathrm{m}(t)}{L(t)}\right)} u_\mathrm{m}(t) = c_\mathrm{ex}(t)\, u_\mathrm{m}(t). \tag{3.3}$$

Equation (3.3) can further be used to express $u_\mathrm{hh}(t)$ at the two consecutive time steps t_i and t_{i-1}. The quotient of the wind speed at hub height and the extrapolation from the measurement height is equated for the two time steps. Rearranging this identity yields

$$u_\mathrm{hh}(t_i) = \frac{c_\mathrm{ex}(t_i)}{c_\mathrm{ex}(t_{i-1})} \frac{u_\mathrm{m}(t_i)}{u_\mathrm{m}(t_{i-1})}\, u_\mathrm{hh}(t_{i-1}). \tag{3.4}$$

Obukhov length L and roughness length z_0 can be determined using meteorological

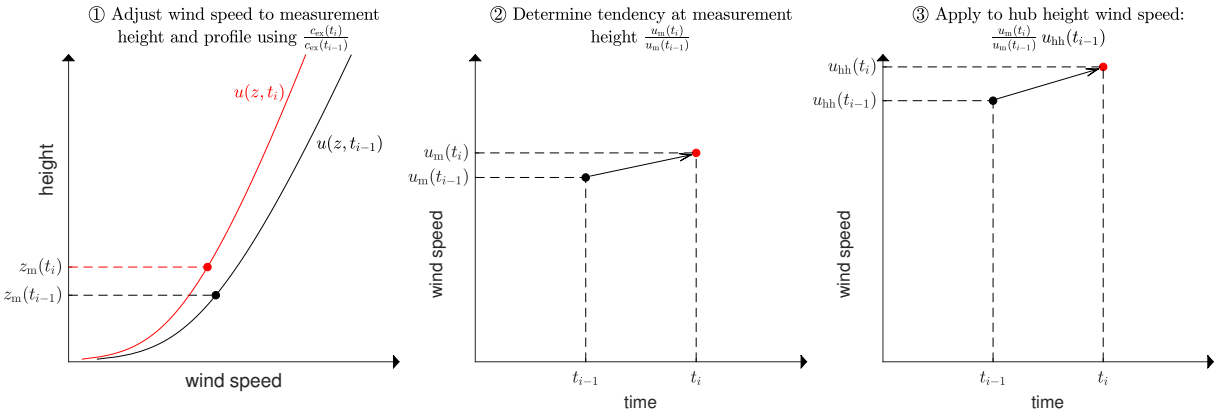

Figure 3.3: Tendency-based forecasting approach. First, the wind speed at time step t_{i-1} is adjusted to the profile described by L and z_0 and the measuring height z_m at t_i. Then a wind speed tendency at measuring height is determined and in a third step applied to wind speed observations at hub height.

measurements, following the approach described in Section 3.3.1, or by means of the fit described in Section 3.3.1. When assuming the atmospheric conditions do not vary significantly from t_{i-1} to t_i, i. e. $L(t_i) \approx L(t_{i-1})$ and $z_0(t_i) \approx z_0(t_{i-1})$ the expression 3.4 simplifies to

$$u_{hh}(t_i) = \frac{\ln\left(\frac{z_m(t_{i-1})}{z_0(t_i)}\right) - \Psi\left(\frac{z_m(t_{i-1})}{L(t_i)}\right)}{\ln\left(\frac{z_m(t_i)}{z_0(t_i)}\right) - \Psi\left(\frac{z_m(t_i)}{L(t_i)}\right)} \frac{u_m(t_i)}{u_m(t_{i-1})}\, u_{hh}(t_{i-1}). \tag{3.5}$$

Figure 3.3 illustrates the methodological steps of the TF: The term $\frac{c_{ex}(t_i)}{c_{ex}(t_{i-1})}$ in Equation (3.4) can be understood as the adjustment of the measured wind speed at t_{i-1} to atmospheric conditions and measuring height at t_i. When assuming constant L and z_0, the expression equals the correction factor of a wind speed extrapolation from $z_m(t_i)$ to $z_m(t_{i-1})$ (left fraction of Equation 3.5). The difference between $z_m(t_i)$ and $z_m(t_{i-1})$ is hereby significantly smaller than that of $z_m(t_i)$ and z_{hh}. We thus avoid the extrapolation across large height differences. Subsequently, the two consecutive forecasts at t_{i-1} and t_i at measurement height are used to derive a wind speed tendency, i. e. the relative change of wind speed from one time step to the other, expressed by the term $\frac{u_m(t_i)}{u_m(t_{i-1})}$ in Equation (3.4). The forecasted tendency is then applied to the current hub height wind speed $u_{hh}(t_{i-1})$, i. e. SCADA wind speed, to determine the future one $u_{hh}(t_i)$. Similarly as for persistence, the wind speed forecast in this method is based on the current wind speed observation. The lidar-based approach, however, allows to include information of the approaching wind field additionally.

In course of this work we tested three variants of the TF, i) using Equation 3.3 and meteorological parameters, ii) using Equation 3.3 and fitted parameters and iii) using

Equation 3.5 and meteorological parameters. No significant quality differences were observed between the three variants. In the following we will therefore show the results of the simplified case iii) only.

3.3.2 Uncertainty estimation of lidar-based forecasting approaches

Previous studies have suggested that lidar-based forecasting errors are largely caused by errors in wind speed extrapolation (Theuer et al., 2020b). We therefore performed an analytical uncertainty estimation of the wind speed extrapolation based on a logarithmic stability-corrected wind profile. This analytical approach does not account for uncertainties related to the wind vector propagation, but focuses solely on the wind speed extrapolation. It is considered a good representation of the uncertainty for the TDF only, as the wind profile of the PF is based on a fitting approach and the TF only indirectly applies the logarithmic profile. Nevertheless, this uncertainty estimation is considered valuable to characterise the shortcomings of wind speed extrapolation by means of a logarithmic profile in more detail.

As a second method for uncertainty estimation, we performed Monte Carlo simulations. They allow to determine uncertainties related to all three approaches and include uncertainties related to the lidar data processing, wind vector propagation and height extrapolation. Moreover, they consider possible numerically introduced uncertainties and provide a metric that is directly linked to the case study analysed in this work.

Uncertainty estimation related to the logarithmic wind profile

A theoretical uncertainty estimation is possible based on the analytical expression for the stability-corrected logarithmic wind profile (Equation 3.2). We applied Gaussian uncertainty propagation to Equation (3.3) to determine the total uncertainty Δy

$$\Delta y = \sqrt{\sum_i \left(\left| \frac{\delta y}{\delta x_i} \right| \Delta x_i \right)^2}, \tag{3.6}$$

using the uncertainties of the input variables Δx_i.

The wind speed extrapolation uncertainty Δu_{hh} as a function of the measured wind speed uncertainty Δu_{m}, the roughness length uncertainty Δz_0, the measurement height uncertainty Δz_{m} and the stability term uncertainty $\Delta\Psi$ was derived in more detail by Theuer et al. (2020a). The uncertainty of the stability correction term $\Delta\Psi$ was expressed

Table 3.1: Input variables used for the analytical uncertainty estimation and standard deviations of error distributions used for the Monte Carlo simulations. For the analytical uncertainty estimation, we used twice the stated standard deviation.

variable	input value	standard deviation
LOS wind speed	-	$0.2\,\mathrm{m\,s{-}1}$
azimuth	-	$0.025°$
wind direction	-	$1°$
propagated wind vectors	-	$0.1\,\mathrm{m\,s{-}1}$
pitch	-	$0.025°$
roll	-	$0.025°$
measurement height	24.6m	0.3m
SCADA wind speed	-	$0.05\,\mathrm{m\,s{-}1}$
wind speed at lidar position	$8.2\,\mathrm{m\,s{-}1}$	$0.05\,\mathrm{m\,s{-}1}$
air temperature	$\{1, 1.2, ..., 23\}°\mathrm{C}$	$0.05°\mathrm{C}$
water temperature	$\{6, 6.2, ..., 18\}°\mathrm{C}$	$0.1°\mathrm{C}$
pressure	$1011.81\,\mathrm{hPa}$	$0.15\,\mathrm{hPa}$
humidity	$80.69\,\%$	$0.6\,\%$
roughness length	$9 \cdot 10^{-5}\,\mathrm{m}$	$4.5 \cdot 10^{-6}\,\mathrm{m}$

as a function of the Obukhov length uncertainty ΔL and the height uncertainty Δz. While so far ΔL was assumed to be a constant, we here estimated it using uncertainties in meteorological measurements used to calculate L. Input variables were the TP height z_{TP} and wind speed at TP height u_{TP}, air and water temperature T_{TP} and T_0, humidity H and pressure p, and all associated uncertainties. More details on the estimation of L and its uncertainty can be found in Schneemann et al. (2021). Table 3.1 summarises the values of all input variables used for the analytical uncertainty estimation. Air and water temperature, pressure, humidity and wind speed were defined in accordance with the measured values during the analysed time period. Uncertainties were chosen following typical values suggested in the respective sensor's user manual. All uncertainty terms used in the analytical uncertainty estimation correspond to twice the standard deviation indicated in Table 3.1 and are thus considered to include 95 % of all errors.

Uncertainty estimation related to lidar data processing, propagation and height extrapolation

For uncertainty estimation of lidar data processing, wind vector propagation and the PF's and TF's height extrapolation no analytical description is available. Thus, no analytical uncertainty estimation can be computed. However, Monte Carlo simulations for each

of the three approaches can be applied. Monte Carlo simulations rerun the forecast N times with varying input variables. The Monte Carlo runs provide many possible outcomes based on the variations of the input parameters. The standard deviation of these is considered a representation of the results' uncertainty. The input parameters were randomly selected using previously defined error distributions (Zhao et al., 2018). In this case, we performed simulations with $N = 1000$ repetitions and errors normally distributed around a mean error value of zero. The wind fields determined from lidar scans were hereby subject to LOS wind speed, azimuth and wind direction errors. Errors in wind vector propagation were expressed by adding a random wind speed error to vectors contributing to the forecast. Height errors were characterised in terms of pitch and roll error, which define the lidar's tilt (Rott et al., 2022). Thus, height errors increased with measurement distance to the device. A visualization of pitch and roll uncertainty and other uncertainties related to long-range lidar measurements can be found in Figure 2 of Schneemann et al. (2021). Errors in L and z_0 were realised considering errors in air and water temperature, pressure, humidity and the wind speed at lidar position.

For each analysed time step, a new set of N random errors was selected from each variable's error distribution. We are aware that errors are not uncorrelated between time steps, however, we chose this approach for simplicity reasons. The only errors we consider correlated between time steps are LOS wind speed and azimuth pointing errors, and thus here the same N errors were assigned to all analysed time steps. Also this assumption can be understood as a simplification.

The uncertainties assigned to the input variables are summarised in Table 3.1.

3.4 Results

In the following, we present the results of the two uncertainty analyses (Section 3.4.1). Further, the case study is analysed, evaluating the estimated vertical wind speed profiles (Section 3.4.2) and the minute-scale wind speed forecasts (Section 3.4.3).

3.4.1 Uncertainty estimation of lidar-based forecasting approaches

Uncertainty estimation related to the logarithmic wind profile

As described in Section 3.3.2, we analysed the dependency of ΔL and further Δu_{hh} on L. We calculated ΔL, with input variables defined in Table 3.1. Figure 3.4(a) shows the dependency of ΔL on L on the left y-axis. ΔL approaches zero for $L \to 0\,\mathrm{m}$ and

infinity for $L \to \infty$. At $L = 200\,\mathrm{m}$, ΔL has already increased to 49 m. For $L = -200\,\mathrm{m}$ the uncertainty is slightly smaller with $\Delta L = 46\,\mathrm{m}$, due to the definition of L. The curve's overlapping regions were caused by varying absolute temperature values, which resulted in the same value for L, but slightly differing ΔL.

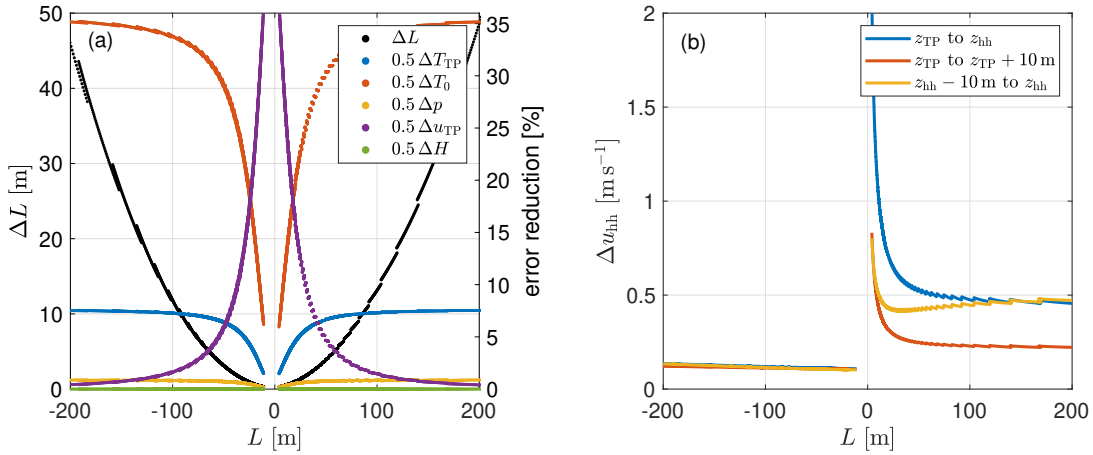

Figure 3.4: Analytical estimation of the wind speed extrapolation uncertainty. In (a) the uncertainty of L is shown in black with ΔL on the left y-axis. As coloured lines on the right y-axis, the reduction of ΔL for reducing the error of one of the contributors by 50 % is visualised. In (b) the wind speed extrapolation uncertainty Δu_{hh} is depicted for varying extrapolation distances dependent on L.

To understand the impact of the different contributions to the overall uncertainty, we reduced the individual uncertainty contributions to 50 % of their initially defined value. The reduction of ΔL is shown on the right y-axis for variations of ΔT_{TP}, ΔT_0, Δp, Δu_{TP} and ΔH. While an increase of accuracy for humidity and pressure had none to little impact, a reduction of Δu_{TP} could significantly reduce ΔL, especially during very stable and very unstable situations ($|L| \to 0$). Approaching neutral situations, the most considerable impact can be attributed to the temperature uncertainties, particularly the water temperature uncertainty. Since in very stable or unstable scenarios, the temperature errors are small compared to the temperature difference; they have a smaller impact on the stability estimation.

Figure 3.4(b) visualises how the wind speed extrapolation uncertainty Δu_{hh} changes with L. Variables were defined as stated in Table 3.1. Theuer et al. (2020a) have previously found that the two main contributors to the wind speed extrapolation uncertainty are the components of the stability correction terms, i. e. $\left|\frac{\delta u_{\mathrm{hh}}}{\delta \Psi}\right| \Delta \Psi$, and the wind speed component, i. e. $\left|\frac{\delta u_{\mathrm{hh}}}{\delta u_{\mathrm{m}}}\right| \Delta u_{\mathrm{m}}$. We thus focus on theses contributors here. In neutral conditions, i. e. $|L| \to \infty$, the wind speed component contributes strongly to Δu_{hh}. The stability correction terms Ψ_{m} and Ψ_{hh} become zero while $\Delta \Psi_{\mathrm{m}}$ and $\Delta \Psi_{\mathrm{hh}}$ approach a

limit related to water and air temperature uncertainties and the considered heights. When L approaches zero in stable cases, both $\Delta\Psi$ as well as $|\Psi|$ approach infinity. The overall contributions of the stability terms approach infinity and they dominate Δu_{hh}. In unstable cases this is also true; however, $\Delta\Psi$ will increase only from very small $|L|$ onwards, dependant on the input parameters. Therefore this increase is hardly visible in Figure 3.4(b) and will most likely not impact many of the considered cases.

Further investigation has shown that Δu_{hh} and all of its sub-components increase with extrapolation distance, as visualised in Figure 3.4(b). Here, the wind speed extrapolation uncertainty Δu_{hh} is shown for reduced extrapolation distances of 10 m in a lower region of the wind speed profile in red and in a higher one in yellow. As a change of extrapolation distance was found to mainly impact errors associated with the stability terms and wind speed, its reduction will have the most considerable effect during stable stratification when these terms have a larger contribution to the wind speed extrapolation uncertainty (Theuer et al., 2020a). It is also visible that uncertainties are smaller in lower regions of the logarithmic wind profile.

Uncertainty estimation related to lidar data processing, propagation and height extrapolation

Figure 3.5 depicts the standard deviation of the Monte Carlo simulations σ_{mc} described in Section 3.3.2 dependent on Obukhov length L with 117 values per bin and 95 % confidence intervals visualised as error bars. In accordance with the results of the analytical error analysis of the wind speed extrapolation (Section 3.4.1) values are larger in stable compared to unstable situations for the TDF, with particularly large uncertainties during very stable situations. The TF shows a similar pattern during stable cases, however, with significantly lower uncertainties. For both approaches the large uncertainty in u_{hh}, i. e. σ_{mc}, is caused by the high sensitivity of c_{ex} to the input variables. As for the TF the ratio of c_{ex} values of two consecutive time steps is considered, its variation does have a smaller impact on the overall result than for the TDF. Similarly, also variations of wind speed have less influence on the TF. During unstable cases, the uncertainty of SCADA wind speed dominates the overall uncertainty of the TF, resulting in larger uncertainties compared to the TDF.

The profile fit shows almost constant σ_{mc} for different L. The fitting algorithm can adjust for variations in the input variables. Likewise to the TF, the uncertainty of SCADA wind speeds dominates σ_{mc}. The PF's uncertainty is larger than the TDF's during unstable cases but can outperform both TDF and TF during stable situations.

Overall, the results indicate that the two alternative approaches of wind speed ex-

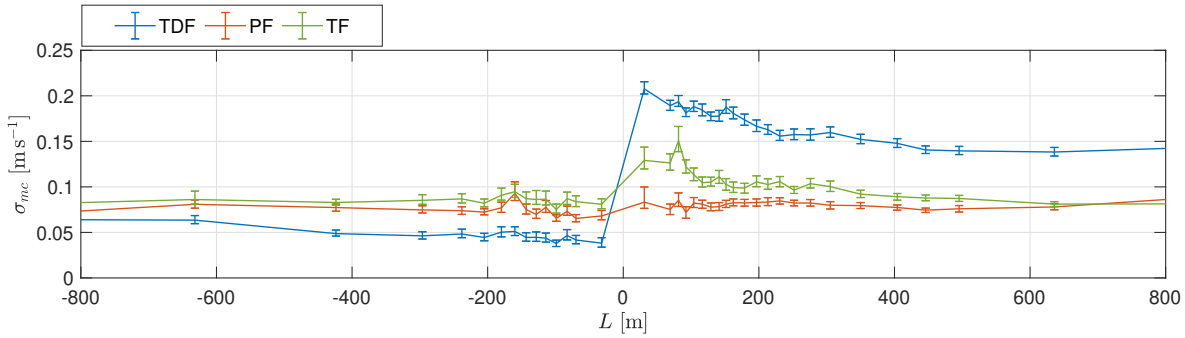

Figure 3.5: Standard deviation of Monte Carlo simulations dependent on Obukhov length L for the different forecasting methodologies. The 95 % confidence intervals are visualised as error bars. Each bin contains 117 values.

trapolation, i. e. PF and TF, are less sensitive to flawed estimations of input parameters during stable situations, which means a lower uncertainty can be assigned to the forecasts. One should, however, be aware that the absolute values σ_{mc} are strongly dependent on the error distributions' standard deviations. Further, the impact of different variables on the results varies for different approaches.

3.4.2 Estimation of vertical wind speed profiles

In Section 3.3.1 we used two methods to determine the parameters z_0 and L. The first is based on a physical estimation (TDF), while the latter is based on an empirical fit (PF). This section compares the estimated parameters of TDF and PF to gain insight into the advantages and shortcomings of the different methodologies.

Figure 3.6(b) plots the corresponding values of the roughness length z_0 against each other, using the two methods for turbines T1-T4. Here, two clusters can be distinguished. In the first, the TDF and PF roughness lengths are scattered around the black diagonal line, indicating perfect agreement. In the second cluster, the PF values are about 4.5 times larger than the ones of the TDF, which is discussed in Section 3.5.1. Figure 3.6(a) visualises the distribution of L for both the TDF and PF with bins of 50 m width. In the histogram, it stands out that the number of very unstable cases, i. e. cases with $-50\,\mathrm{m} < L < 0\,\mathrm{m}$ is much larger for the fit (PF) than the temperature-difference estimation (TDF). This can be explained with the help of Figure 3.7(a), which shows the relation of L and the wind speed difference between measuring height and hub height $\delta u = u_{\mathrm{hh}} - u_{\mathrm{m}}$ for both the TDF and PF. As reference the wind speed difference determined using the MOST is shown in black dependent on L and for mean values of measuring height $z_m = 36\,\mathrm{m}$ and roughness length $z_0 = 9 \cdot 10^{-5}\,\mathrm{m}$. Additionally, the frequency of stability classifications is given within

each panel in Figure 3.8(a) as a percentage of the total number of values considered. We defined the five stability classes very unstable ($-200\,\mathrm{m} \leq L < 0\,\mathrm{m}$), unstable ($-1000\,\mathrm{m} < L < -200\,\mathrm{m}$), neutral ($|L| >= 1000\,\mathrm{m}$), stable ($200\,\mathrm{m} < L < 1000\,\mathrm{m}$) and very stable ($0\,\mathrm{m} < L \leq 200\,\mathrm{m}$), which are shown on the x-axis for the TDF and on the y-axis for the PF. Panels positioned on the diagonal therefore represent situations with the same stability class for both the TDF and PF. Figure 3.8 will be presented in more detail in Section 3.4.3. The fitting algorithm classified profiles as very unstable when wind speed values decreased or stayed constant with height. While for situations $\delta u > 0\,\mathrm{m\,s^{-1}}$, the resemblance of the PF results and the theoretical estimation by means of MOST is high, for very unstable cases, δu determined with the MOST approaches $0\,\mathrm{m\,s^{-1}}$. Those cases also corresponded to the situations with increased values of z_0 as visualised in Figure 3.7(b). During many situations z_0 stayed almost constant at a low value, i. e. L was the main parameter used to influence the profile. When L was quite restricted by the negative wind speed difference with height, z_0 played a more important role, thus was assigned a larger value. While most of these situations were estimated as unstable (Figure 3.7(a)) by means of the temperature difference, 19 % were defined as neutral and 15 % as stable. An evaluation (cf. Figure 3.8(a)) revealed that about 3.5 % of all analysed cases were classified as stable by the TDF but fitted as unstable cases by the PF. That includes, besides situations with decreasing wind speed with height, also many with only slightly increasing wind speed of up to approximately $0.6\,\mathrm{m\,s^{-1}}$. Conversely, in 4.5 % of all situations, cases classified as unstable by the TDF were classified as stable by the PF. Here, the increase of wind speed with height was larger with about $0.8\,\mathrm{m\,s^{-1}}$ to $2.0\,\mathrm{m\,s^{-1}}$.

3.4.3 Minute-scale wind speed forecasting

5-minute-ahead wind speed forecasts at the turbines T1-T7 were generated using the three introduced extrapolation approaches, i. e. i) the temperature difference-based forecast (TDF approach), ii) the wind speed profile fit-based forecast (PF approach) and iii) the tendency-based forecast (TF approach). As a reference a persistence forecast was used. Persistence is considered a benchmark in minute-scale forecasting and is based on the assumption that the current value will persist until the time of the forecast (Würth et al., 2019). For further analysis only situations with valid forecasts for all three approaches and simultaneously available forecasts for turbines T1-T4 were considered (Section 3.2). The root-mean-squared error (rmse)

$$\mathrm{rmse} = \sqrt{\frac{1}{N}\sum_{i=1}^{N}(\mathrm{fc}_i - \mathrm{obs}_i)^2} \tag{3.7}$$

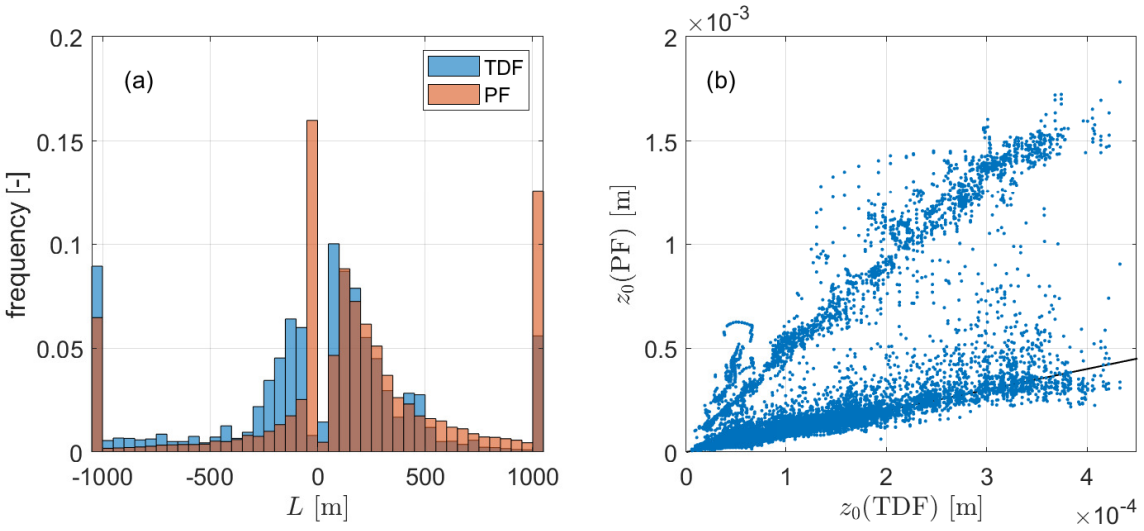

Figure 3.6: Comparison of TDF and PF wind profile parameters. In (a) the histograms of the Obukhov length L are shown in bins with 50 m width. The outermost bins represent all values with $L < -1000\,\mathrm{m}$ and $L > 1000\,\mathrm{m}$, respectively. In (b) the roughness length z_0 is compared for the TDF on the x-axis and the PF on the y-axis. The black line indicates perfect agreement between z_0 of TDF and PF.

and the bias

$$\mathrm{bias} = \frac{1}{N}\sum_{i=1}^{N}(\mathrm{fc}_i - \mathrm{obs}_i) \tag{3.8}$$

of the forecasts fc_i were determined by comparison with the observations obs_i, i. e. 1-minute-mean SCADA wind speed values. Here, N denotes the number of forecasts considered in the (sub-)dataset.

To compare the forecast skill to a reference forecast, the skill score expressed as percentage

$$\mathrm{rmse\ ss} = 100\left(1 - \frac{\mathrm{rmse}}{\mathrm{rmse}_{\mathrm{ref}}}\right) \tag{3.9}$$

was used. The bias skill score (bias ss) was determined accordingly. The skill score equals 100 % for a perfect forecast with $\mathrm{rmse} = 0$ or $\mathrm{rmse} << \mathrm{rmse}_{\mathrm{ref}}$ and is negative for $\mathrm{rmse} > \mathrm{rmse}_{\mathrm{ref}}$.

In the following, we first assess the profile fit and tendency approach applied to T1-T4 before comparing the skill of all forecasting methodologies.

Comparison of wind speed profile fit-based forecast and temperature difference-based forecast

The previous section revealed the partially large differences between the stability classes defined by the TDF and the PF. We therefore analyse how the estimated stability class

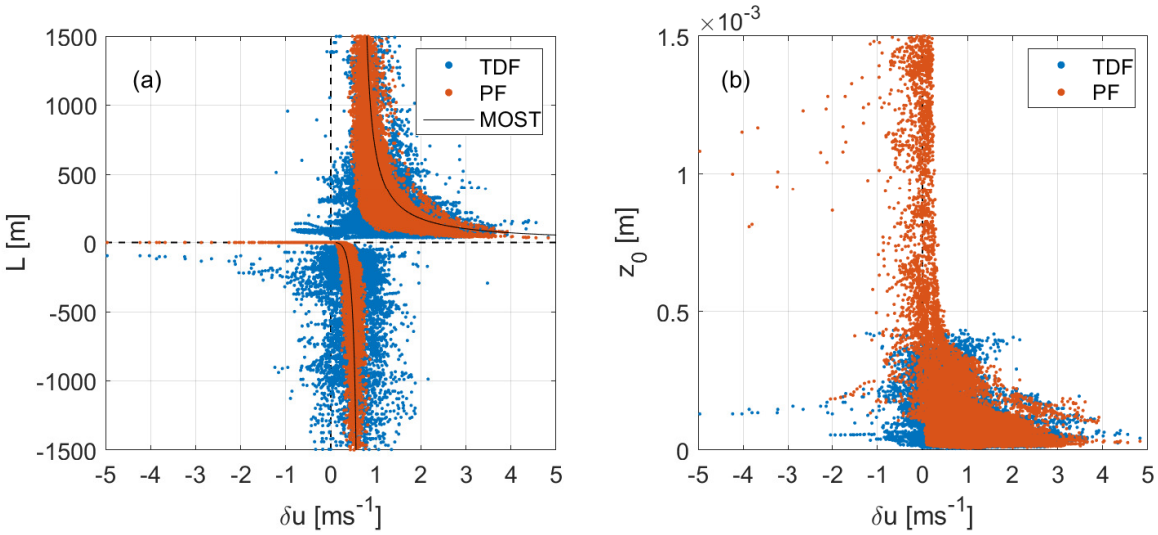

Figure 3.7: Relation between the predicted wind speed difference from measuring to hub height δu and (a) Obukhov length L and (b) roughness length z_0 of TDF and PF. The black line in (a) depicts the wind speed difference determined using the MOST depending on L for representative values of measuring height and roughness length.

impacts the forecast accuracy of the two methods in more detail. Figure 3.8 compares the forecast skill of the temperature difference-based forecast and the profile fit respectively. In both sub-figures it matches the stability classes derived by the TDF on the x-axis with the stability classes estimated for the PF on the y-axis. The panels positioned on the diagonal hence depict the identical stability class estimated by both approaches. The values within the panels in Figure 3.8(a) indicate the frequency of occurrence of each classification with respect to all cases analysed. Figure 3.8(a) visualises the profile fit's rmse skill score with the TDF rmse as the reference on a colour scale. The skill score of the bias' magnitude is shown in Figure 3.8(b), with the bias' sign of each of the two methods indicated within each panel (PF|TDF). In both sub-plots panels marked by blue writing indicate that the results are not statistically significant. Significance was determined by comparing 95 % confidence intervals of both data samples, as suggested by Cumming (2009). For most of the shown panels, indicated in green, the PF's rmse was reduced as compared to the TDF. The largest rmse skill score of 77 % was observed for situations defined as very stable by the TDF and as very unstable by the PF, visualized by the deep green panel in the lower right corner. In many of these situations, classified as very stable by the TDF, wind speeds were found to decrease or stay constant with height, and were thus categorised as very unstable profiles by the PF's fitting algorithm. Consequently, the substantial overestimation of wind speed and large rmse caused by the extrapolation using a very stable profile were reduced. Strongly positive skill scores were generally observed

for situations classified as stable or very stable by the TDF and those classified as very unstable by the PF due to the same reasons. As indicated by Figure 3.8(b) also the bias was in those situations improved by at least 62 %. In total, such cases were observed in 72 % of all analysed situations.

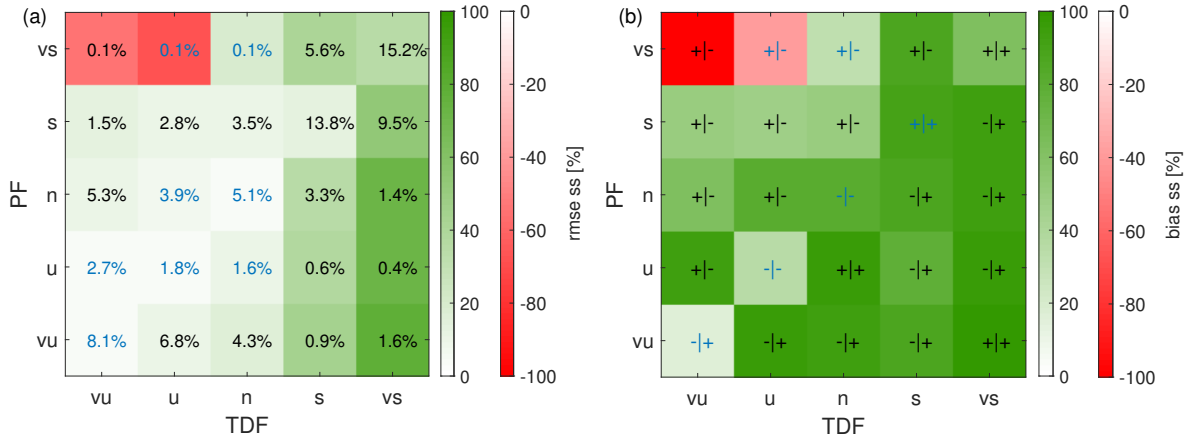

Figure 3.8: Comparison of 5-minute-ahead wind speed forecast skill of the TDF and the PF. In (a) TDF stability classes are shown on the x-axis, while PF ones are plotted on the y-axis. The values within the panels indicate the percentage of respective stability classifications with respect to all cases analysed. The colour-scale visualises the PF's skill score compared to the TDF in percent. Subfigure (b) shows the bias skill score, respectively. Here, the sign of the bias is indicated within the panel (PF|TDF). Blue values and signs indicate statistically insignificant results.

Several cases with comparably small skill scores, i. e. TDF and PF have almost the same result, indicated by light coloured panels near the main diagonal, can be observed. A number of these were determined not to be statistically significant. That means, for instance, due to a low number of forecasts within that category or only small differences between the scores of TDF and PF, it is ambiguous whether the profile fit leads to a reduction of forecasting errors. A reduction of the rmse and bias forecast skill was observed for situations classified as very unstable or unstable by the TDF and as very stable by the PF, visualized by the red panels in the upper left corner. They show a rmse skill score of -53 % and -68 %, respectively and a bias skill score of -156 % and -39 %, respectively. Both panels contain only a very small number of values and the scores of the latter can be considered insignificant.

Influence of height extrapolation on tendency-based forecast

The uncertainty analysis with the Monte Carlo simulations revealed the sensitivity of the TF to errors in the SCADA wind speeds and possible wind vector propagation and

lidar data processing, while the approach was more robust with respect to wind speed extrapolation uncertainties. In order to further improve the TF approach we assessed its quality dependent on extrapolation distance δz. Extrapolation distance is in this context defined as the difference of measuring height between the two consecutive wind speed forecasts used to determine the wind speed tendency, i. e. $\delta z = z_{\mathrm{m}}(t_i) - z_{\mathrm{m}}(t_{i-1})$. In Figure 3.9 rmse and bias dependent on δz are visualised, summarising the results of turbines T1-T4 and distinguishing between atmospheric stability. In stable cases, each bin contains 503 values, in unstable cases 574 values.

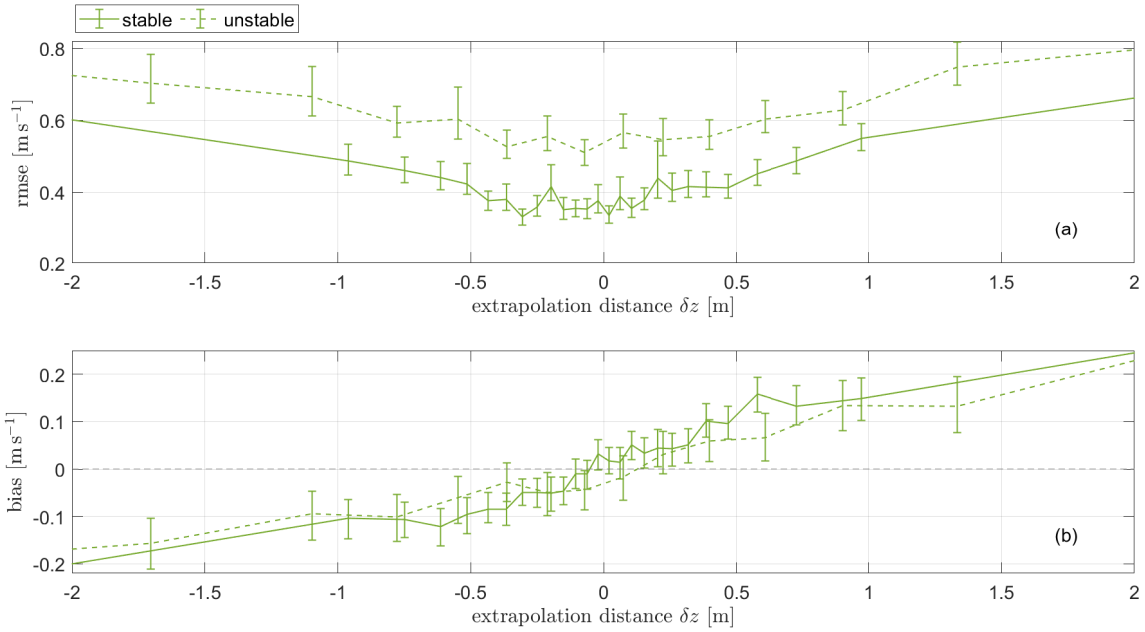

Figure 3.9: Forecast quality of the 5-minute ahead wind speed forecast dependent on extrapolation distance δz. The TF's (a) rmse and (b) bias, distinguishing between stable and unstable situations, are depicted. The 95 % confidence intervals are visualised as error bars. For stable cases each bin contains 503 values, for unstable cases 574 values.

The extrapolation distance δz is a consequence of the varying propagation distance of the contributing wind vectors to the lidar and the device's varying tilt. As expected, in Figure 3.9(a) forecast skill decreases for larger $|\delta z|$. As both the varying tilt and the varying distance of wind vectors to the lidar are related to wind speed changes, more larger extrapolation distances were observed during unstable cases. While in stable situations 90 % of all analysed values lay below $|\delta z| < 1$m, in unstable situations it was only 67 %. The tendency forecasts overestimated wind speed for positive δz and underestimated it during negative ones (Figure 3.9(b)).

Comparison of the three forecasting methods

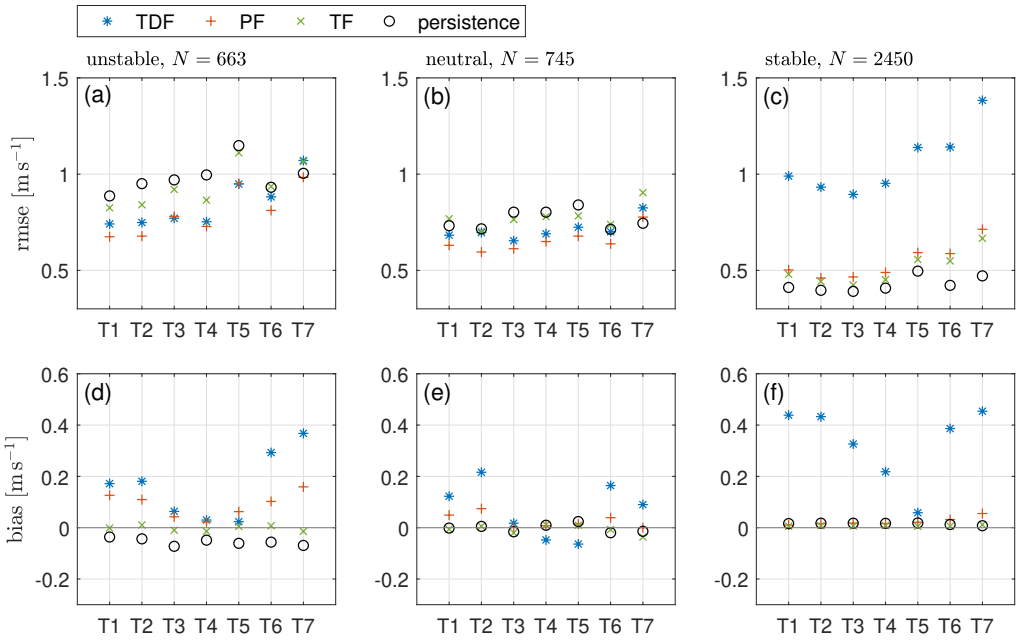

Figure 3.10: Forecast quality of the three lidar-based forecasts and persistence. The number of valid forecasts N, the rmse and bias of the different 5-minute ahead wind speed forecast for turbines T1-T7 and distinguishing between atmospheric stability are shown.

Figure 3.10 compares rmse and bias for the two new forecasting approaches, the previously introduced lidar-based forecast and persistence distinguishing between unstable (a, d), neutral (b, e) and stable (c, f) situations individually for the seven analysed turbines. Hereby, stable cases are defined as $0\,\mathrm{m} < L \leq 1000\,\mathrm{m}$, unstable cases as $-1000\,\mathrm{m} \leq L < 0\,\mathrm{m}$ and neutral ones as $|L| > 1000\,\mathrm{m}$. We only considered situations with simultaneously available forecasts for all turbines and approaches. Generally, forecasts are most accurate in stable situations, followed by neutral and unstable ones. Only exception are the distinct errors of the TDF observed during stable situations. Here, the bias indicates a strong overestimation of wind speed for all analysed turbines, except T5. Most accurate during stable situations is persistence, closely followed by the TF. PF, TF and persistence all show a bias close to zero. For unstable cases, the PF yields the lowest rmse, outperforming persistence for turbines T1-T6. The TDF and, in particular, the TF show a slightly larger rmse; however, they are also outperforming persistence for most cases. A positive bias, especially large for T6 and T7, can be observed for both the TDF and PF. Also in neutral situations, the PF can outperform all other approaches. The bias is close to zero for all four forecasts; only the TDF shows a distinct overestimation for T1, T2, T6 and

T7.

In the following, we analyse the forecast skill dependent on atmospheric conditions in more detail. To do so, we summarise the results of turbines T1-T4. We excluded turbines T5-T7 from this analysis due to their low forecast skill and availability. In all of the following figures (i. e. Figure 3.11-3.13), 95 % confidence intervals are visualised as error bars. Figure 3.11 depicts the dependency of rmse and bias on the Obukhov length L for all forecast methodologies. Each bin contains 716 values. Similar to Figure 3.10, all approaches are able to outperform persistence during unstable situations; however, not during stable ones. PF and TF beat the TDF during stable situations in terms of rmse, during unstable cases the TF can not outperform the TDF. The rmse values are generally lower for stable as compared to unstable cases except for the TDF. A large peak is visible for very stable cases with $0\,\mathrm{m} < L < 100\,\mathrm{m}$ with a rmse of up to $1.6\,\mathrm{m\,s^{-1}}$ and a bias of $1.3\,\mathrm{m\,s^{-1}}$. Approaching neutral situations, the TDF's bias shows a slight underestimation of wind speed. The bias of PF, TF and persistence fluctuates around zero for the entire range of L.

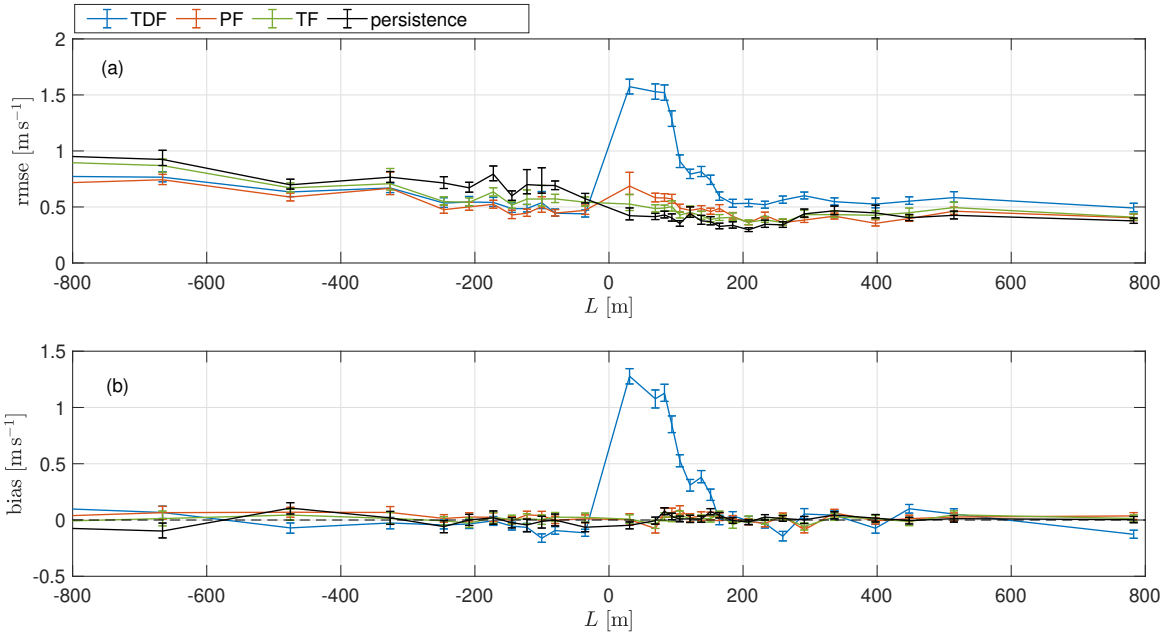

Figure 3.11: Forecast quality of the different 5-minute ahead wind speed forecasts dependent on Obukhov length L. In (a) the rmse and in (b) the bias are depicted. The 95 % confidence intervals are visualised as error bars. Each bin contains 716 values.

In Figure 3.12 the rmse dependent on the 5-minute wind speed increment from the forecast's initialisation time to the forecasted time for both stable and unstable cases is visualised. Each bin contains 503 values for stable and 574 values for unstable situations.

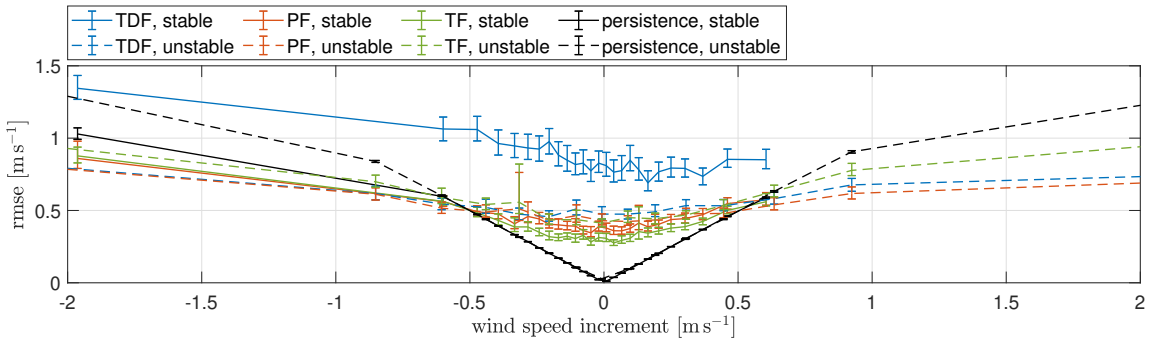

Figure 3.12: The rmse of the different 5-minute ahead wind speed forecasts dependent on 5-minute wind speed increments and distinguishing between stable and unstable situations. The 95 % confidence intervals are visualised as error bars. Stable cases contain 503 values per bin, unstable cases 574 values.

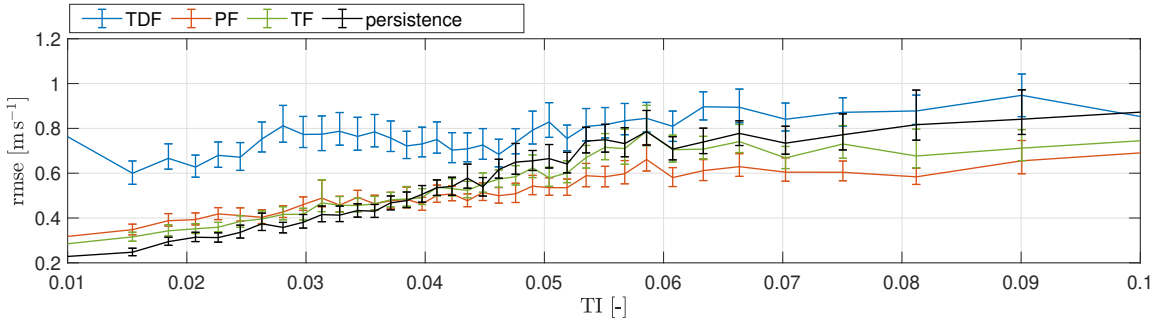

Figure 3.13: The rmse of the 5-minute ahead wind speed forecast dependent on the turbulence intensity TI. TI is computed from wind measurements observed up to 30 minutes prior to the forecast. The 95 % confidence intervals are visualised as error bars. Each bin contains 604 values.

Due to the definition of persistence, its rmse and bias are of the same magnitude as the increment itself. For the TDF the forecast skill is significantly lower for stable than for unstable cases as confirmed by previous results. Both the PF and the TF show lower rmse during stable stratification. For all three approaches, the rmse only slightly increases with increasing increment. The PF is hereby least sensitive to the magnitude of the wind speed increment. Consequently, the lidar-based forecasting methodologies are able to outperform persistence during changes in wind speed exceeding $0.5\,\mathrm{m\,s^{-1}}$ to $0.6\,\mathrm{m\,s^{-1}}$. During unstable stratification large wind speed increments can be most accurately forecasted by the PF, followed by the TDF and the TF. While during unstable stratification about 34 % to 41 % of all values show increments larger than the determined threshold of $0.5\,\mathrm{m\,s^{-1}}$ to $0.6\,\mathrm{m\,s^{-1}}$, this is the case only for 10 % to 16 % during stable stratification.

Figure 3.13 visualises the rmse dependent on the normalised standard deviation of SCADA wind speed, i. e. turbulence intensity TI, computed using wind measurements

observed up to 30 minutes prior to the forecast initialisation. Each bin contains 604 values. The rmse increases linearly with TI. Persistence shows the highest accuracy of all forecasts for $\mathrm{TI} < 0.04$. However, the increase of rmse, i. e. the slope of the depicted curves, is smaller for TDF, PF and TF, indicating that the accuracy of these approaches is less sensitive to turbulence intensity. While the TDF has a generally larger error than the other approaches, the PF and TF can outperform persistence for a turbulence intensity above 0.04. Such situations were observed in 58 % of all analysed situations. The confidence intervals suggest that this result can be considered statistically significant for the PF, however, not for the TF.

3.5 Discussion

Here, we will first discuss the uncertainties related to the two methods for wind speed profile estimation TDF and PF. Further, implications for minute-scale forecasting are evaluated and the value of the newly introduced approaches is discussed.

3.5.1 Accuracy of vertical wind speed profile estimation

Our analysis has revealed the impact of individual input parameters on the accuracy of stability estimation and consequently hub height wind speed. Temperature and wind speed measurement uncertainties have a strong influence on the accuracy of a stability parameter. Their effect on extrapolation accuracy is dominated by the influence of the stability correction term Ψ on the extrapolated wind speed. That means, as Ψ has such a large impact on u_{hh} in very stable situations, we expect larger uncertainties in wind speed extrapolation for those cases. This follows from the definition of the stability correction term and is true regardless of the exemplary uncertainties of the input parameters defined in Table 3.1. In a similar study, Saint-Drenan et al. (2009) found that already small uncertainties in temperature estimation result in considerable uncertainty in the shear estimation and consequently the extrapolated wind speed, particularly during very stable situations. For future applications, the installation of accurate temperature sensors is encouraged to enhance the stability estimation.

Kelly and Jørgensen (2017) discovered that the impact of misestimations of z_0 on wind resource estimation is minimal for small z_0. For offshore situations with typical values in the order of $z_0 = 10^{-4}\,\mathrm{m}$, the estimated hub height wind speed is thus expected not to be influenced significantly by misestimations of roughness. Conclusively, determining z_0 by means of measured wind speed and L is considered a fair method for offshore wind speed forecasting.

Even though the uncertainty in measurement height estimation is small compared to that of stability and wind speed, especially in stable situations, it can considerably impact the wind speed extrapolation accuracy. With increasing range gate, the lidar devices inclination will cause increasingly large deviations in the measuring height. Thus, especially for long-range lidar measurements, as used for minute-scale forecasting, the lidar alignment is of large importance (Theuer et al., 2020a). Schneemann et al. (2021) conducted a detailed uncertainty assessment of long-range lidar measurements and made recommendations for their offshore operation.

In addition to uncertainties of input parameters, one needs to consider that the stability-corrected logarithmic wind profile is not always a good representation of the true wind profile (Kalverla et al., 2017). It is not possible to represent, for instance, kinks or reversed profiles. Especially during stable conditions, such profiles can be observed frequently (Møller et al., 2020). During such conditions, when wind speeds are described as strongly increasing by logarithmic profiles, the deviations between extrapolated and true profiles are considerable (Theuer et al., 2020a; Møller et al., 2020). Further, also the model describing the relation between the bulk Richardson number and the Obukhov length L (Grachev and Fairall, 1997) is subject to some inherent uncertainty that was not included in our analysis. Moreover, the assumptions based on the Monin-Obukhov similarity theory (MOST) are only valid in the surface layer. For larger altitudes the wind speed profile is increasingly affected by other parameters such as the boundary-layer depth (Peña et al., 2008). This might pose a problem in particular during very stable situations, when the surface layer is very shallow, thus possibly below the height of interest for large offshore wind turbines. However, also during neutral and unstable situations the atmospheric boundary layer height might have a non-negligible influence on the wind speed profile at hub height. In good agreement with the strongly positive bias of the TDF observed in this work (Section 3.4.3), several studies (Peña et al., 2008; Optis et al., 2014) have shown the logarithmic profiles tendency to overestimate wind speeds in high altitudes and during stable conditions. An analysis of another data set from this campaign by Theuer et al. (2020a) indicates that such situations start to occur with target heights of 61 m and extrapolation distances δz larger than 25 m and can thus be expected to impact wind speed extrapolation to the hub height of 92 m considered in this case. Future investigations could assess whether the use of a wind speed extrapolation method that takes into consideration the boundary layer depth and is valid beyond the surface layer (Peña et al., 2008; Gryning et al., 2007; Optis et al., 2021) could improve wind speed extrapolation and the forecast skill of the TDF.

Taking into account the results of our study, a better alternative to wind speed extrap-

olation with the logarithmic profile is needed. Most beneficial for that purpose would be high-frequency wind profile measurements, e. g. lidar wind profiler measurements. However, in most cases such data is not available and one is restricted to the use of on-site meteorological measurements. As an alternative, the profile fit approach utilises wind turbine operational data, which allows to better describe the wind shear from measuring to hub height. Particularly interesting are situations classified as very unstable and with comparably large fitted value of z_0. In these cases, L is restricted by the decreasing wind speed with height. That means the main parameter to adjust the wind speed is the roughness length z_0. On average, it was observed that z_0 increases by a factor of 4.5 compared to the originally calculated values. This factor is defined by the original value of L and the wind speed difference at hub height. It should be noted that the parameters determined by the profile fit cannot be understood as an accurate description of the atmospheric stability and roughness length, respectively, but rather describe the observed wind shear empirically.

3.5.2 Relevance for minute-scale forecasting

The profile fit-based forecast has benefits, particularly during stable stratification. The additional consideration of SCADA wind speed and the fitting approach allow to adjust for systematic errors in propagated wind vectors, for instance, caused by measurement height misestimation or errors in LOS wind speed measurements. This was confirmed by the results of the Monte Carlo simulations. Nevertheless, uncertainties are introduced whenever profiles change during the forecast horizon, most likely during dusk and dawn, or when only few data is available during the respective time period. Also the advection of wind vectors is expected to introduce uncertainties, influencing the accuracy of the fit. In such cases, it might be more accurate to rely on the TDF stability values. Generally, we expect that the PF would benefit from more detailed profile information, i. e. wind speed measurements at additional heights. Another advantage of the profile fit is its independence of meteorological measurements.

The tendency-based forecast avoids vertical profile extrapolation by considering two observed consecutive profiles. Also the consideration of recent SCADA data has a significant impact on the forecast's accuracy. Here, less weight is put onto the propagated lidar measurements and additionally wind speed measurements at hub height are considered. Persistence shows that in many cases the last observation of wind speed can provide accurate estimates of the next observation, especially during stable atmospheric conditions. Further, the Monte Carlo simulations revealed that wind vector estimation and propagation errors have less impact as not their absolute value, but only their ten-

dency is considered in the TF. Our analysis has further shown the TF's dependency on the extrapolation distance. This is on one hand related to the wind speed increments associated to larger extrapolation distances, but might on the other hand also be caused by increasing uncertainties in height extrapolation (Theuer et al., 2020a). As extrapolation distances can be significantly reduced when eliminating the lidar's tilt, this emphasises the need for a proper alignment of the device. Alternatively, a bias correction might be able to improve the TF's accuracy.

As expected, the benchmark persistence is much more skilful during stable compared to unstable situations. Also the two newly introduced lidar-based approaches show lower errors during stable situations. This is in good agreement with the assumption that the applied advection techniques are more accurate during stable cases. Here, the evolution of larger structures dominates the flow compared to small scale buoyancy effects. Würth et al. (2018) found that small wind speed fluctuations do not persist when propagated across larger distances and thus the prediction of flow over complex terrain is challenging. Further, we expect that turbines positioned within the wind farm cannot be predicted well using Lagrangian advection. A more detailed analysis of different propagation techniques is therefore essential.

For future applications, it is important to be able to estimate the accuracy of each approach during different situations. We have identified the variability of the wind, expressed in terms of atmospheric stability or turbulence intensity as a major influencing factor. The lidar-based forecasts, in particular the PF, were found to be less sensitive to these parameters compared to persistence. This is also true for the dependency of forecast accuracy on the magnitude of the wind speed increment. While this is advantageous for wind speed changes larger than approximately $0.5\,\mathrm{m\,s^{-1}}$, it also means that it is virtually impossible to outperform persistence in situations where wind speeds are almost constant. However, these findings suggest that lidar-based methodologies can be especially beneficial during wind ramps. This is confirmed by a recent study of Valldecabres et al. (2020), who forecasted the power of individual and aggregated wind turbines using dual Doppler radar data with an emphasis on the prediction of ramp events. Such situations are especially important for grid stability and electricity trading and typically not represented well by statistical models (Pichault et al., 2021b). Further, one could argue that the lidar-based forecast will become more accurate than persistence with increasing lead time, as this would result in a higher amount of large wind speed increments. Würth et al. (2018), for instance, found that the accuracy of lidar-based forecasts compared to persistence improves when considering larger lead times.

Also, Würth et al. (2019) suggest that the advantages of minute-ahead forecasts com-

pared to persistence increase with forecast horizon. We could not prove this hypothesis as the measurement set-up restricted us to 5-minute ahead forecasts (Theuer et al., 2020b). In future analysis, the accuracy of wind power forecasts based on the introduced methods needs to be evaluated. As the two newly introduced methods are directly based on the SCADA wind speed, a careful calibration of the power curve used to translate wind speed to power is necessary for each of the analysed turbines. Also the non-linearity of the power curve will impact the forecast skill (Theuer et al., 2020b).

3.6 Conclusions

We developed two new lidar-based forecasting methodologies in this work, and evaluated them against an existing approach and persistence under varying atmospheric conditions at an offshore wind farm, aiming to reduce the associated errors. The two new approaches additionally utilise wind turbine operational data to improve wind speed extrapolation to hub height. We also assessed the methods uncertainty under varying atmospheric conditions using an analytical uncertainty estimation of wind speed extrapolation by means of a stability-corrected logarithmic wind profile and using Monte Carlo simulations, to also capture uncertainties related to the lidar data processing and wind vector propagation.

Our results revealed the high potential of the profile fit-based approach and the tendency-based approach compared to the previously introduced temperature difference-based approach, particularly during stable atmospheric conditions. These two new approaches could outperform persistence during unstable and neutral stratification for situations with turbulence intensity greater than 4 % and wind speed increments larger than $0.5\,\mathrm{m\,s^{-1}}$ to $0.6\,\mathrm{m\,s^{-1}}$.

Monte Carlo simulations highlighted their lower sensitivity to inaccurate input parameters, for instance wind speed and stability estimates. An analytical uncertainty estimation of the height extrapolation by means of a stability-corrected logarithmic profile confirmed the temperature difference-based approach's high uncertainty during very stable conditions due to large uncertainties in the stability correction term. Despite the much lower errors of the profile fit-based approach and tendency-based approach compared to the temperature difference-based approach these two new methods could not outperform persistence during stable stratification.

An accurate alignment of the lidar device could further improve the two new approaches. Wind speed measurements at additional heights, e.g. with a profiling lidar, would be beneficial especially for the profile fit-based approach.

We conclude that the additional use of wind turbine operational data has a significant

positive impact on the forecast accuracy of lidar-based forecasts. This is especially of interest when no wind profile measurements or meteorological measurements are available. Generally, lidar-based forecasts were found to be less sensitive to atmospheric conditions than persistence. The characterisation of the approaches' forecast skill under different atmospheric conditions can be valuable for decision-making processes.

Chapter 4

Observer-based power forecast of individual and aggregated offshore wind turbines[c]

Due to the increasing share of wind energy in the power system, minute-scale wind power forecasts have gained importance. Remote sensing-based approaches have proven to be a promising alternative to statistical methods and thus need to be further developed towards an operational use, aiming to increase their forecast availability and skill. Therefore, the contribution of this paper is to extend lidar-based forecasts to a methodology for observer-based probabilistic power forecasts of individual wind turbines and aggregated wind farm power. To do so, lidar-based forecasts are combined with SCADA-based forecasts that advect wind vectors derived from wind turbine operational data. After a calibration, forecasts of individual turbines are aggregated to a probabilistic power forecast of turbine subsets by means of a copula approach. We found that combining the lidar- and supervisory control and data acquisition (SCADA)-based forecasts significantly improved both forecast skill and forecast availability of a 5 min ahead probabilistic power forecast at an offshore wind farm. Calibration further increased the forecast skill. Calibrated observer-based forecasts outperformed the benchmark persistence for unstable atmospheric conditions. The aggregation of probabilistic forecasts of turbine subsets revealed the potential of the copula approach. We discuss the skill, robustness and dependency on atmospheric

[c]The content of this chapter is identical to the journal article submitted to Wind Energy Science: Theuer, F., Rott, A., Schneemann, J., von Bremen, L., and Kühn, M.: Observer-based power forecast of individual and aggregated offshore wind turbines, *Wind Energy Science*, 7, 2099-2116, https://doi.org/10.5194/wes-7-2099-2022, 2022.

conditions of the individual forecasts, the value of the observer-based forecast, its calibration and aggregation, and more generally the value of minute-scale power forecasts of offshore wind. In conclusion, combining different data sources to an observer-based forecast is beneficial in all regarded cases. For an operational use one should distinguish between and adapt to atmospheric stability.

4.1 Introduction

With the increasing share of wind and solar power in our energy system, the need for accurate minute-scale power forecasts to support grid stability and electricity trading arises (Dowell and Pinson, 2016; Sweeney et al., 2019; Würth et al., 2019). The low geographical dispersion of installed offshore wind capacity and its consequently high volatility (Malvaldi et al., 2017) calls for skilful forecasts of, in particular, offshore wind power. Commonly, statistical methods, such as the benchmark persistence or AR(I)MA (auto-regressive (integrated) moving average) methods, are applied on those timescales (Würth et al., 2019). While those methods are reliable in many situations, they underperform, for instance, during ramp events, i.e. sudden and strong changes in wind speed or direction. Therefore, recently remote-sensing-based wind speed and power forecasts have been researched as a physical-based alternative (Würth et al., 2018; Valldecabres et al., 2018b,a, 2020; Theuer et al., 2020b, 2021; Pichault et al., 2021a).

Several studies have shown the potential of lidar-based wind speed and power forecasts to outperform the benchmark persistence under specific atmospheric conditions (Valldecabres et al., 2018b; Theuer et al., 2021; Pichault et al., 2021a). Theuer et al. (2020b) and Valldecabres et al. (2018b) found that atmospheric stability can influence forecast accuracy in particular with respect to the wind speed height extrapolation. Theuer et al. (2021) showed that overall lidar-based forecasts are more accurate during stable conditions; however, they can only outperform persistence during unstable stratification because persistence is also more skilful during stable situations. Valldecabres et al. (2020) introduced a dual-Doppler radar-based forecast that was able to outperform persistence in terms of probabilistic scores during ramp events and for free-stream turbines. Two lidar-based methods, one based on a neural network and one on a smart persistence approach, introduced by Pichault et al. (2021a) were able to exceed persistence, as well as an ARIMA method during ramp events and non-ramp situations, for different wind directions and atmospheric conditions onshore. In their work the authors focus on deterministic forecasts and wind farm power forecasts that do not distinguish forecasts at turbine level.

Driven by these promising results, the methods' development now needs to be directed towards an operational use. Besides the fact that there are many situations during which persistence outperforms the lidar-based forecast, low forecast availability is a main issue with the technology and concepts available so far. Hence, depending on the wind farm layout, scanning trajectories, lidar availability and wind conditions, no or only low-quality forecasts can be generated (Theuer et al., 2020b). This problem can be reduced by optimizing scanning trajectories, increasing the lidar's measurement range and possibly commissioning additional devices. However, during situations with reduced lidar sight, due to, for example, fog or rain or when devices fail, one would need to fall back to an alternative data source. For that purpose, hybrid methods are worth being considered. In the context of lidar-based methods, Theuer et al. (2021), for instance, showed that the additional use of wind turbine operational data can contribute to the forecast accuracy. Also Pichault et al. (2021a) included wind farm operational data in the form of a smart persistence approach in their forecast and achieved promising results.

Currently, lidar-based methods have been evaluated with regard to their probabilistic characteristics in a few cases only (Theuer et al., 2020b) but mainly with respect to their deterministic characteristics and for individual wind turbines (Würth et al., 2018; Valldecabres et al., 2018b; Theuer et al., 2021). However, for end-users in power trading and system operation, uncertainty information is of high value as it aids decision-making processes (Dowell and Pinson, 2016; Sweeney et al., 2019). One way to increase the reliability and sharpness of probabilistic forecasts is statistical post-processing, i.e. forecast calibration (Thorarinsdottir and Gneiting, 2010). Commonly, ensemble model output statistics (EMOS) is used. EMOS was first developed for temperature and pressure forecasts (Gneiting et al., 2005) but has successfully been applied to the prediction of precipitation (Scheuerer, 2014), wind speed (Thorarinsdottir and Gneiting, 2010), wind vectors (Schuhen et al., 2012) and power (Späth et al., 2015).

Considering the different areas of application of minute-scale forecasts, both individual turbines' power output and aggregated wind farm power or power at the grid connection point, i.e. aggregated power of a subset of individual wind turbines, are important. While the former are mainly required for wind turbine control (Würth et al., 2019), the latter are of interest for trading and system operation purposes. So far, lidar-based forecasts of individual wind turbines focused on free-stream situations. In a next step, these methodologies need to be extended to wake-influenced turbines. A main challenge is hereby the propagation technique, which assumes constant wind vector trajectories and is therefore unable to account for wakes. Valldecabres et al. (2020) circumvent this by applying a directional turbine efficiency that significantly improved the skill of their

radar-based forecast.

Individual turbines' power forecasts can also be helpful when determining wind farm power. In this context, recently hierarchical forecasting on both temporal and spatial levels has gained attention, aiming to achieve coherency between different levels of the hierarchy and thereby improving forecast performance at each level (Bessa, 2016; Gilbert et al., 2020). A common method in the context of coherent probabilistic forecasts is copula approaches. Gilbert et al. (2020) successfully implemented and tested a variety of copulas to aggregate the probabilistic power forecasts of individual wind turbines to the probabilistic forecast of wind farm power.

Our objective in this paper is to develop a probabilistic observer-based forecast of aggregated wind farm power. To do so, we first introduce an observer-based power forecast of individual wind turbines that combines lidar and turbine operational data. This method accounts for variable wake conditions and increases forecast availability and skill. Additional calibration further improves the forecast's probabilistic characteristics. In the second step, we aggregate individual probabilistic wind turbine power forecasts to probabilistic wind farm power forecasts by applying a copula approach.

4.2 Methods

The basis of this work is the lidar-based forecasting approach introduced and analysed in more detail in Theuer et al. (2020a), Theuer et al. (2020b) and Theuer et al. (2021). The method is briefly described in Sect. 4.2.1. In this work this approach is significantly extended further as described in the following: Using SCADA (supervisory control and data acquisition) data, it is first extended to an observer-based forecast (OF) to increase forecast availability and skill (see Sect. 4.2.2). In a next step, observer-based forecasts are calibrated by means of ensemble model output statistics (EMOS) (see Sect. 4.2.3). Finally, probabilistic power forecasts of individual wind turbines are aggregated using different copula approaches (see Sect. 4.2.4).

4.2.1 Reference method lidar-based forecast (LF)

The reference method probabilistic lidar-based power forecast (LF) using single lidar measurements was developed by Theuer et al. (2020b) and is based on the work of Valldecabres et al. (2018a) who applied dual-Doppler radar. Lidar-based power forecasts utilize horizontal or slightly elevated plan position indicator (PPI) lidar scans measuring the inflow of an offshore wind farm. Typically, lidar devices are positioned on the transition piece (TP) of a wind turbine or alternatively a nearby platform and record line-of-sight (LOS)

wind speed measurements and the carrier-to-noise ratio (CNR) at each scanned azimuth angle and range gate along with a time stamp. Using that information, lidar scans are filtered applying a data density approach on normalized CNR values and LOS wind speed measurements similar to Beck and Kühn (2017). By means of a velocity azimuth display (VAD)-like fit, the wind direction χ is then determined dependent on range gate r (Werner, 2005) and used to reconstruct a wind field with the horizontal wind speed u_h from the line-of-sight wind speed measurements u_LOS and the lidar's azimuth angle ϑ

$$u_\mathrm{h}(r,\vartheta) = \frac{u_\mathrm{LOS}(r,\vartheta)}{\cos(\vartheta - \chi(r))}. \tag{4.1}$$

After wind field reconstruction, the individual lidar scans are interpolated to a Cartesian grid and synchronized in time (Beck and Kühn, 2019). Time synchronization refers to the propagation of individual parts of the lidar scans measured at different times to the same time step using semi-Lagrangian advection. It aims at accounting for the large time shift within each scan. A Lagrangian advection technique is then applied to propagate wind vectors, i.e. horizontal wind speed and wind direction information at each grid point. Hereby, it is assumed that vectors travel with their local wind speed and wind direction and do not change their trajectory while travelling. Wind vectors reaching the area of influence around the target turbine within a time interval of $k \pm 30\,\mathrm{s}$ with lead time k are selected to contribute to the target turbine's probabilistic forecast. For each forecasted time step, wind data recorded during a time interval previous to forecast initialization are taken into account. That means that for each forecast several time-synchronized scans are considered, and the travelling time of wind vectors can therefore exceed the lead time. Considering also previous scans is important to be able to forecast turbines positioned further away from the lidar-scanned area. Wind speed forecasts at measurement height u_m are transformed to hub height assuming a logarithmic stability-corrected wind speed profile (Emeis, 2018). Here, we apply a methodology introduced as tendency-based forecast in previous work (Theuer et al., 2021). It determines the wind speed tendency at measuring height and applies it to wind speed at hub height u_hh after performing a correction of measuring height z_m and atmospheric conditions defined by the Obukhov length L and the roughness length z_0 between time steps t_i and t_{i-1} (see Eq. 4.2). $\Psi(z, L)$ describes the stability correction term (Emeis, 2018). Measuring heights vary along the range gate due to the curvature of the Earth and dynamically due to a thrust-dependent tilt of the lidar device (Rott et al., 2022). The hub height wind speed

at the future time step t_i is then defined as

$$u_{\mathrm{hh}}(t_i) = \frac{\ln\left(\frac{z_{\mathrm{m}}(t_{i-1})}{z_0(t_i)}\right) - \Psi\left(\frac{z_{\mathrm{m}}(t_{i-1})}{L(t_i)}\right)}{\ln\left(\frac{z_{\mathrm{m}}(t_i)}{z_0(t_i)}\right) - \Psi\left(\frac{z_{\mathrm{m}}(t_i)}{L(t_i)}\right)} \frac{u_{\mathrm{m}}(t_i)}{u_{\mathrm{m}}(t_{i-1})}\, u_{\mathrm{hh}}(t_{i-1}). \tag{4.2}$$

In a final step, the wind speed forecast is transformed to a power forecast using power curves extracted individually for each wind turbine from 1 min mean SCADA wind speed and power data. In this case, the wind speed values are not measured but estimated from power, pitch angle and the SCADA system's turbine power curve.

Details on this forecasting methodology can be found in Theuer et al. (2020b, 2021).

4.2.2 Extension to an observer-based forecast (OF) by integrating a SCADA-based forecast (SF)

If the LF is invalid due to missing data, the prevailing wind conditions, the lidar trajectory or wind farm layout, one needs to fall back to an alternative forecasting approach. For that purpose we introduce the observer-based forecast, which combines the LF and a SCADA-based forecasting approach.

The SCADA-based power forecast (SF) modifies the methodology introduced in Rott et al. (2020), adapting its wind vector weighting approach and time scales to match the LF. The 1 Hz wind speed and wind direction data of all wind turbines of the wind farm are propagated using Lagrangian advection. In accordance with the LF, only wind vectors v arriving within a certain area of influence around our target turbine j are selected. The selected vectors originating at time $t_{v,j}$ are then weighted according to their age $t - t_{v,j}$ using an inverse temporal distance weighting to determine the weighting factor $\hat{w}_{v,j}(t)$:

$$\hat{w}_{v,j}(t) = \frac{w_{v,j}(t)}{\sum_v w_{v,j}(t)}, \tag{4.3}$$

with

$$w_{v,j}(t) = \frac{1}{(t - t_{v,j})^p} \tag{4.4}$$

and the tuning parameter $p \in \mathbb{N}$ that determines the strength of the weighting factor's decrease with increasing temporal distance Rott et al. (2020). The selected wind vectors are resampled to a predefined number of wind vectors with their individual contribution given by the weighting factor. As suggested by Rott et al. (2020) a bias correction with the observed wind speed $u_{\mathrm{obs},j}$ and the ensemble average of the forecast at turbine j, i.e. $\bar{u}_{\mathrm{sc},j}$, is applied to all members v of the forecast at this turbine $u_{\mathrm{sc},v,j}$ to account

for possible systematic errors and wake effects. The bias-corrected wind speed vectors $u_{\mathrm{corr},v,j}$ then yield

$$u_{\mathrm{corr},v,j}(t) = u_{\mathrm{sc},v,j}(t) - \left(\frac{1}{N_\mathrm{t}} \sum_{l=0}^{N_\mathrm{t}} \bar{u}_{\mathrm{sc},j}(t-k-l\,\Delta\tau) - u_{\mathrm{obs},j}(t-k-l\,\Delta\tau) \right), \tag{4.5}$$

with N_t the number of time steps with length $\Delta\tau$ prior to forecast initialization $t-k$, with lead time k, considered to determine the bias. Wind speed forecasts are transformed to power forecasts as described for the LF (Sect. 4.2.1).

In this work we extend the LF to an observer-based power forecast (OF) by integrating the SF. If both LF and SF are valid, they are weighted equally in the OF; otherwise only the valid forecast is considered. To be considered valid we require a minimum number of wind vectors to reach the target turbine for both methods. In that way, we avoid individual wind vector outliers being given too much weight. To account for the varying number of wind vectors contributing as a consequence of different temporal and spatial resolutions of the lidar and SCADA data, we resample each forecast to contain the same predefined number of members.

4.2.3 Calibration of the observer-based forecast

In a next step, the OF is calibrated using ensemble model output statistics (EMOS). EMOS is commonly used to calibrate ensemble forecasts; in our work it is applied to minute-scale remote sensing-based power forecasts for the first time. Hereby, a truncated Gaussian distribution

$$f(x,\mu,\sigma) = \frac{1}{\sigma} \frac{\phi\left(\frac{x-\mu}{\sigma}\right)}{\Phi\left(\frac{P_\mathrm{r}-\mu}{\sigma}\right) - \Phi\left(\frac{0-\mu}{\sigma}\right)}, \tag{4.6}$$

for $0 \leq x \leq P_\mathrm{r}$ and $f(x<0)=0$ and $f(x>P_\mathrm{r})=0$ with rated power P_r is used to model the wind speed distribution (Thorarinsdottir and Gneiting, 2010). The probability density function of the standard normal distribution is defined by ϕ and its cumulative distribution function (cdf) by Φ. The mean $\mu_{i,j}$

$$\mu_{i,j} = a + b\,\overline{\mathrm{fc}}_{i,j}, \tag{4.7}$$

and the variance $\sigma^2_{i,j}$ of the distribution

$$\sigma^2_{i,j} = c + d\,\mathrm{fc}_{\sigma^2 i,j}, \tag{4.8}$$

are modelled as a linear function of the ensemble mean $\overline{\mathrm{fc}}_{i,j}$ and variance $\mathrm{fc}_{\sigma^2\,i,j}$ respectively with time index i and turbine index j as suggested by Thorarinsdottir and Gneiting (2010). The cdf of the ensemble members at time i and for turbine j is defined as $F_{i,j}(\mu_{i,j}(a,b),\sigma_{i,j}(c,d))$ and referred to as $F_{i,j}$ in the following. The parameters a, b, c and d are optimized to minimize the cost function,

$$J_j(x_{i,j},a,b,c,d) = \frac{1}{N_\mathrm{c}}\sum_{i=1}^{N_\mathrm{c}} \mathrm{crps}(F_{i,j},x_{i,j}), \tag{4.9}$$

based on the continuous ranked probability score (crps) of the forecast,

$$\mathrm{crps}(F_{i,j},x_{i,j}) = \int_0^{P_\mathrm{r}} [F_{i,j}(x) - H(x-x_{i,j})]^2 dx, \tag{4.10}$$

with the observation $x_{i,j}$, the number of time steps considered N_c and the Heaviside step function H (Gneiting et al., 2007). A sliding window approach is applied; thus a training interval with optimized length before forecast initialization is used to calibrate the forecast.

4.2.4 Aggregated wind turbine power forecast using a copula approach

The observer-based forecast provides probabilistic power forecasts of individual wind turbines, i.e. one cdf $F_{i,j}$ for each time index i and individual wind turbine j. Here, we aim to derive a joint predictive distribution of wind power production from a subset of wind turbines in a wind farm using a copula approach following the work of Gilbert et al. (2020) and Bessa (2016). In our work we apply the method to a data set with higher temporal resolution and shorter forecast horizon. This approach is based on Sklar's theorem, which states that a m-dimensional cumulative distribution F, with the number of turbines m and the length of the training data set t_n, can be expressed using a copula function C of the individual marginal distributions $F_{i,j}$ as

$$F\left(x_{1,1},x_{1,2},...,x_{t_\mathrm{n},m}\right) = C\left(F_{1,1}\left(x_{1,1}\right),F_{1,2}\left(x_{1,2}\right),...,F_{t_\mathrm{n},m}\left(x_{t_\mathrm{n},m}\right)\right), \tag{4.11}$$

conditional on well-calibrated forecasts with uniformly distributed marginals $u_j = F_j\left(x_j\right)$ (Gilbert et al., 2020). In this work, we apply a Gaussian copula,

$$\begin{aligned} &C\left(F_{1,1}\left(x_{1,1}\right),F_{1,2}\left(x_{1,2}\right),...,F_{t_\mathrm{n},m}\left(x_{t_\mathrm{n},m}\right)\right) = \\ &\Phi_\Sigma\left(\Phi^{-1}\left(F_{1,1}\left(x_{1,1}\right)\right),\Phi^{-1}\left(F_{1,2}\left(x_{1,2}\right)\right),...,\Phi^{-1}\left(F_{t_\mathrm{n},m}\left(x_{t_\mathrm{n},m}\right)\right)\right) \end{aligned} \tag{4.12}$$

with the m-dimensional normal distribution Φ_Σ with covariance matrix Σ and a mean of $\mu_1 = \mu_2 = ... = \mu_m = 0$. To determine the joint predictive distribution of the individual turbines and finally the probabilistic aggregated power, we proceed as follows. First, marginal distributions of all wind turbines to be considered for the aggregation are determined from the cdfs and observations as $F_{i,j}(x_{i,j})$, and their uniformity is verified (Pinson et al., 2009). Marginals are then transformed into the Gaussian domain described by $\Phi^{-1}(F_{i,j}(x_{i,j}))$. Based on these transformed and normally distributed marginals, the covariance matrix Σ of the training data set can be determined. This multivariate distribution can be used to generate M random samples, which are then transformed back to the uniform domain. Finally, for each turbine j and time steps within the test data set i, the samples are transformed into the power domain using its cdf $F_{i,j}$ and summed over all turbines to yield a set of aggregated power samples. Based on these M aggregated power samples, a power distribution, i.e. a probabilistic forecast, can be derived.
To enlarge the test data set, we estimate covariance matrices using a sliding windows approach. This also allows us to determine a joint predictive distribution that flexibly adapts to changing atmospheric conditions. A change in wind direction, for example, will affect the wake situation of the turbines and is consequently expected to have an impact on the turbine subset's joint distribution too.

In addition to the empirical covariance determined as described above, we define and test parametric covariance matrices based on an exponential relation,

$$\Sigma_{j,h} = \exp\left(-\frac{\Delta r_{j,h}}{\nu}\right), \tag{4.13}$$

with the covariance between two turbines $\Sigma_{j,h}$ and the spatial distance Δr between the position of turbines j and h (Gilbert et al., 2020). The parameter ν is fitted using a least-squares regression and the empirically determined covariance matrix. The advantage of parametric copulas is their lower sensitivity to reduced data availability, avoiding noisy covariances and overfitting (Gilbert et al., 2020).
We further evaluate vine copulas as a more flexible option compared to Gaussian copulas. Vine copulas describe a set of bivariate copulas with variable distribution families for each (turbine) pair (Bessa, 2016). Here, we determined vine copulas using the MATLAB framework developed by Coblenz (2021). Distribution families are chosen using the Akaike information criteria (AIC) (Aas et al., 2009).

4.3 Results

After the general description of the methodological steps in the previous section, we introduce the case study analysed in this work and its case-specific parameters in Sect. 4.3.1. In Sect. 4.3.2 the results of the LF and SF for individual wind turbines are presented. Further, we assess the value of the OF compared to the LF, SF and persistence (Sect. 4.3.3) and evaluate the calibrated OF compared to the raw, i.e. the uncalibrated, one (Sect. 4.3.4). Finally, we determine the forecast skill of the aggregated probabilistic power of several wind turbines and compare it against a probabilistic version of persistence (Sect. 4.3.5).

4.3.1 Case study at the offshore wind farm Global Tech I (GT I)

The methodology described in the previous sections is applied to and evaluated at the offshore wind farm Global Tech I (GT I) in the German North Sea. The wind farm consists of 80 turbines of type Adwen AD 5-116, with a hub height of $z_{\mathrm{hh}} = 92\,\mathrm{m}$, a rotor diameter of $D = 116\,\mathrm{m}$ and a rated power of $P_{\mathrm{r}} = 5\,\mathrm{MW}$. The lidar was placed on the transition piece of turbine GT58 at a height of $z_{\mathrm{TP}} = 24.6\,\mathrm{m}$. Horizontal plan position indicator (PPI) lidar scans were performed with a WindCube 200S (serial no. WLS200S-024) and with an elevation of 0°, an azimuth angle spanning 150°, an azimuthal resolution of 2°, range gates from 500 to 7950 m in 35 m intervals and an accumulation time of 2 s. Including the measurement reset time, the scanning duration was 156 s. The scanning trajectories, which were adjusted manually according to four wind direction sectors, and the wind farm layout are depicted in Fig. 4.1b. Figure 5.1a additionally depicts the layout of the wind farms Albatros and Hohe See, which were under construction but not yet operational during the time of the analysis. Those turbines did not cause any wakes but were visible as hard targets in the lidar scans occasionally, which were omitted during data filtering and thus did not impact the forecast. More details on the measurement campaign are available in Schneemann et al. (2020) and Theuer et al. (2020b, 2021).

Each forecasted time step of the LF considered the six most recent scans and thus can contain wind data measured during the last 15 min. This ensures that also turbines positioned far away from the lidar scans can be reached by low wind speeds and their forecasts will not be biased. Wind vectors contributing to the SF were weighted using a tuning parameter of $p = 4$. The choice of this parameter is further discussed in Sect. 4.4.1. The SF's bias correction was performed considering a number of $N_{\mathrm{t}} = 5$ time steps prior to forecast initialization. This ensures that there is enough data for bias estimation while keeping the correlation high. The step length was chosen as $\Delta\tau = 156\,\mathrm{s}$ in accordance

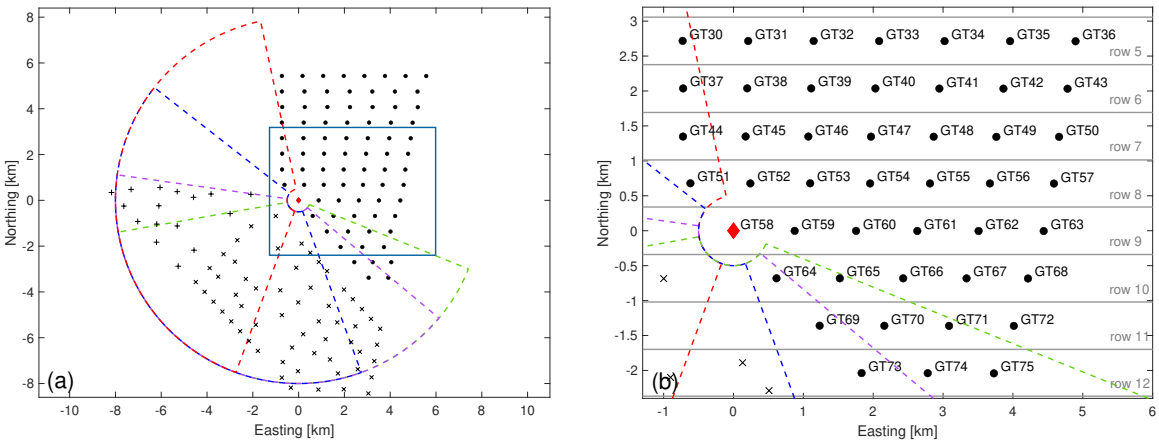

Figure 4.1: Layout of the wind farm Global Tech I with turbine positions visualized as black dots. Further, the neighbouring wind farms Albatros (+) and Hohe See (×) are shown. The lidar location is depicted as red diamond and lidar trajectories as coloured dashed lines. The Cartesian grid is centered around the lidar's position. Grey horizontal lines mark turbine rows referred to in this work. The blue rectangle indicates the zoomed-in region shown on the right. It displays turbine numbers of the wind farm's centre region.

with that of the lidar scans. LF and SF were generated with an area of influence of $2\,D$ and a minimum of 20 required wind vectors (Theuer et al., 2021) and were resampled to contain 500 members. Forecast calibration was performed with a 5 h training interval before forecast initialization. The time window was optimized in a sensitivity analysis. A calibration was only performed for situations with at least 60 % valid data within that training period.

To construct a joint predictive distribution of all turbines of GT I a sufficiently large training data set with simultaneously available forecasts of all turbines is required. As a consequence of the limited forecast availability, we therefore only considered subsets of turbines to generate and evaluate aggregated power forecasts in this work. Turbine subsets were selected based on the availability of simultaneously available forecasts and their proximity to each other (see Fig. 4.1b). Here, a 6 h training window was used, again determined using a sensitivity analysis.

For forecast calibration, training of the copula and forecast evaluation 1 Hz SCADA power data, averaged to 1 min intervals, were used.

4.3.2 Evaluation of lidar-based and SCADA-based power forecasts for individual wind turbines

We evaluate 5 min ahead power forecasts generated within the period 8 March to 21 June 2019 against 1 min mean SCADA data. In total, 9438 valid forecasts were generated, and 6753 were successfully calibrated. Hereby, we considered only situations during which both lidar and SCADA data were available for forecast generation and evaluation and persistence forecasts were available as a reference. The benchmark persistence assumes the future value equals the current observation. A probabilistic version of persistence was constructed by adding forecasting errors of the past 19 time steps to the current forecast as described by Gneiting et al. (2007). Further, forecasts of individual turbines not in normal operation mode were neglected. The wind conditions of the 9438 analysed time steps are summarized as a wind rose in Fig. 4.2. Wind speed and wind direction were extracted from the horizontal PPI lidar scans. The Obukhov length L reaches values as small as $-27\,\mathrm{m}$ in unstable and $11\,\mathrm{m}$ in stable cases. Median values of L are $-266\,\mathrm{m}$ for $L < 0$ and $268\,\mathrm{m}$ for $L > 0$, respectively. In the following analysis we will distinguish between stable ($L > 0$) and unstable ($L < 0$) atmospheric conditions in accordance with the definition of the stability-corrected logarithmic wind speed profile.

The forecast skill was determined by means of the average continuous ranked probability score:

$$\overline{\mathrm{crps}} = \frac{1}{N} \sum_{i=1}^{N} \mathrm{crps}_i. \tag{4.14}$$

To compare the skill of two forecasts the crps skill score (crps ss)

$$\mathrm{crps\ ss} = 100 \left(1 - \frac{\overline{\mathrm{crps}}}{\overline{\mathrm{crps}}_{\mathrm{ref}}} \right), \tag{4.15}$$

with the reference forecast $\overline{\mathrm{crps}}_{\mathrm{ref}}$ is applied.

To understand the impact of lidar coverage and turbine location on the forecast skill and forecast availability of LF and SF, we depict the number of available forecasts for each method in Fig. 4.3a and b. In Fig. 4.4 we further compare the crps ss of the LF and SF with persistence as reference for individual turbines of GT I and distinguish between unstable and stable atmospheric conditions. Based on the number of available forecasts the turbines GT30–GT75 (see Fig. 4.1) were selected for further analysis. Grey vertical lines mark horizontal wind turbine rows, with the turbine to the left of the line located on the easterly side of the wind farm.

The westerly corner of the wind farm shows high LF availability (see Fig. 4.3a). In

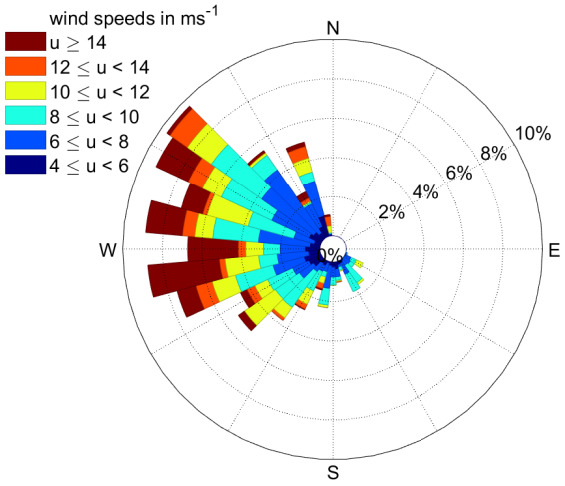

Figure 4.2: Wind speed and wind direction distribution extracted from horizontal PPI lidar scans of the 9438 analysed time steps.

agreement with this, the LF was able to outperform persistence during unstable atmospheric conditions for those turbines covered well by the lidar scans (e.g. GT52, GT58, GT64). Its forecast availability is reduced for turbines located further away from the lidar. Here, also the forecast skill is low. This can be attributed to the longer time and distance wind vectors need to travel before reaching these turbines. Even though we consider in addition to the current lidar scan also previous ones, missing or low-quality scans increase the risk of wind vectors not reaching the turbines and negatively impact forecast skill. Moreover, high uncertainty might be related to wake effects. Wind turbines located in the northerly region of the wind farm show a low skill score due to insufficient lidar coverage. The SF mainly covers the easterly part of the wind farm and consequently performs well for easterly located turbines (e.g. GT50, GT57, GT63; see Fig. 4.4), also during unstable conditions. It cannot predict free-flow turbines, considering the main westerly wind direction, as no upstream turbines are available to propagate from. Hence, skill scores are lower for turbines positioned close to the first row. Overall, the results indicate that both methods are able to predict power of not only free-stream turbines but also wake-influenced turbines more accurately than persistence under unstable conditions. During stable stratification both methods fail, in particular the SF.

Other than the SF, the LF is not bias-corrected to account for systematic errors possibly related to wakes. We therefore consider it worthwhile to analyse the impact of wakes on the LF in more detail. To do so, the $\overline{\text{crps}}$ and the bias of GT30–GT75 are depicted in Fig. 4.5 for wind directions $260-280°$ (Fig. 4.5a and b) and $170-190°$ (Fig. 4.5c and d). To capture in particular situations strongly impacted by wakes, we included only stable atmospheric conditions and situations operating below rated power

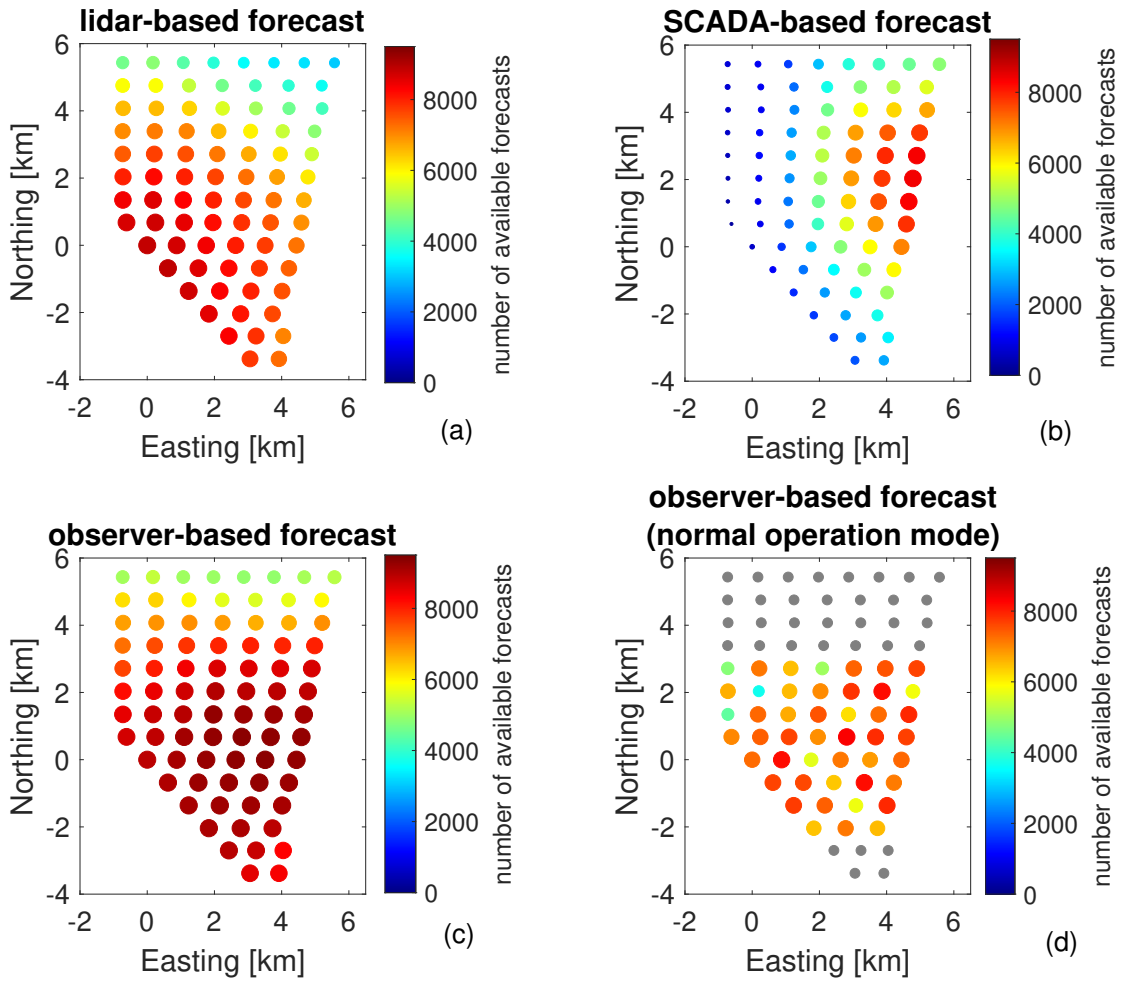

Figure 4.3: Forecast availability for (a) the lidar-based forecast, (b) the SCADA-based forecast, (c) the observer-based forecast and (d) the observer-based forecast after filtering situations during non-normal operation. The subset of turbines shown in colours in (d) is analysed in more detail in this work, while turbines marked in grey are not considered for further analysis. The colour scale and magnitude of the dots visualize the number of valid forecasts.

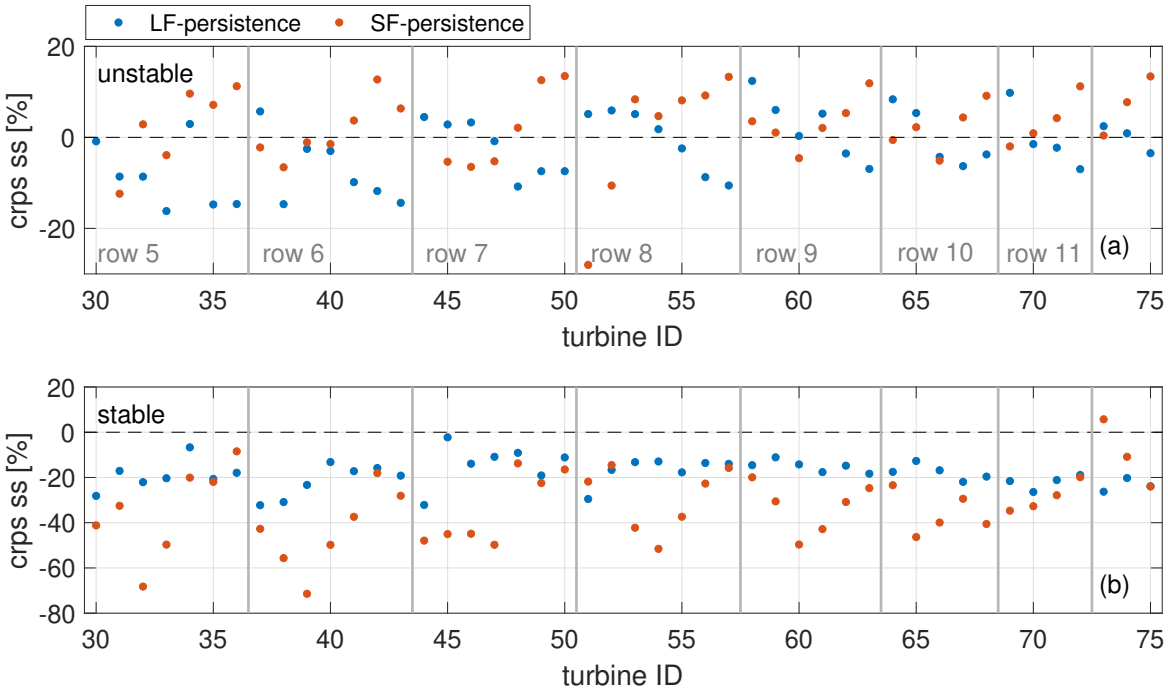

Figure 4.4: The crps ss of LF and SF with persistence as reference for individual turbines of GT I and distinguishing between (a) unstable and (b) stable atmospheric conditions. Grey vertical lines mark horizontal wind turbine rows.

($< 0.9\,P_\mathrm{r}$) in this analysis. The $\overline{\mathrm{crps}}$ deteriorates, i.e. is growing, with increasing distance to the free-stream turbines. In accordance with the wind directions, forecasts are most accurate for westerly located turbines in Fig. 4.5a and for southerly located ones, with the exception of GT75, in c. The bias is not distinctly affected by the individual turbines' position in the wind farm and fluctuates closely around zero for westerly winds. For southerly winds, scores are generally slightly larger, and the bias of most turbines lies between 0.5 % and 1.5 %.

The LF's dependency on lidar coverage was already shown in previous work (Theuer et al., 2020b). Here, we focused on the SF's sensitivity to missing turbine data. In the case of failing measurement devices or maintenance operations, wind speed and wind direction information might be missing or inaccurate for some turbines during periods of time. Here, we analysed how the SF's forecast skill is affected by missing turbines. To do so, we randomly excluded an increasing amount of wind turbines as the origin of wind vector propagation for the whole analysed time period. We will refer to the number of turbines considered as turbine availability in the following. In Fig. 4.6 we compare the forecast availability and the $\overline{\mathrm{crps}}$ normalized with respect to 100 % turbine availability for a number of exemplary turbines that have shown high forecast availability. The normalized $\overline{\mathrm{crps}}$ in Fig. 4.6b only considers simultaneously available forecasts for all filter criteria.

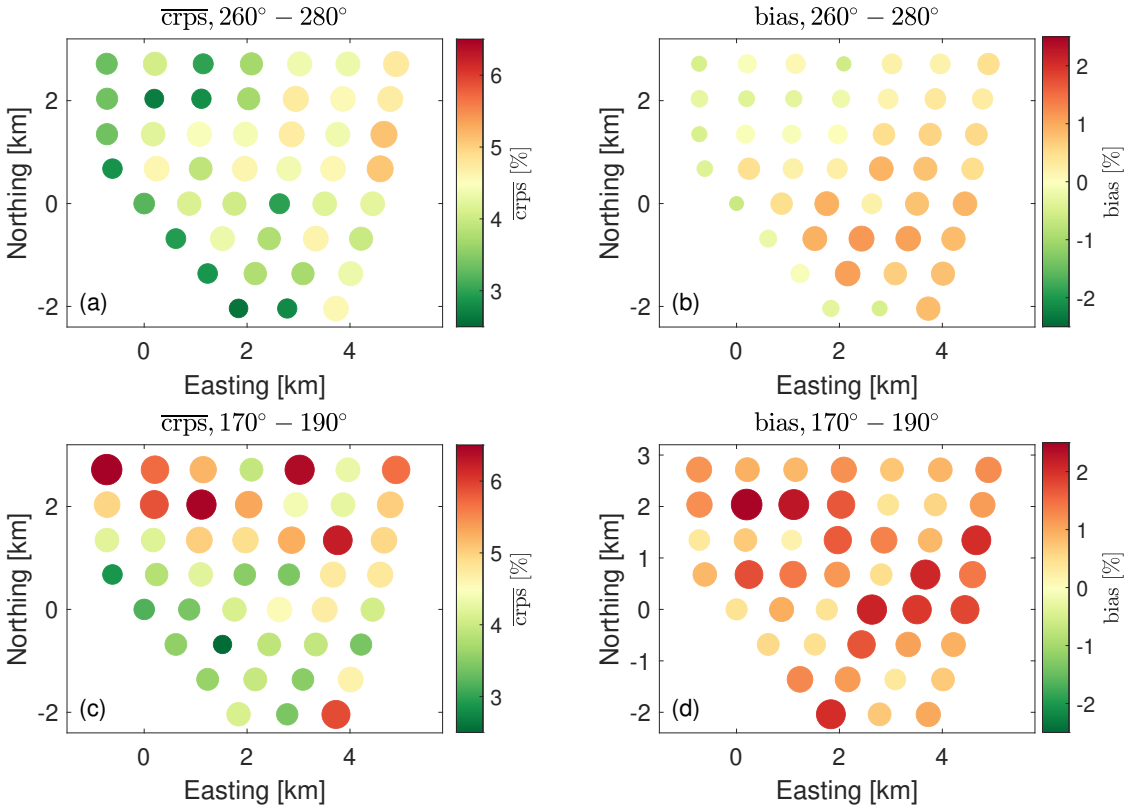

Figure 4.5: The $\overline{\text{crps}}$ and bias of the LF for turbines GT30–GT75 in % of rated power for stable atmospheric conditions, situations below rated power and wind directions (a,b) $260-280°$ and (c,d) $170-190°$. The colour scale and magnitude of the dots visualize the magnitude of the scores.

A reduction in turbine availability clearly causes a decrease in forecast availability and skill for all of the analysed turbines. The impact of missing turbines increases with lower turbine availability. For GT36, for instance, a reduction in turbine availability from 100 % to 50 % reduces the forecast availability to 97 % and increases the $\overline{\text{crps}}$ by 4.8 %. Further reducing turbine availability to only 25 % lowers the forecast availability by another 10.6 % and increases the $\overline{\text{crps}}$ by 11.5 %. A similar behaviour can be observed for turbines GT35 and GT42. Only for turbine GT56 do the forecast availability and $\overline{\text{crps}}$ change rather linearly.

4.3.3 Extension to an observer-based power forecast of individual wind turbines

A main advantage of the OF compared to the LF or SF is its increased forecast availability. This is visualized in Fig. 4.3, where the number of available forecasts for the 80 turbines of GT I for LF, SF and OF is shown. It becomes clear that the LF and SF complement each

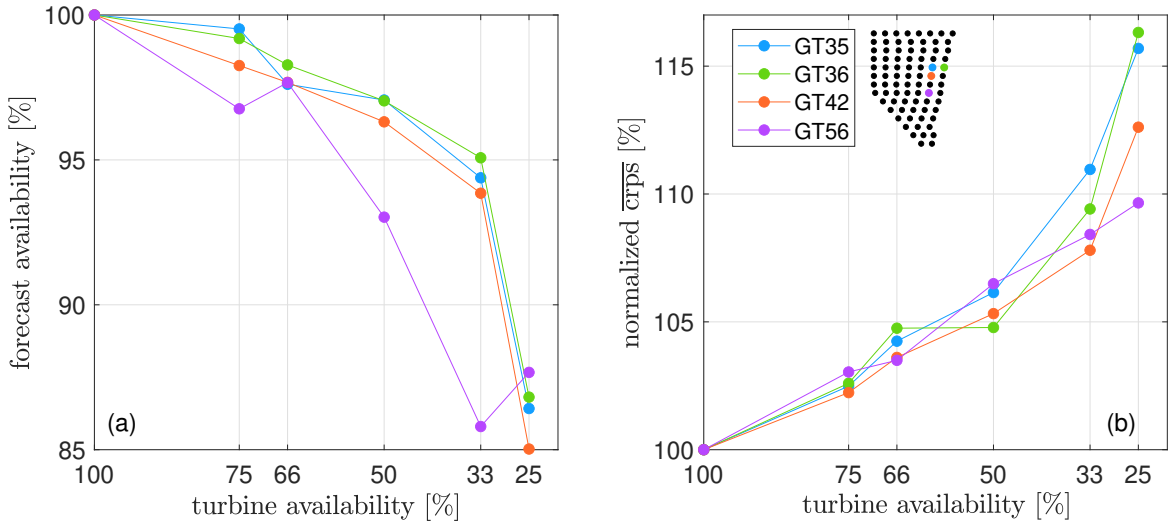

Figure 4.6: (a) Forecast availability in % and (b) $\overline{\text{crps}}$ normalized with respect to 100 % turbine availability in % for reduced turbine availability and selected example turbines. The wind farm layout visualizes the turbines' positions.

other well in terms of data availability (see Sect. 4.3.2) from which the OF can benefit. It shows high availability in the wind farm's centre, which decreases when approaching the north-westerly and south-easterly region of the wind farm. This is a consequence of lidar trajectories, wind farm layout and wind conditions at the site. The OF's availability for the selected turbines, GT30–GT75, after filtering turbines during non-normal operation (see Sect. 4.3.2) is depicted in Fig. 4.3d.

In addition to the forecast availability also the forecast skill can benefit from a combination of the two forecasting methodologies. Figure 4.7 depicts the $\overline{\text{crps}}$ for the OF compared to the LF, the SF and persistence for the 46 remaining turbines. To be able to compare OF and LF respectively SF we only consider situations for which both of the forecasts are available. That means that in Fig. 4.7a we only take those OFs into account that consist of either a combination of LF and SF or solely the LF. We distinguish between unstable atmospheric conditions ($L < 0$) in blue and stable ones ($L > 0$) in red. The dot size represents the number of available forecasts at the respective turbine and is scaled with the maximal value of available forecasts within each subplot. Data positioned below the diagonal black line indicates an improvement of the OF's forecast skill compared to the reference method.

In addition, in Fig. 4.8 we present the crps skill score for the individual wind turbines, distinguishing between atmospheric conditions for the same cases as visualized in Fig. 4.7. The OF shows higher forecast skill for all turbines in both stable and unstable situations compared to the LF. It benefits strongest from additional SFs for turbines located far

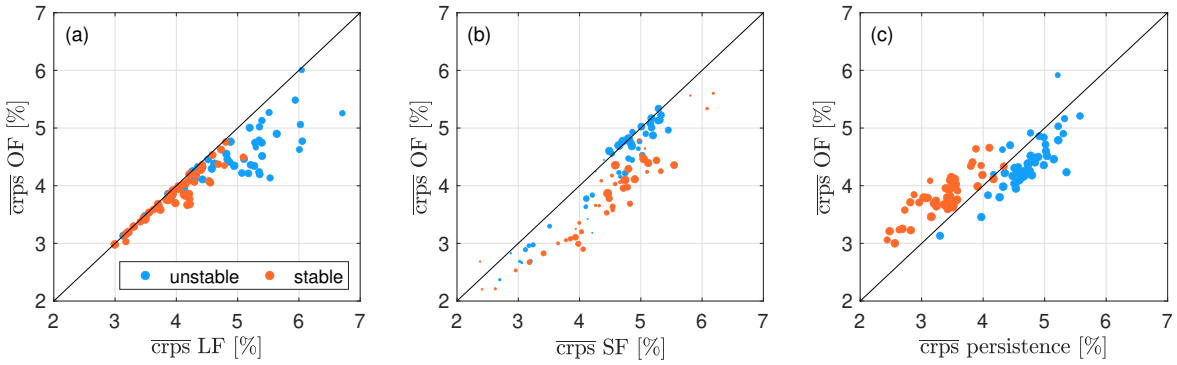

Figure 4.7: Comparison of $\overline{\text{crps}}$ of the observer-based forecast to the (a) lidar-based forecast, (b) SCADA-based forecast and (c) persistence (% of the turbines' rated power). Each dot represents $\overline{\text{crps}}$ for one of GT I's wind turbines (GT30–GT75) both for stable and unstable atmospheric conditions. The dot size scales with the number of forecasts considered. Only situations with forecasts available for both methods are considered.

away from the lidar scans, which are most affected by the LF's long wind vector travelling distances and times and possibly by wake effects. A number of turbines for which the effect almost disappears (e.g. GT44, GT51, GT58), indicated by dots positioned close to the diagonal line and a crps ss close to 0, are visible. Those correspond to free-stream turbines for which the amount of valid SFs is small and the OF consists mainly of LFs. Also compared to the SF, the OF's $\overline{\text{crps}}$ is improved for almost all analysed turbines. The effect is most distinct during stable atmospheric conditions and for turbines close to the free-stream region of the wind farm (e.g. GT39, GT54, GT60), thus with few upstream turbines for the SF available. Here, the SF can benefit strongly from additionally available lidar data.The OF is able to outperform persistence during unstable stratification for most turbines; however, it fails to do so during stable cases. Turbines for which the OF underperforms during unstable cases are positioned in the northerly region of the wind farm. Those located in the centre of the wind farm (e.g. GT50–GT58) can be forecasted best due to the beneficial data basis.

4.3.4 Calibration of observer-based power forecasts of individual wind turbines

Forecast calibration aims to improve the probabilistic characteristics of forecasts. Moreover, well-calibrated forecasts are a prerequisite for the application of the copula approach (see Sect. 4.2.4). In Fig. 4.9a we therefore compare the $\overline{\text{crps}}$ of the raw and calibrated observer-based power forecast. As in Fig. 4.7, we distinguish between atmospheric con-

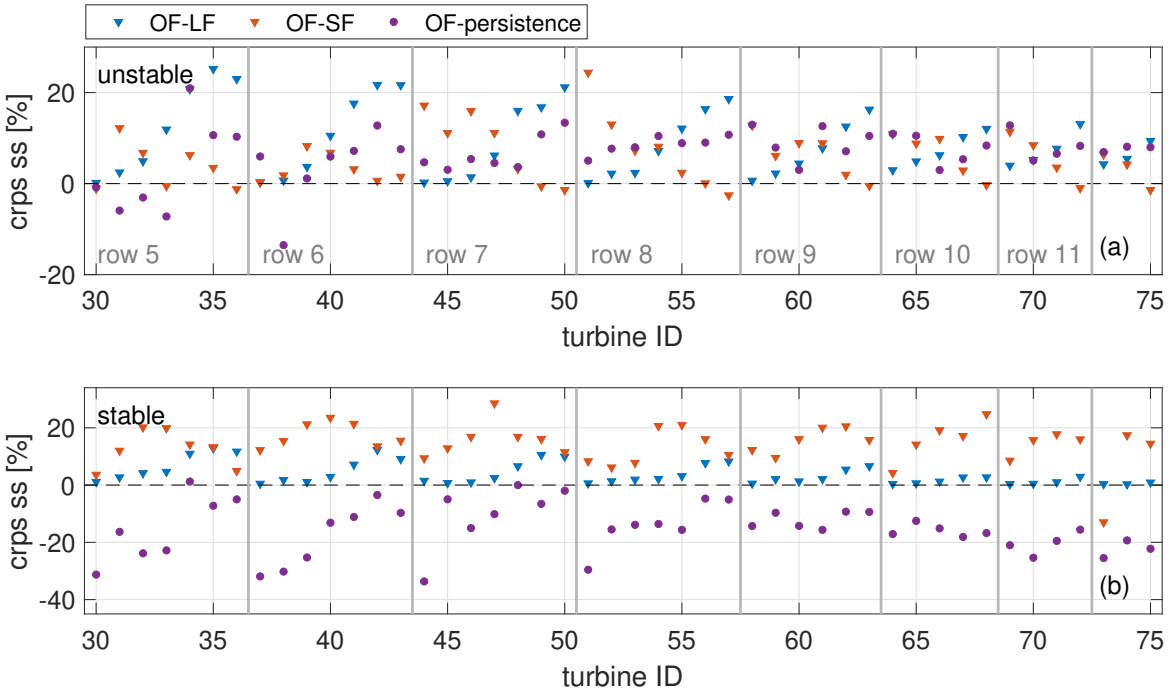

Figure 4.8: The crps ss of the OF with LF, SF and persistence as reference for individual turbines of GT I and distinguishing between (a) unstable and (b) stable atmospheric conditions. Grey vertical lines mark horizontal wind turbine rows.

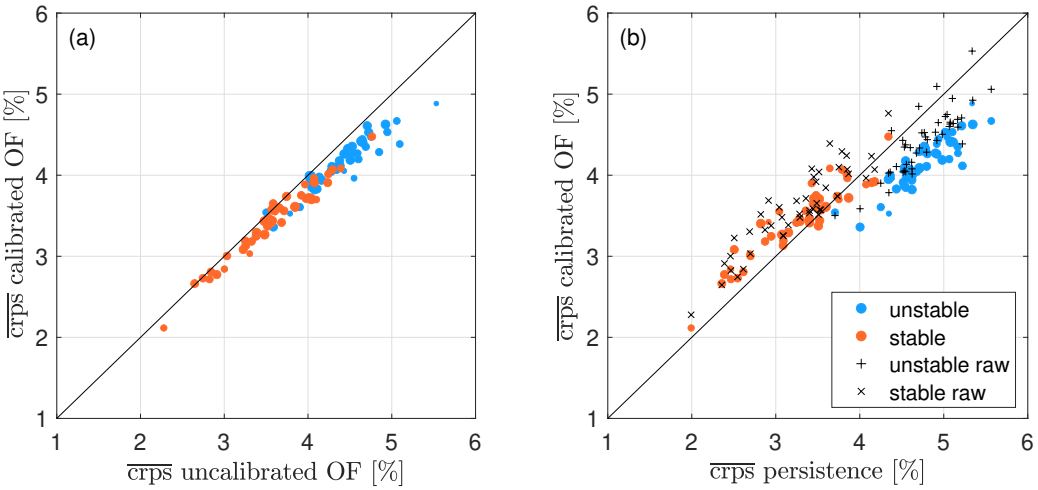

Figure 4.9: Scatterplots as described in Fig. 4.7. In (a) calibrated and raw observer-based forecasts are compared and in (b) the calibrated observer-based forecasts in colour and the raw observer-based forecasts as black markers are compared to persistence.

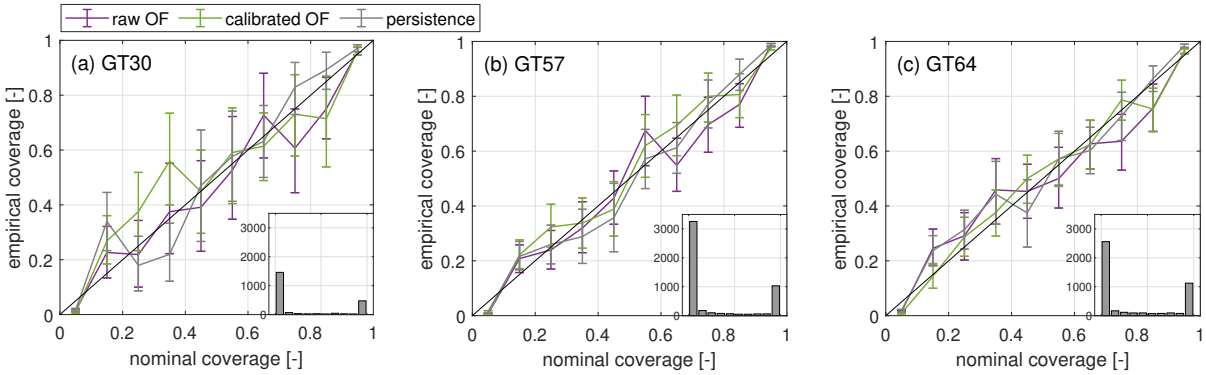

Figure 4.10: Reliability diagrams of the raw observer-based forecast (purple), the calibrated observer-based forecast (green) and persistence (grey) for turbines GT30, GT57 and GT64. The 95 % confidence intervals are visualized as error bars. The diagonal black line indicates perfect reliability. Histograms show the number of valid forecasts per quantile step for the calibrated forecast.

ditions and scale the marker size according to data availability. For almost all of the analysed turbines the OF's skill was considerably improved by calibration. The effect seems most distinct for turbines with less accurate forecasts, which often coincide with lower data availability. A comparison of the OF and persistence in Fig. 4.9b reveals that persistence is outperformed only for few of the turbines during stable atmospheric conditions. However, the OF is now more skilful than persistence during unstable situations for all analysed turbines.

In addition to $\overline{\text{crps}}$ we use reliability diagrams to evaluate the consistency between the statistics of the forecast and the observation. The reliability diagrams in Fig. 4.10 visualize the analysed quantile steps $[0, 0.1, ..., 1]$ on the x axis. For each time step the likelihood that a certain threshold is exceeded is determined from the forecast members and assigned to its specific quantile bin. The fraction of observations actually exceeding the threshold for those time steps is shown on the y axis. In this case, we define a threshold of $0.9\,P_\mathrm{r}$. Accurate probabilistic forecasts of high-power regimes are particularly important for grid integration and trading. The 95 % confidence intervals of the reliability diagrams are determined by means of a bootstrapping approach and visualized as error bars. Due to the limited number of available forecasts, we did not distinguish between atmospheric stability when evaluating reliability diagrams.

To analyse differences in reliability dependent on turbine location we selected the exemplary turbines GT30, GT57 and GT64. The reliability diagram of GT30 fluctuates more strongly around the diagonal, and its confidence intervals are broad compared to GT57 and GT64. As visible in the histogram, this is related to a smaller number of valid forecasts, which in turn is a consequence of the turbine's location in the northerly region

of the wind farm. In general, the data basis is too poor to draw any conclusions from comparing the different methods or turbine locations. Overall, the OF seems reasonably well calibrated.

4.3.5 Evaluation of aggregated wind turbine power forecasts

As explained in Sect. 4.3.1, the aggregation of individual turbines' power forecasts requires a large number of simultaneously available turbine forecasts. Furthermore, these individual forecasts need to be well-calibrated (Bessa, 2016). To have sufficiently large data sets that also allow for a distinction between atmospheric stability available we therefore limited our analysis to a maximum number of seven turbines per subset. Turbines within one subset were selected as those in close proximity to each other to increase the number of simultaneously available forecasts. To test the copula approach for a number of different circumstances, we selected subsets covering different parts of the wind farm, e.g. the westerly part in subset 1 and the easterly part in subset 3, and arranged in different shapes, e.g. an elongated turbine cluster stretching from the wind farm's south-westerly to north-easterly region in subset 2, a more dense cluster of turbines near the free-flow region in subset 4 or a horizontal wind turbine row in subset 5.

Table 4.1: Turbine subsets, number of valid forecasts considered and $\overline{\text{crps}}$ in (% of the subsets' rated power) for the vine, empirical and exponential copula approach and persistence for unstable and stable atmospheric conditions. The lowest scores are shown in bold.

	Subset	1	2	3	4	5
	Turbines	45, 46, 52, 58, 59, 65	40, 45, 46, 52, 58	42, 43, 48, 50, 55, 56, 57	51, 52, 58, 59, 64, 65	51, 52, 53, 54, 55, 56, 57
$\overline{\textbf{crps}}$ [%] unstable	N	1012	1101	612	1074	876
	Persistence	2.32	2.99	3.39	**2.29**	2.20
	Vine	**2.20**	2.68	**2.82**	2.42	**2.05**
	Empirical	2.21	2.68	2.83	2.42	2.07
	Exponential	2.21	**2.67**	2.85	2.42	2.08
$\overline{\textbf{crps}}$ [%] stable	N	529	489	279	537	350
	Persistence	**2.88**	**2.31**	**2.89**	**2.57**	**2.81**
	Vine	2.94	2.61	3.14	2.80	3.04
	Empirical	2.94	2.59	3.12	2.80	3.03
	Exponential	2.95	2.59	3.12	2.80	3.02

Table 4.2: The RMSE (% of the subsets' rated power) for the vine, empirical and exponential copula approaches, the deterministic approach and persistence for unstable and stable atmospheric conditions. The lowest scores are shown in bold.

	Subset	1	2	3	4	5
rmse [%] unstable	Persistence	5.17	6.12	6.32	**4.59**	**4.80**
	Deterministic	**5.08**	**5.59**	5.58	5.07	4.92
	Vine	5.11	5.65	5.56	5.09	4.92
	Empirical	5.11	5.67	**5.54**	5.10	4.94
	Exponential	5.11	5.66	5.58	5.09	4.94
rmse [%] stable	Persistence	**5.25**	**4.21**	**5.41**	**4.51**	**5.01**
	Deterministic	5.59	5.02	5.81	5.24	5.58
	Vine	5.61	5.03	5.84	5.27	5.59
	Empirical	5.62	5.01	5.86	5.29	5.61
	Exponential	5.62	5.01	5.82	5.28	5.59

In addition to probabilistic forecasts of aggregated wind turbine power, we also evaluated deterministic power forecasts using the root-mean-squared error (RMSE)

$$\mathrm{rmse} = \sqrt{\frac{1}{N}\sum_{i=1}^{N}(\mathrm{fc}_i - \mathrm{obs}_i)^2} \tag{4.16}$$

with forecasts fc_i and observations obs_i with time index i and number of analysed forecasts N.

We generated deterministic forecasts of turbine subsets by aggregating deterministic forecasts of individual turbines and refer to this method as deterministic OF in the following. Deterministic forecasts of individual turbines were determined by averaging their ensemble members. Additionally, the ensemble members of the subsets' probabilistic power forecasts determined using the three different copula approaches, namely the empirical Gaussian copula, the parametric Gaussian copula and the vine copula (see Sect. 4.2.4), were averaged. The turbine subsets used, the number of valid forecasts considered within each subset, and the results for the different copula approaches and persistence are summarized in Tables 4.1 and 4.2 for unstable and stable atmospheric conditions. Further, reliability diagrams of all subsets and approaches are shown in Fig. 4.11. The average absolute difference between empirical and nominal coverage for quantile steps q

and their number N_q is summarized as quantile mean absolute error (mae),

$$\text{quantile mae} = \frac{1}{N_\mathrm{q}} \sum_{q=1}^{N_\mathrm{q}} |\text{empirical coverage}_q - \text{nominal coverage}_q|. \tag{4.17}$$

and is additionally shown in Fig. 4.11f.

In terms of $\overline{\mathrm{crps}}$, four out of five subsets are able to outperform the benchmark persistence during unstable atmospheric conditions. For stable atmospheric conditions, persistence performs best. Generally, forecast skill is higher for the aggregated forecasts compared to those of individual turbines due to the smoothing of power fluctuation averaging. For three subsets unstable atmospheric conditions can be predicted more accurately than stable situations by all evaluated methods, contradicting previous results. A comparison of the different approaches and subsets with regard to their reliability and quantile mae is not conclusive, considering the overlap of the wide confidence intervals. This is a consequence of the small number of available forecasts. In terms of RMSE, the copula approaches are able to outperform persistence for three and the deterministic OF for only one of the evaluated subsets during unstable atmospheric conditions (see Table 4.2). During stable cases, persistence is most accurate for all five subsets. Overall, scores are very similar for the three tested approaches, and none of them can be identified as superior.

The analysis of the covariance matrices revealed their dynamic behaviour over time. The sliding-window approach allows the covariances to adapt to changing atmospheric conditions. In Fig. 4.12 we show average empirical and exponential covariance matrices of subset 1 for different conditions. We distinguish between atmospheric stability, average power production of free-flow wind turbines (GT30, GT37, GT44, GT51, GT58, GT64, GT69, GT73) and average wind direction of turbines GT30–GT75. We select covariances considering conditions during the 6 h time window used for copula training. A comparison of empirical (left, Fig. 4.12a, c, e, g, i and k) and exponential covariance matrices (right, Fig. 4.12b, d, f, h, j and l) makes clear that covariances are smoothed by the parameterization. For exponential covariances, a distinct dependency on the turbines' spacing can be observed. Figure 4.12a–d show that, as expected, covariances are on average higher during stable atmospheric conditions than during unstable cases. In Fig. 4.12e–h we compare covariances of situations with turbines operating below rated power ($< 0.9\,P_\mathrm{r}$) and those running at rated power ($\geq 0.9\,P_\mathrm{r}$). Slightly larger values can be observed below rated power. In Fig. 4.12i–l we analyse the covariances' dependency on wind direction. To exclude the impact of atmospheric stability and power production, we only consider cases with stable stratification and turbines operating below rated power here. To maximize the number of valid covariance matrices, relatively large wind direction intervals of

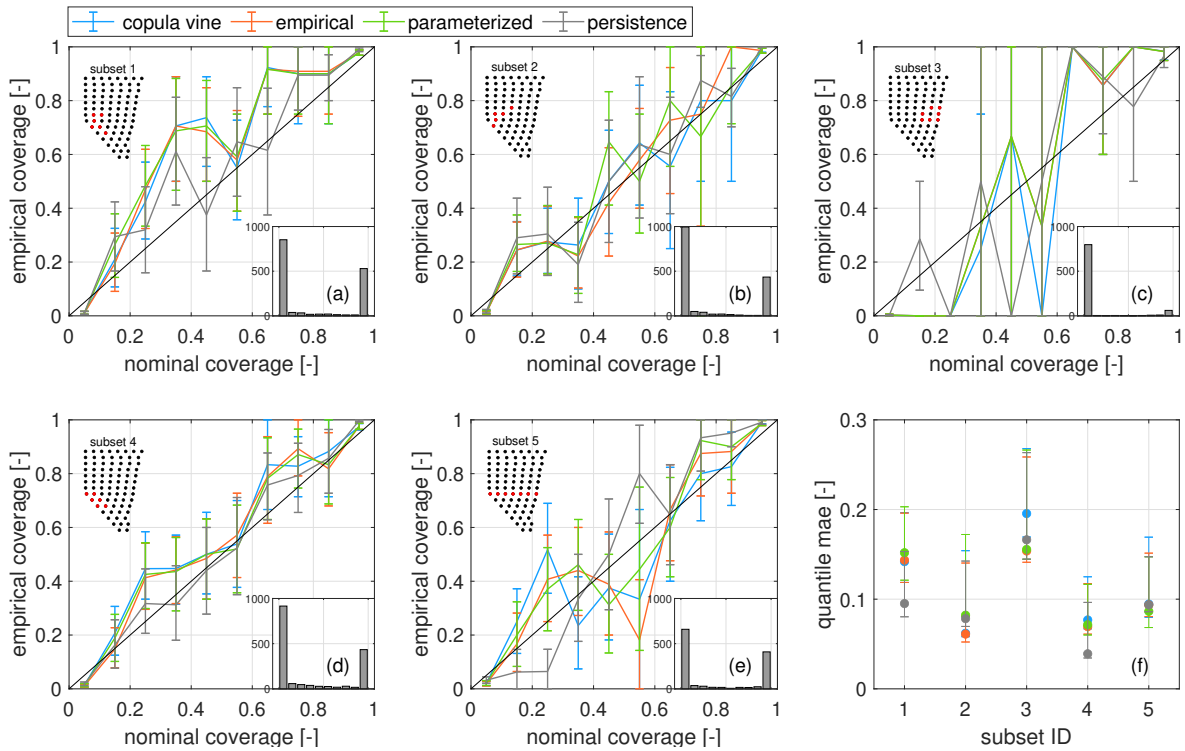

Figure 4.11: (a)–(e) Reliability diagrams for the different turbine subsets (1–5) and copula approaches summarized in Table 4.1 and persistence. The turbine subsets are marked in red in the small wind farm layouts. Histograms show the number of valid forecasts per quantile step for the empirical copula approach. The diagonal black line indicates perfect reliability. In (f) the corresponding quantile maes are shown. For all subfigures 95 % confidence intervals are visualized as error bars.

$240 - 300°$ and $< 240°$ are chosen. Overall, covariances are higher for westerly winds as compared to south and south-westerly winds. We relate this mainly to changing wake situations. We exemplarily analyse the covariances' dependency on wind direction using turbine pairs GT45–GT46, GT45–GT52 and GT46–GT52. While for westerly winds the average covariance of GT45–GT52 is higher than that of GT45–GT46 and GT45–GT52, it is lower for south and south-westerly winds. This can be explained because for westerly winds, GT45 and GT52 experience similar wake conditions and are positioned approximately perpendicular to the incoming wind. In contrast, for south and south-westerly winds, their wake situation is different, with GT52 placed upstream of GT45. Here, GT45–GT46 and GT46–GT52 are subject to more similar wake effects and exhibit higher covariances. It should be noted that the number of covariance matrices considered for the different filter criteria varies considerably.

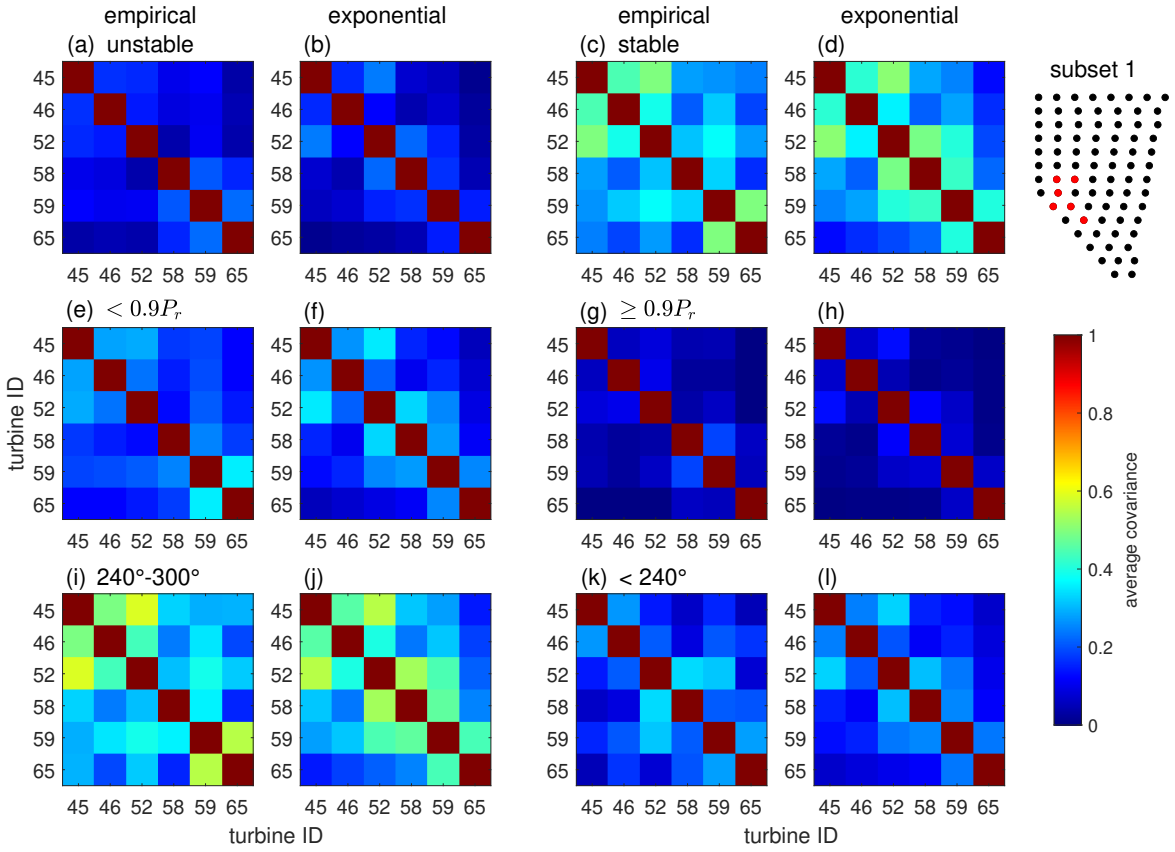

Figure 4.12: Average covariances of turbine subset 1 determined using the empirical (left: a, c, e, g, i, k) and exponential (right: b, d, f, h, j, l) copula approaches. Unstable (a, b) and stable (c, d) cases and situations with turbines operating below ($< 0.9\,P_\mathrm{r}$) (e, f) and at rated power ($\geq 0.9\,P_\mathrm{r}$) (g, h) are compared. In (i)–(l) stable situations with turbines operating below rated power with wind directions ranging from $240-300°$ (i, j) and $< 240°$ (k, l) are depicted. The turbine subset 1 is marked in red in the small wind farm layout.

4.4 Discussion

In the following, we review the lidar- and SCADA-based forecasting methodologies with regard to the impact of wakes and data availability. Further, the generation and calibration of the observer-based forecast, as well as the aggregation of individual power forecasts by means of a copula approach, are discussed. Finally, we assess the value of minute-scale power forecasts of offshore wind in a broader context.

4.4.1 Lidar- and SCADA-based power forecasts of individual wind turbines

In previous work (Theuer et al., 2020b, 2021) we have focused on the forecast of the first row of wind turbines, with respect to the main wind direction, only. Here, we extended the forecast to all wind turbines of the wind farm, also including waked wind turbines. Generally, the LF's skill is highest for free flow turbines and areas covered well by the lidar scans. As discussed in more detail in Theuer et al. (2020b), lidar range, scanning trajectory and wind farm layout do not only influence the forecast availability but can also impact forecast uncertainty and relate to e.g. a forecast bias. Our analysis has revealed that forecasting errors are larger for wind turbines and wind directions directly impacted by wakes, while a systematic over- or underestimation of wind speed was not observed. That means, that the LF is generally able to capture the mean wake effect; however, it is not able to forecast small-scale fluctuations associated with it. The LF considers, just like persistence, past observations at the turbine of interest that are then multiplied with the wind speed tendency determined from lidar data (see Sect. 4.2.1). It is thus able to account for wakes to some extent. We assume that the higher errors observed are mainly related to turbulence in wake regions that cannot be represented well by Lagrangian advection. Furthermore, wind vectors reaching turbines positioned in the easterly and north-easterly region of the wind farm were typically propagated over a longer distance and time compared to turbines closer to the lidar scans. These vectors can be associated with higher uncertainty. For the SF, forecasts are most accurate in the region of the wind farm opposite to the prevailing wind direction, i.e. the north-easterly region. Here, the applied bias correction prevents systematic errors. Wind vector propagation of the SF is affected more strongly by wakes than the LF as it is performed at hub height. Also Valldecabres et al. (2020) accounted for wakes in their work by applying a directional turbine efficiency, which significantly improved their results. However, the forecast was only able to outperform persistence in terms of $\overline{\text{crps}}$ for wake-influenced turbines during ramp events.

The SCADA-based forecast introduced in this work is based on a high-frequency (0.2 Hz) flow reconstruction and prediction methodology developed by Rott et al. (2020). We extended this work to a probabilistic approach by resampling the selected wind vectors by also considering the weights assigned to them and included a power transformation. Rott et al. (2020) applied and validated their model to a high-frequency data set, aiming at applications in wind turbine control. In our work, we focus on 1 min mean forecasts with a temporal resolution of 2.5 mins, in accordance with the lidar scans. Therefore, we adjusted the methodology to pre-select wind vectors following the lidar-based forecasting

methodology, considering only those reaching an area of influence within a certain time window before applying the inverse temporal distance weighting. As opposed to Rott et al. (2020), we neglected the spatial distance weighting and relied solely on the temporal distance weighting, using a Shepard parameter of $p = 4$. Rott et al. (2020) state that the usage of large Shepard parameters results in a more accurate representation of wind speed fluctuations, while lower parameters allow a robust forecast of average wind speeds. We chose a medium parameter as a good compromise between robustness and temporal resolution of wind speed fluctuations.

While the flow reconstruction method was applied only to forecasts with lead times up to 120 s, the results indicated that an application to forecasts with larger lead times might be valuable. Rott et al. (2020) showed that forecast accuracy decreases with lead time; however, its skill compared to persistence increases. Our results confirm the methodology's benefit compared to persistence for lead times of 5 min. Inaccurate wind direction data might impact the accuracy of SCADA-based forecasts. Wind direction was determined using the absolute yaw position and wind vane of each turbine, both of which are subject to uncertainties (Mittelmeier and Kühn, 2018; Simley et al., 2021). Rott et al. (2020) identified the model's approach to consider wakes and disturbances of the sonic anemometers and consequently wind direction measurements as additional sources of uncertainty.

The SF is able to account for missing data to some extent. It can thus be considered robust against the lack of data of individual wind turbines that might occur during daily operation of a wind farm due to maintenance or failing measurement devices. Only with more distinct reductions in turbine availability were forecast skill and forecast availability significantly reduced. In that case, gaps are too large, and important information is lost. How strongly missing turbine data impacts forecast accuracy is also dependent on wind speed, wind direction and the target turbine's position. They could, just like insufficient lidar coverage, cause systematic forecasting errors.

4.4.2 Extension to an observer-based power forecast, forecast calibration and aggregation

The lidar- and SCADA-based forecasts complement each other well in terms of data availability. Further, the forecast skill of the observer-based forecast outperforms both individual methods. Our analysis clearly showed that both forecasting methods, LF and SF, profit from the additional data set considered in the OF. While we relate this mainly to an improved data basis for certain areas of the wind farm, a combination can also benefit

from the individual forecasts' methodical differences. During unstable situations the SF was most significantly improved for turbines close to free-flow turbines due to significantly improved coverage. For stable stratification, the largest improvement shifts to turbines located further downstream. We relate this to more pronounced wake effects during stable stratification. As suggested previously, the LF is able to account for wakes more accurately than the SF (see Sect. 4.3.2 and Sect. 4.4.1), which means it can significantly increase the SF's value in such situations. For turbines located far away from the lidar, when propagated lidar wind vectors are associated with high uncertainty due to wakes and their increased propagation distance and time, the OF mainly benefits from more recent SCADA wind vectors.

It is common practice in (power) forecasting to combine different forecasting approaches to improve performance. Junk et al. (2015), for instance, combined different ensemble prediction systems to multi-model ensembles. They introduced different weighting approaches, namely implicit weighting, equal weighting and optimized weighting. The authors found that optimized weighting did not improve forecast calibration, while implicit weighting, which is based on the different number of ensemble members of the models, performed best. In our work, we were not able to apply implicit weighting as the number of wind vectors selected for the forecast strongly depends on the different spatial and temporal scales of the data sources. Future work should analyse how the different numbers of wind vectors reaching a certain turbine using the LF or SF can be considered in the weighting, thus moving from the equal weighting approach to a more implicit one.

Forecast calibration by means of ensemble model output statistics allows one to correct for systematic errors, as well as ensemble spread. By using a moving-time-window approach it is also possible to account for systematic errors varying with atmospheric conditions, for instance wind direction-dependent wake losses. Varying atmospheric stability and turbulence intensity that might impact power fluctuations can be addressed by adapting the forecast spread.

As we were only able to aggregate a maximum of seven turbines, it is not yet possible to draw any conclusion regarding the copula approach's ability to predict the total wind farm power. Results indicate, however, that copulas can be a valuable tool to support the generation of probabilistic forecasts. Even though we generally expect persistence to have an advantage compared to observer-based methods for aggregated wind power forecasts as power fluctuations are averaged out, persistence underperformed for four out of five subsets in terms of $\overline{\text{crps}}$ during unstable conditions. The higher skill during unstable situations compared to stable ones for three of the analysed subsets contradicts previous results (Theuer et al., 2020b, 2021). It is likely related to a higher number of situations

with turbines operating at rated power, which are associated with a higher forecast skill. Gilbert et al. (2020) applied a similar methodology to aggregate individual wind turbines' power forecasts and were also able to beat two benchmarks, namely a quantile regression model and an analogue ensemble method. However, their forecast's lead time was much larger, its temporal resolution was much lower, and a distinction between stability cases was not made, making a comparison difficult. The high temporal resolution of the OF might be one reason why covariances in our study are generally lower compared to the results of Gilbert et al. (2020). We found the magnitude of covariances to be dependent on atmospheric stability, turbine spacing, power production and wind direction. The small data set makes a more detailed distinction between different conditions difficult. Covariances are lower in situations with many power fluctuations, as expected during unstable atmospheric conditions and when turbines are subjected to wakes. Also for high-power regimes, when typically the ensemble spread is narrow, quantiles are less correlated, and thus the covariances are low. In cases where power forecasts and actual power production of neighbouring turbines can be expected to be rather similar, covariances are higher. This might happen due to more homogeneous wind fields upstream, typically during stable atmospheric conditions, and when the impact of wakes on the neighbouring turbines is similar.

An analysis of the RMSE revealed that for deterministic forecasts of turbine subsets it is more skilful to aggregate individual deterministic wind turbine forecasts. The comparison of different copula approaches suggests the use of an empirical or parametric copula instead of a vine copula. Vine copulas are more computationally expensive; however, they are able to achieve only marginally better results. Similar conclusions were drawn by Bessa (2016) and Gilbert et al. (2020). Results also varied for different turbine subsets. This is possibly related to different numbers of turbines considered, the different skill of the individual turbines' forecasts or varying distributions of atmospheric conditions within the data sets. For Sklar's theorem to hold, marginal distributions of forecasts need to be uniformly distributed. While our forecasts were reasonably well calibrated, further improvement would possibly also have benefits in the copula generation.

4.4.3 Future value of minute-scale offshore wind power forecasts

For future minute-scale forecasts of offshore wind power, considering, for example, the large number of wind farms in the North Sea and also their close proximity to each other, it might be beneficial to include operational data of several wind farms into the observer-based forecast. We expect that these additional data sources could further increase data availability, enhance forecast skill and in particular enlarge the forecast horizon. In such

a case, however, one would need to carefully calibrate the forecast to include operational data from different wind farms. The availability of lidar-based forecasts could further be increased by deploying several lidar devices and by developing more powerful lidars, e.g. with considerably increased range or scanning speed. This might facilitate multi-elevation scans with a better resolution of the rotor swept area of future very large offshore turbines.

The forecast skill of lidar-based, SCADA-based and consequently observer-based forecasts is expected to decrease with increasing lead time as a consequence of assumptions made during Lagrangian advection as discussed in previous studies (Würth et al., 2018; Rott et al., 2020; Theuer et al., 2020b). An observer-based forecast covering large areas of, for example, the North Sea is therefore not expected to be able to forecast small-scale structures very accurately. However, it would likely be able to predict the occurrence of power ramps caused, for example, by passing fronts. It was shown in numerous studies and confirmed in this work that remote-sensing-based forecasts are able to outperform persistence in particular during unstable or turbulent situations and also during ramp events (Valldecabres et al., 2020; Theuer et al., 2021). We expect this to be true also for forecast horizons larger than 5 min, which we were restricted to in this work (Theuer et al., 2020b). The development of an early warning system of potentially grid-critical power ramps based on observer-based forecasts covering the North Sea is therefore considered a valuable extension to persistence. To this end, further analysis will investigate how the forecast skill for larger horizons compares to that of persistence during different conditions.

The overall value of observer-based forecasts compared to persistence for longer time periods will strongly depend on typical atmospheric conditions at the wind farm site. During stable atmospheric conditions forecasts are generally more accurate, but the OF is not able to outperform persistence (Theuer et al., 2021). In those cases, applying persistence should be considered instead or possibly a hybrid model that includes persistence (Theuer et al., 2022b).

The aggregation of individual wind turbine power forecasts using a copula approach was strongly restricted by limited data availability in this work. As shown in other work (Valldecabres et al., 2018a; Theuer et al., 2020b) and previously discussed the availability of forecasts is strongly dependent on lidar trajectories, wind farm layout and wind conditions. Excluding certain operating conditions of turbines further reduced the available data set. That means, in particular for a wind farm as large as Global Tech I, the generation of reliable simultaneously available forecasts for all turbines is difficult. Further analysis is required to evaluate how the proposed methods might benefit probabilistic power forecasts for wind farms of smaller size or with an overall higher forecast avail-

ability. Also trajectory optimization or the installation of multiple lidars instead of just one could improve the applicability of the copula approach. To evaluate the benefit of hierarchical forecasting these methods should also be compared to wind farm power forecasts that do not consider individual power forecasts on the turbine level (Pichault et al., 2021a).

4.5 Conclusions

We developed an observer-based minute-scale offshore wind power forecast by combining a lidar-based and a SCADA-based approach. To improve probabilistic forecast skill we calibrated the observer-based approach. Further, a copula methodology was implemented to generate probabilistic power forecasts of aggregated turbine subsets.

Our results revealed the high potential of a complementary use of lidar-based and SCADA-based forecasts regarding both forecast availability and skill. We conclude that a combination of SCADA- and lidar-based forecasts is beneficial for all turbines in the wind farm and during both stable and unstable atmospheric conditions. Lidar-based forecasts were less skilful for wake-influenced turbines than for free-stream ones; however, they were able to predict the mean wake effect. SCADA-based forecasts were found to be very robust against reduced turbine availability. To guarantee high availability and skill of lidar-based forecasts a careful planning of lidar scanning trajectories is required, considering main wind direction, wind farm layout and lidar capabilities.

Forecast calibration was found to significantly reduce the forecasts' average crps; however, as a consequence of the small data set no conclusions regarding the calibration's impact on reliability could be drawn. Even though forecast skill was significantly improved compared to the raw forecasts, calibrated observer-based forecasts were only able to outperform persistence during unstable rather than stable atmospheric conditions. Based on these results we conclude that for an operational use of the observer-based forecast a distinction between atmospheric conditions is useful. Given the current status of the methodology, during stable conditions it is recommended to rely on persistence. Also the use of a hybrid methodology might be beneficial and should be explored in the future. Applying the copula approach to generate aggregated probabilistic power forecasts for turbine subsets showed high potential. Empirical and parametric covariance matrices were found advantageous over vine copulas in particular considering their high computational cost. The copula approach was not able to add value to deterministic forecasts.

In future work the copula approach for probabilistic minute-scale power forecasting needs to be further analysed for wind farms with higher overall forecast availability.

Chapter 5

Hybrid use of an observer-based minute-scale power forecast and persistence[d]

Lidar-based minute-scale wind power forecasts are valuable to support grid stability and electricity trading. Current methodologies are able to outperform the benchmark persistence only during transient situations and unstable stratification. So far, methods that extend lidar-based forecasts to observer-based forecasts by embedding turbine operational data are not able to outperform persistence during stable atmospheric conditions either. In this paper we therefore analyse the complementary use of an observer-based power forecast and persistence. To do so, we implemented two hybrid approaches: The first is based on a binary decision algorithm, while the second is weighting the two methods by minimizing a cost function. We evaluated 5-minute-ahead deterministic power forecasts of the hybrid and individual models at an offshore wind farm and found the weighting approach to be most skilful. Further, the data set was extended to represent the atmospheric conditions on site for an entire typical year. The weighting approach outperformed the binary decision algorithm for both the 5-minute sample forecasts and the one year-long data set. We discuss the advantages and disadvantages of the two hybrid models and conclude that the weighting approach is the better choice. Further, it can be concluded that also

[d]The content of this chapter is identical to the peer-reviewed version of the following conference proceeding accepted in Journal of Physics: Conference Series: Theuer, F., Schneemann, J., van Dooren, M. F., von Bremen, L., and Kühn, M.: Hybrid use of an observer-based minute-scale power forecast and persistence, *Journal of Physics: Conference Series*, 2265, 022047, https://doi.org/10.1088/1742-6596/2265/2/022047, 2022.

when evaluating the forecasts over a longer period, in this case one year, the additional use of observer-based forecasts is beneficial compared to solely relying on persistence.

5.1 Introduction

In the context of the increased share of renewable energies in our power system, minute-scale power forecasts are developed to support grid integration and electricity trading (Würth et al., 2019). On these time horizons, typically statistical methods are used. A highly competitive and easy-to-implement statistical benchmark is persistence, which assumes that the current value equals the future one (Würth et al., 2019). Probabilistic extensions of persistence consider past forecasting errors to build a forecast distribution (Gneiting et al., 2007). Other time series models are, for instance, AR(I)MA (autoregressive (integrated) moving average) models that utilize a number of past measurements and in some cases forecasting errors (Würth et al., 2019). It is common to combine different forecasting models to a hybrid approach in order to increase the available information contained in the forecast, exploit the advantages of both individual methods and thereby improve forecast skill (Chang, 2014). Hybrid models can combine different types of forecasts, i. e. statistical and physical models, or forecasts with different lead times.

In the last years, remote sensing-based minute-scale wind speed and power forecasts have been the subject of research as an alternative to statistical methods (Valldecabres et al., 2020; Theuer et al., 2020b, 2021; Pichault et al., 2021a). Valldecabres et al. (2020) developed a promising radar-based approach that was able to outperform persistence for free-stream turbines and during ramp events Valldecabres et al. (2018a). Studies have shown that lidar-based forecasts (LF) are able to outperform persistence during specific situations, namely during unstable atmospheric conditions and situations with high turbulence intensity or large wind speed increments. However, also lower forecast skills were observed for other conditions (Theuer et al., 2021). A recent study that has extended lidar-based forecasts to observer-based forecasts (OF) by embedding also wind turbine operational data confirmed the superiority of persistence in particular during stable stratification (Rott et al., 2020; Theuer et al., 2022a). This suggests using observer-based methods as a complement to persistence rather than a substitute. It also implies that the benefit of OFs evaluated over longer time periods will strongly depend on the atmospheric conditions and stratification at the wind farm location.

The aim of this work is to gain a more comprehensive understanding of the benefit of observer-based power forecasts as a supplement to persistence. We develop strategies to apply the OF in combination with persistence under different atmospheric conditions.

We evaluate the forecast skill for a training data set and additionally for an artificial one year-long data set, that mimicks the atmospheric conditions at the test site.

5.2 Methodology

In this section we first introduce the observer-based power forecast that utilizes both lidar and SCADA (Supervisory Control and Data Acquisition) data. Distinguishing between atmospheric stability, the power production and wake impact, two hybrid methods combining persistence and the observer-based forecast are then introduced. The first approach is based on a binary decision algorithm and the second method weights and combines the two individual forecasts. Finally, we explain the generation of artifical one year-long OFs, hybrid forecasts and persistence forecasts by resampling from the original forecasts in order to assess the methods' usefulness over a longer time period. Hereby, the artifical data set mimicks the typical atmospheric conditions at the wind farm site.

5.2.1 Minute-scale observer-based power forecasts at the offshore wind farm Global Tech I

The 5-minute ahead lidar-based forecasts were generated for a period from March 2019 until June 2019 using horizontal plan position indicator (PPI) lidar scans performed at the offshore wind farm Global Tech I (GT I). The wind farm consists of 80 turbines of type Adwen AD 5-116 with a rated power P_r of 5 MW. Lidar scans were measured with an azimuthal resolution of 2°, an opening angle of 150°, range gates from 500 m to 7950 m in 35 m steps and an accumulation time of 2 s. The scan orientation was adjusted manually to one of four sectors according to wind direction. Figure 5.1 depicts the wind farm layout and scanning trajectories. Line-of-sight (LOS) wind speed measurements were transformed to horizontal wind speed using wind direction information estimated by means of a Velocity Azimuth Display (VAD) fit individually for each range gate (Werner, 2005). The resulting wind vectors were propagated using Lagrangian advection (Valldecabres et al., 2018a). Those vectors reaching an area of influence around the target turbine within the time interval $k \pm 30\,\mathrm{s}$, with lead time k, were selected to contribute to the wind speed forecast. Two subsequent wind speed forecasts at lidar height, one initialized at t and one at $t-k$, were used to determine a wind speed tendency. In a next step, this tendency was applied to high-frequency operational wind turbine data to determine a wind speed forecast at hub height.

Here, we additionally propagated high-frequency wind speed and wind direction in-

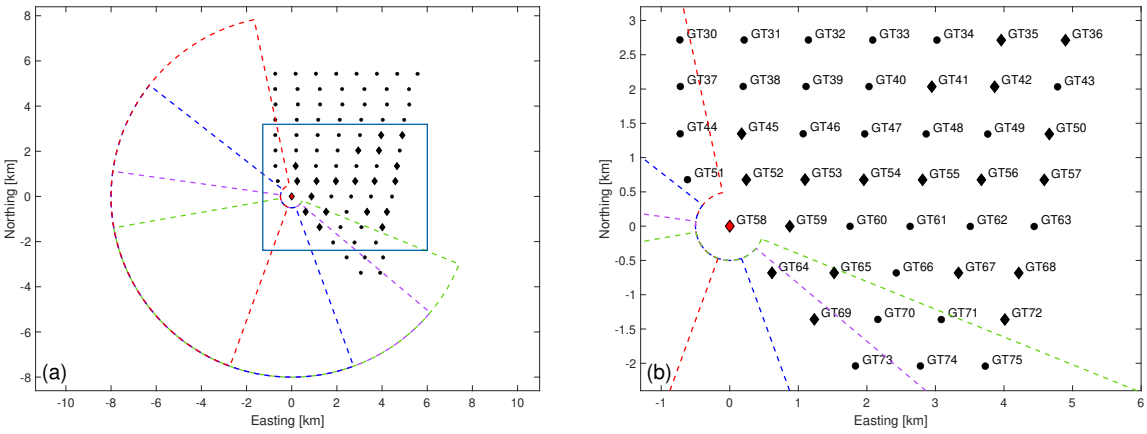

Figure 5.1: (a) Layout of the wind farm Global Tech I with turbine positions visualized as black dots. The lidar position is visualized as red diamond and scanned sectors as coloured dashed lines. The Cartesian grid is centred around the lidar's position. The blue rectangle indicates the zoomed-in region shown in (b). The 20 turbines with the highest forecast availability are marked as black diamonds.

formation obtained from GT I's wind turbine operational data as suggested by Rott et al. (2020). Wind vectors based on SCADA data were weighted according to their age and bias-corrected to account for wake effects (Theuer et al., 2022a). Lidar and SCADA contributions were resampled to the same number of wind vectors and weighted equally. Wind speed forecasts were transformed to power forecast using wind turbine power curves. Power forecasts were calibrated using an EMOS (ensemble model output statistics) approach (Thorarinsdottir and Gneiting, 2010). We will refer to this approach as observer-based forecast in the following. Both the data set and the forecasting methodology are described in more detail in Theuer et al. (2021) and Theuer et al. (2022a).

5.2.2 Hybrid methods combining the observer-based forecast and persistence

As the atmospheric conditions were found to have a strong impact on the skill of the LF and OF and their performance in comparison to persistence (Theuer et al., 2021, 2022a), we developed a hybrid methodology that aims to consider these different conditions. We used the Obukhov length L, the wind speed at 100 m height $u_{100\,\mathrm{m}}$ and the wind direction at 100 m height $\chi_{100\,\mathrm{m}}$ extracted with 10 minute resolution from a WRF (Weather Research and Forecasting Model) simulation at the location of the offshore wind farm Global Tech I (Dörenkämper et al., 2020). The wind speed was transformed into turbine power P utilizing power curves constructed from high-frequency SCADA data. L, $\chi_{100\,\mathrm{m}}$

and P were further linearly interpolated to the forecast's time steps and used to categorize the forecasts into power and stability bins. Hereby, we distinguished between unstable ($-1000\,\mathrm{m} < L < 0\,\mathrm{m}$), neutral ($|L| >= 1000\,\mathrm{m}$) and stable ($0\,\mathrm{m} < L < 1000\,\mathrm{m}$) stratification and low ($0.05\,P_\mathrm{r} \leq P < 0.2P_\mathrm{r}$), medium ($0.2\,P_\mathrm{r} \leq P < 0.9\,P_\mathrm{r}$) and high power production ($P \geq 0.9\,P_\mathrm{r}$). We further considered if turbines were placed inside the wake of surrounding turbines or not. This information was extracted from $\chi_{100\,\mathrm{m}}$ and the wind farm layout. As we expect wake influences to be less important for the upper and lower power ranges and we wanted to avoid overfitting as a consequence of too little available data, we made this distinction only for the middle power range.

Subsequently, each bin was bisected into a training data set, that was used to optimize the hybrid forecast, and a test set to evaluate the methodology. To combine the OF and persistence we used two approaches. For the first approach, referred to as binary method in the following, the root-mean-squared error (rmse) of each bin's training data set was compared for the OF and persistence. The method with the lower score was deemed superior for the selected bin and applied to corresponding situations in the test data set. For the second approach, referred to as weighting method, the observer-based forecast fc_OF and persistence $\mathrm{fc}_\mathrm{pers}$ were weighted and averaged within each bin b. The assigned weight w_b was hereby determined using a cost-function J_b

$$J_b = \sqrt{\frac{1}{N}\sum_{i=1}^{N}(\mathrm{fc}_{\mathrm{weighting},i} - \mathrm{obs}_i)^2} \tag{5.1}$$

that minimizes the rmse of the training data set with

$$\mathrm{fc}_{\mathrm{weighting},i} = w_b\,\mathrm{fc}_{\mathrm{pers},i} + (1 - w_b)\,\mathrm{fc}_{\mathrm{OF},i}, \tag{5.2}$$

the number of considered time steps N and the observation obs.

Hybrid forecasts were evaluated in terms of rmse, bias and rmse skill score (ss)

$$\mathrm{rmse\,ss} = 100\left(1 - \frac{\mathrm{rmse}}{\mathrm{rmse}_\mathrm{ref}}\right). \tag{5.3}$$

The rmse of the reference forecast is denoted $\mathrm{rmse}_\mathrm{ref}$. For a perfect forecast with $\mathrm{rmse} = 0$ or $\mathrm{rmse} \ll \mathrm{rmse}_\mathrm{ref}$ the skill score equals $100\,\%$ and is negative for $\mathrm{rmse} > \mathrm{rmse}_\mathrm{ref}$.

For the analysis we focused on turbines GT30-GT75 shown in Figure 5.1 (b) as the forecast availability of the remaining turbines, positioned in the northerly and southerly region of the wind farm, is low due to insufficient lidar and SCADA coverage.

5.2.3 Extension to a one year-long data set

To assess the usefulness of the OF, the hybrid methods and persistence, they have to be evaluated over a longer period of time. A meaningful time period would, for instance, be one year. Hereby, the atmospheric conditions need to be considered as they strongly impact the methods' forecast skill. The duration of the measurement campaign and therefore the available forecasts do not cover a sufficiently large time period. We therefore extrapolated the available data set to a whole year mimicking typical atmospheric conditions at the wind farm site. To do so, we utilized wind speed, wind direction and atmospheric stability information at GT I extracted from WRF in the period 2010-2019 (Dörenkämper et al., 2020). This information was binned using stability regimes as described in Section 5.2.2, the wind speed intervals $[4;8;12;35]\,\mathrm{m\,s^{-1}}$, and the wind direction intervals $[170;200;230;260;290;320;350]^\circ$. Wind directions in the range from 350° to 170° were not considered. This is based on the assumption that a single lidar device is able to sufficiently cover an azimuth range of approximately 180°. In accordance with that, the available forecasts are not able to sufficiently cover a wider set of wind directions. Also the available forecasts were binned according to these criteria and using data extracted from WRF. The number of average occurrences per year was then determined for each bin and the corresponding number of forecasts was drawn from the binned forecasts using a random sampling technique with replacement. A bootstrapping method was applied to determine the significance of the results. In cases with no forecasts available within a certain bin, we first enlarged the wind direction bin by allowing a selection from the two adjacent bins. In a second step, we enlarged the wind speed bin in the same manner, and finally only considered stability information. This procedure was applied as the highest impact on forecast skill is expected to be related to atmospheric stability based on results from previous work (Theuer et al., 2021). Extended forecasts were evaluated in terms of rmse and bias.

5.3 Results

5.3.1 Hybrid methods combining the observer-based forecast and persistence

The OF, persistence and the two introduced hybrid methods were evaluated using 1-minute-mean SCADA data. Hereby, only situations under normal operating conditions were considered. Figure 5.2 compares the rmse of all forecasts for turbines GT30-GT75 for (a) unstable, (b) stable and (c) neutral atmospheric conditions. The number of valid

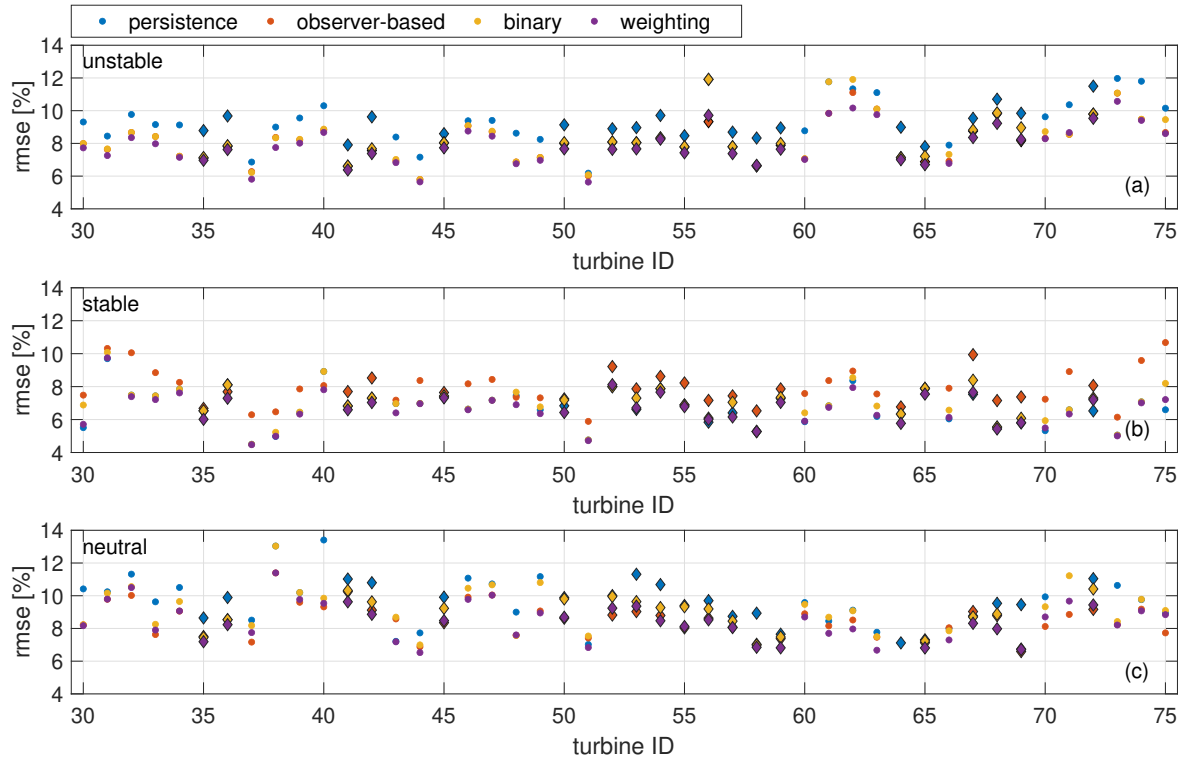

Figure 5.2: The rmse of persistence, the OF and the hybrid methods for the turbines GT30-GT75 of GT I distinguishing between (a) unstable, (b) stable and (c) neutral atmospheric conditions. The rmse is given in % of the wind turbines' rated power. The 20 turbines with the highest forecast availability are marked by ♢.

forecasts varies for the different turbines as a consequence of wind speed, wind direction, wind farm layout and the lidar trajectories. In unstable cases persistence has the largest rmse for most of the analysed turbines. The weighting method shows an improved skill compared to the OF, while the binary method shows scores similar to the OF, outperforming it in few cases. Similar as observed in previous work persistence outperforms the OF during stable stratification (Theuer et al., 2021, 2022a). For most turbines, the skill of the binary approach is lower than that of persistence but higher than that of the OF. The weighting approach performs only slightly better and is able to outperform persistence for some of the turbines. In neutral situations generally the weighting method performs best, followed by the OF and binary method.

After comparing the scores of all methods for the 46 selected turbines of GT I we will focus on the 20 turbines with the highest forecast availability in the following. These turbines are marked as ♢ in Figure 5.1 (b) and Figure 5.2.

In order to analyse how the two hybrid approaches select respectively weight the individual methods under different conditions, we depict the distribution of forecasts per bin, i. e. the number of forecasts available in the training data set, as a bar plot for the

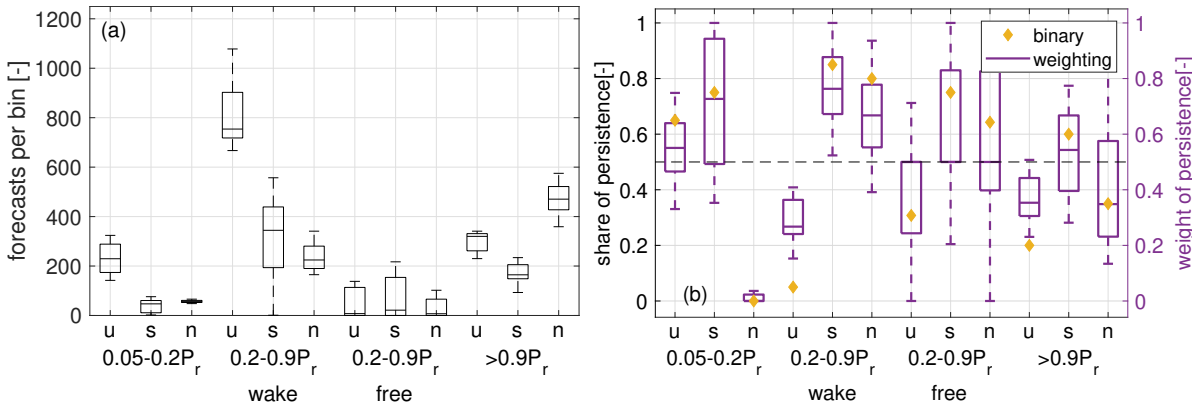

Figure 5.3: (a) Number of valid forecasts for different stability (u,s,n) and power bins. Horizontal lines show the median, the boxes include 50 % of the data. Dashed lines extend to the maximal and minimal values. (b) The share of turbines for which persistence was selected as superior forecasting method in the binary method for the different bins is shown in yellow. The weight of persistence in the weighting approach is visualized as box plot. In both subfigures only the 20 turbines with the most available forecasts are considered.

different stability classes and power regimes in Figure 5.3 (a). The median value is shown as horizontal line and the boxes include the 25% to 75% quantiles. The dashed lines extend to the minimum and maximum values. Moreover, in Figure 5.3 (b) the results of the selection algorithm for both the hybrid models are depicted. The yellow markers indicate the share of the analysed turbines for which persistence was deemed superior for the binary hybrid method and thus selected for the respective stability and power bin. The boxes represent the weight put onto persistence for the weighting approach using Equations 5.1 and 5.2. Overall, the results of the two methods agree well. The OF was weighted stronger and accordingly selected more often for unstable cases and in particular for the medium power bin and waked turbines. Low power cases are an exception, here persistence was weighted stronger than the OF. During stable cases persistence dominates the hybrid methods. For high power regimes, the weights determined for the weighted approach are distributed more closely around 0.5 than for other power regimes. Weights for free-flow and wake-influenced wind turbines are similar, with a larger spread for free-flow cases. This is probably a consequence of lower data availability, which is related to the fact that many of the considered turbines are placed within the wind farm and likely always impacted by wakes.

To answer the question to what extent and under which conditions the observer-based forecast and hybrid models are able to outperform persistence, Figure 5.4 visualizes the average rmse skill score (ss) with respect to the rmse of persistence and the median bias

of the selected turbines for different forecasts and bins. The 50 % confidence intervals are depicted as error bars. For several bins, mainly stable atmospheric conditions, the rmse skill score of the OF is strongly negative. The rmse ss of the binary method often lies close to 0. In these cases persistence was selected for most of the turbines, and thus only little improvement or decline can be observed. Negative skill scores in these cases indicate that the selection of the OF over persistence does not improve forecasts in the test data set. While the skill score of the binary method can, in the best case scenario, equal the positive ones of the OF, the weighting method has the option to outperform the OF skill score by combining the two forecasts. It outperforms persistence for most bins, the largest improvements are observed for neutral and unstable cases. Here, the OF often already has a positive rmse ss, thus outperforms persistence. Also for stable cases in the medium, wake-influenced power regime and the high power regime the rmse ss of the weighting method is positive. Even though the OF's skill is worse than that of persistence for these cases, it can add some value to a hybrid method. In the medium, wake-influenced power regime the OF's and persistence's median bias have opposite signs. This results in a lower absolute median bias of the hybrid methods, in particular of the weighting approach. For most other bins, systematic errors of the hybrid methods are above those of either the OF or persistence. For several bins, the confidence intervals are very broad, questioning the significance of the results. This is most distinct for free-flow situations and likely related to low data availability (cf. Figure 5.3 (a)).

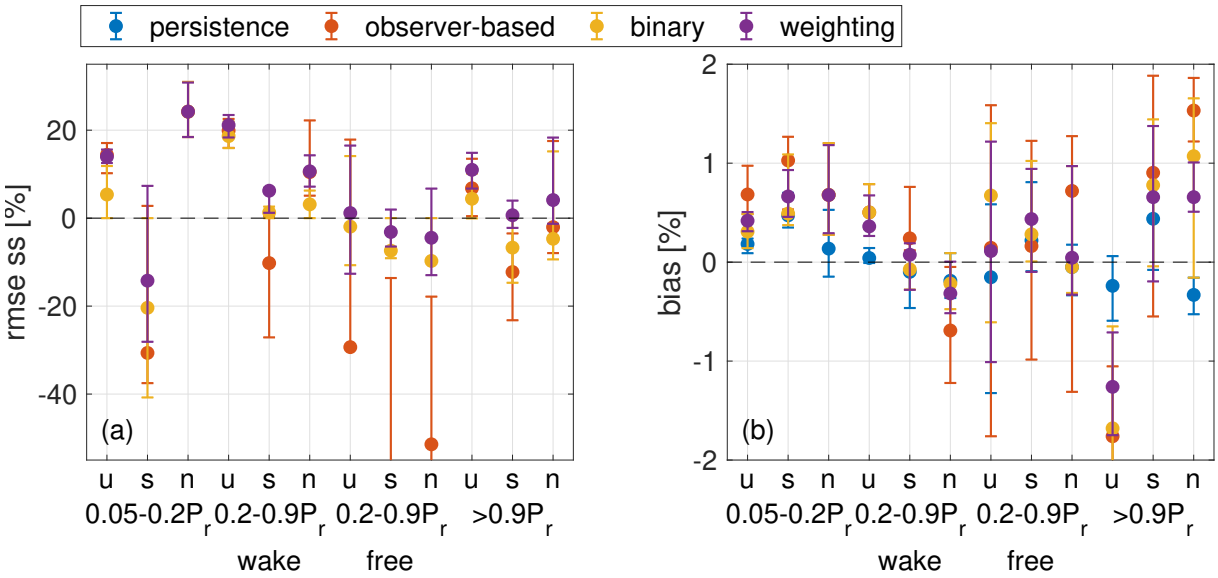

Figure 5.4: Median rmse skill score (a) and bias (b) in % of the turbine's rated power for different stability and power bins and forecasting approaches. Error bars depict 50% confidence intervals. In both subfigures only the 20 turbines with the most available forecasts are considered.

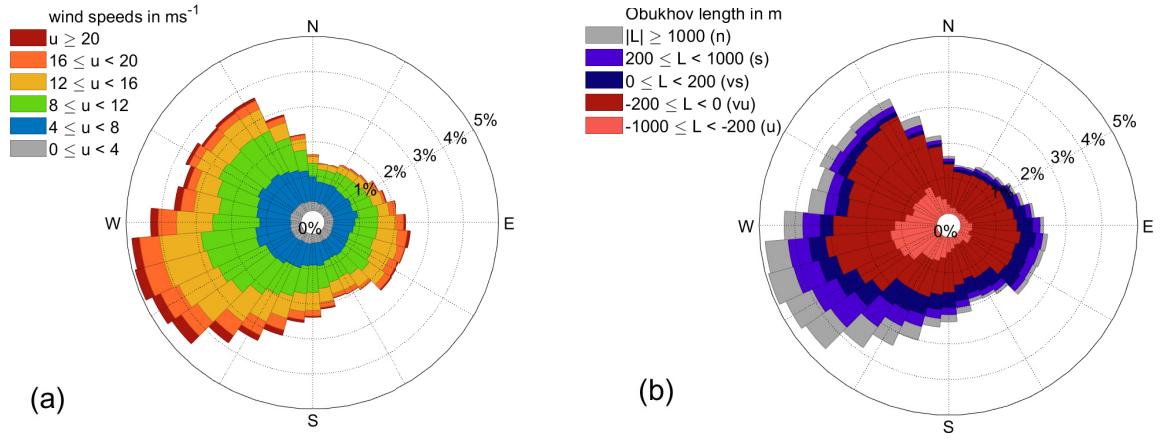

Figure 5.5: (a) Wind rose extracted from WRF at the location of GT I and a height of 100 m for a 10-year period. (b) Stability wind rose extracted from WRF distinguishing between very stable (vs), stable (s), neutral (n), unstable (u) and very unstable (vu) cases.

5.3.2 Extension to one year-long data set

As a basis for the extension to a one year-long data set, in Figure 5.5 the typical atmospheric conditions extracted from WRF simulations at the location of GT I for the years 2010-2019 are summarized. The main wind direction was identified as west/south-west as visualized in the wind rose in Figure 5.5 (a). The considered wind directions from $170° - 350°$ cover around 65.6 % of the whole data set. Further, a stability wind rose is shown in Figure 5.5 (b). The share of stable situations is largest for westerly winds and lowest for north-easterly wind directions.

In Figure 5.6 we show the stability distribution, wind speed and wind direction distribution of an average year at the location of GT I as extracted from WRF (leftmost). The distributions presented here are the binning results described in Section 5.2.3. To evaluate how accurate the atmospheric conditions were mimicked using the resampling technique and available forecasts, we additionally show distributions of those turbines of GT I highlighted in Figure 5.1 (b) and Figure 5.2 (♢). Differing wind speed and wind direction values and in particular a varying number of available forecasts for individual turbines can cause different distributions of wind speed, wind direction and atmospheric stability for the different turbines. Further, the bins shown in Figure 5.6 are finer than those applied for resampling (cf. Section 5.2.3), causing a difference between WRF and wind turbine distributions. In general, the atmospheric conditions correspond well to the ones extracted from WRF. Very stable and very unstable cases are slightly underrepresented in the artificial data set. Similarly, the number of wind speeds from $4\,\mathrm{m\,s^{-1}}$ to $6\,\mathrm{m\,s^{-1}}$ is too low. Wind directions from $170° - 230°$ are not represented well due to

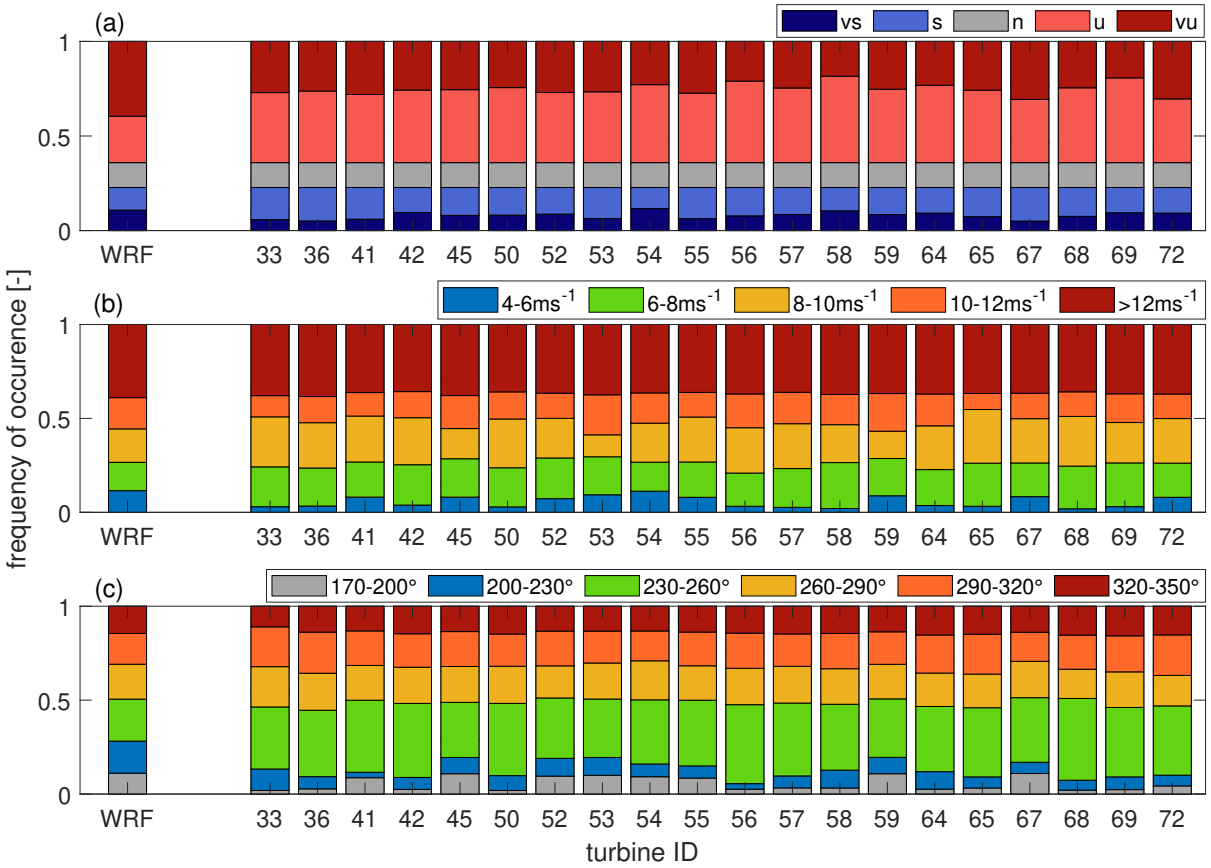

Figure 5.6: (a) Atmospheric stability, (b) wind speed and (c) wind direction distributions extracted from WRF (lefmost) and of the extended forecasts of the 20 turbines highlighted in Figure 5.2 and Figure 5.7.

limited forecast availability for these wind directions. As we use neighbouring wind speed bins as an alternative, wind directions $230° - 260°$ are over-represented.

After confirming the adequate representation of typical atmospheric conditions in the artificial data set we evaluate the forecast skill. In Figure 5.7 we show the rmse of the wind turbines GT30-GT75 in % of their rated power for the different forecasting approaches and the extended, artificially created data set. Markers represent the 50 % quantile and the 95 % confidence intervals are visualized as error bars. Moreover, average rmse values are summarized in Table 5.1. Again, the turbines with the highest number of valid forecasts are marked as $\diamondsuit$. For 44 of the 46 turbines the weighting approach provides the most skillful forecast. Considering only the turbines with the highest availability this holds for 19 out of 20. Also the average rmse of both analysed turbine subsets is lowest for the weighting approach. For many turbines persistence can be outperformed significantly by all methods. The confidence intervals are generally very narrow and results can therefore be interpreted as significant. Figure 5.6 shows that the share of unstable cases of the

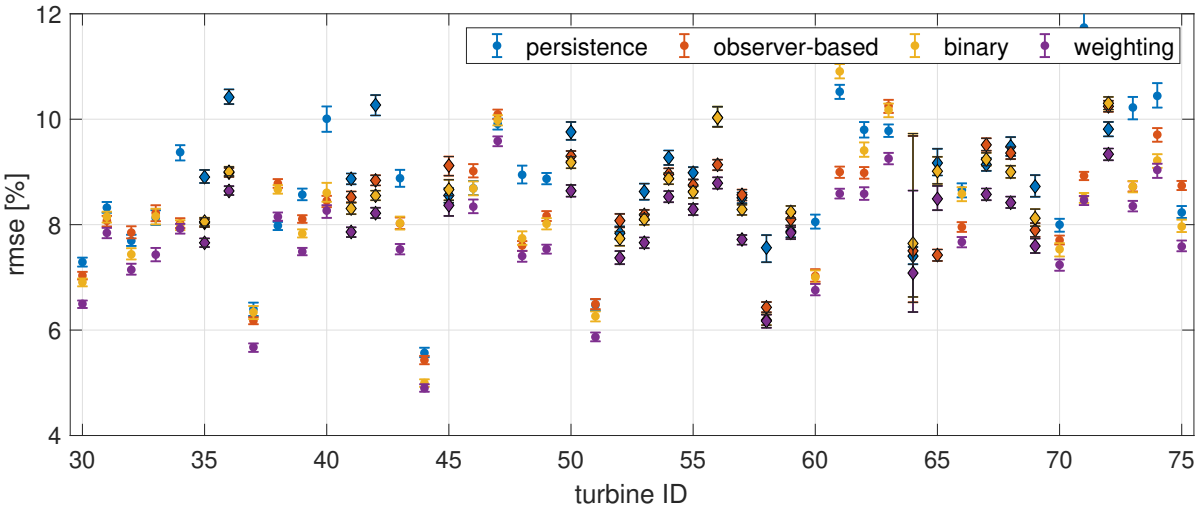

Figure 5.7: The rmse of the extended versions of persistence, the OF and the hybrid methods. The rmse is given in % of the wind turbines' rated power. Markers represent the 50 % quantile and the 95 % confidence intervals are visualized as error bars. The 20 turbines with the highest forecast availability are marked by ♢.

Table 5.1: Average rmse of persistence, the observer-based forecast and the two hybrid methods for the artificially created data set in % of rated power. Lowest scores are shown in bold.

	persistence	**observer-based**	**binary**	**weighting**
GT30-GT75	8.82	8.34	8.33	**7.83**
high availability, 20 turbines	8.96	8.55	8.56	**8.06**

considered data set lies at around 64.1 %. As shown in Section 5.3.1, the OF and hybrid methods are able to outperform persistence during those cases.

5.4 Discussion

5.4.1 Hybrid methods combining the observer-based forecast and persistence

The two hybrid methods introduced in this work rely on a training data set that is divided into several bins characterizing the local atmospheric conditions. Due to a limited amount of available forecasts, we were restricted to a relatively small number of bins in this study. For future work, a finer distinction between atmospheric conditions might be beneficial. However, in this case study it would have likely led to overfitting. Also, larger training data sets might have improved the results. Generally, it should be further analysed what

size of training data set is sufficient and whether weights for the weighting approach deduced here could be used to generate forecasts over longer time periods. We expect this to be less critical for the binary approach.

The weighting method has advantages over the binary method as it can consider both forecasting methodologies. This allows to balance systematic errors of the individual forecasts (cf. Figure 5.4 (b)). The binary approach is based on a binary selection system. If the choice based on the training data set is wrong for the test data set, the forecast skill is maximally degraded. For the weighting approach, this might also happen if one forecast is assigned a weight of 0. However, it is more likely that results will benefit from both methods. That means using the binary method is associated with a higher risk of reducing forecast skill, while its possibility to reduce errors is limited. Overall, we found atmospheric stability to have the largest impact on the forecasts' weighting. Due to limited data availability we could not draw significant conclusions regarding the weighting for free-flow and wake-influenced turbines. Results indicate that a higher weight of OFs compared to persistence during wake-influenced cases is more skillful. In agreement with previous results, persistence is more skillful during stable atmospheric conditions and thus assigned a higher weight (Theuer et al., 2021). It stands out that for low power cases and unstable conditions persistence is also weighted more compared to the OF. This might be related to lower absolute changes in wind speed observed during these situations, possibly leading to an advantage for persistence. In Theuer et al. (2021) persistence outperformed a lidar-based forecast for 5-minute wind speed increments smaller than $0.5\,\mathrm{m\,s^{-1}}$. For high power regimes ($> 0.9P_r$) the difference in weighting between OF and persistence is less clear than for medium and low power values. Here, many situations with wind speed above rated wind speed were considered. For those cases wind speed errors have only little impact on the skill of power forecasts and the skill of both forecasting methods converges.

The complementary use of persistence and an OF was found to be most beneficial during unstable atmospheric conditions. Even during stable atmospheric conditions the OF can add additional skill to persistence.

5.4.2 Extension to one year-long data set

The extension of the forecast to a longer data set is based on the prerequisite that enough forecasts are available within each bin. The limited amount of data in this analysis restricted the bins that could be used and resulted in slightly different conditions for the artificial forecasts compared to the WRF data. The wind direction mainly influences the impact of wakes on individual turbines. The results indicate that in particular wake-influenced situations might benefit from lidar and SCADA data. We thus need to assume

that an inaccurate representation of the wind direction distribution might to some extent influence the results. Also the power regime was found to influence forecast skill. We suspect that during higher wind speeds mainly the observer-based forecast and hybrid methods gain benefits. However, as we were able to reconstruct atmospheric stability distributions well and stratification was found to have the strongest impact on forecast skill, we consider our results meaningful despite these limitations. The narrow confidence intervals support this notion (cf. Figure 5.7). The results achieved by the extension to an artificial but representative typical year prove the value of the weighting approach for an operational use.

The atmospheric conditions observed at the wind farm GT I are not untypical for offshore locations. We, therefore, assume the conclusions drawn in this study are in general applicable also to other offshore sites in the North Sea. To draw more detailed conclusions regarding the value of observer-based forecasts as a supplement to persistence one needs to analyse the conditions at each site individually.

5.5 Conclusions

This study implemented two hybrid methods, combining an observer-based forecast and the statistical method persistence, aiming to understand the benefits of their complementary use. The binary method used a binary selection of either of the two forecasts and the weighting method applied a weighting function. Generally, the weighting approach achieved more skilful results. It is more flexible and can account for systematic errors by combining the individual forecasts. The forecast skill of both the individual and hybrid methods was mainly influenced by atmospheric stability. The highest forecast skill compared to persistence was observed during unstable atmospheric conditions. However, also during stable conditions the observer-based forecast can add value to persistence. Despite the limited forecast availability, atmospheric conditions at the offshore site could be replicated accurately using the resampling technique. As the wind farm site is dominated by unstable stratification, the observer-based and hybrid methods can also significantly increase forecast skill when evaluated over longer time periods. Highest forecast skill was achieved by the weighting approach for both analysed turbine subsets, which proves its value for an operational use.

Chapter 6

Conclusions and outlook

6.1 Conclusions

The transition of the energy system to a carbon-neutral one requires a rapidly increasing share of renewable energies. Consequences of this transition are numerous challenges, such as large numbers of decentralized feed-in, limited transmission grid capacity and the strong volatility of wind and solar power. Particularly, installed wind power capacity has increased significantly over the past years and is expected to do so further. By 2025 an increase of 76 GW onshore and 29 GW offshore installed wind capacity is expected in the EU (WindEurope, 2021), for 2050 the EU aims at 300 GW offshore wind (European Commission and Directorate-General for Energy, 2020). High-capacity offshore wind farms clustered in small areas can cause strong wind power fluctuations which can severely impact grid stability. Minute-scale power forecasts can support the physical balancing of wind power and electricity trading. Probabilistic forecasts, thus forecasts containing uncertainty information, are in this regard useful for end-users. Recently, physical models based on remote sensing measurements have been proven superior to statistical models, which are typically applied on the minute-scale, in particular to predict power ramps.

In this thesis, a probabilistic lidar-based power forecast of an offshore wind farm was developed based on previous radar-based research work. Valuable insights into the forecast skill and its relation to the benchmark persistence under varying atmospheric conditions were gained. Further, knowledge regarding future measurement campaign planning and trajectory optimization was acquired. In the following, we summarize the main conclusions of the thesis in relation to the five research questions stated in Chapter 1.4.

Wind speed and power forecasts based on lidar data have been researched in the past (Valldecabres et al., 2018b; Würth et al., 2018; Pichault et al., 2021a). All these methods are based on Taylor's frozen turbulence hypothesis and generate forecasts in a

deterministic framework. In Valldecabres et al. (2018a) a probabilistic power forecast based on Lagrangian advection and dual-Doppler radar data was introduced for the first time and showed promising results. However, to offer a more feasible alternative that is also applicable to far offshore sites, a comparable methodology needed to be developed for single-Doppler lidar data. In this thesis we used horizontal PPI long-range lidar scans at an offshore wind farm to develop and implement a probabilistic lidar-based power forecast. Chapter 2 introduces a lidar-based methodology that takes into consideration the limitations of lidar devices. The following conclusions, mainly addressing research question I, were drawn:

- Single-Doppler long-range lidar scans measured with an elevation of 0° provide a feasible, cost-efficient alternative to dual-Doppler radar-based forecasts that is applicable to far offshore sites.

- The forecast skill of the developed lidar-based forecast is highly dependent on stratification. During unstable atmospheric conditions deterministic and probabilistic skill of the lidar-based forecast were higher than during neutral and stable atmospheric conditions. High errors during stable stratification are related to wind speed extrapolation from measurement height to hub height by means of a logarithmic stability-corrected wind speed profile.

- Insufficient lidar coverage reduces forecast availability and skill and can introduce significant systematic errors. Lidar trajectories, therefore, need to be optimized, taking into account wind direction and wind farm layout. In the context of single-lidar scans the region with almost perpendicular orientation (±15°) between wind direction and the azimuth angle is critical. It is subject to large uncertainty and therefore typically excluded.

- During unstable atmospheric conditions and for free-stream turbines with sufficient lidar coverage the lidar-based forecast is able to outperform the benchmark persistence in terms of rmse, mae, $\overline{\text{crps}}$ and reliability.

- The maximal possible forecast horizon is, besides wind speed and maximal measuring distance, impacted by the lidar trajectory in relation to the wind farm layout and the scan duration. Scan trajectories, therefore, need to be optimized in terms of azimuth opening angle, azimuthal resolution and scanning speed.

Results from Chapter 2 revealed significant uncertainties related to the wind speed extrapolation from the measurement to hub height. Therefore, we further classified these errors

and introduced two alternative forecasting methodologies in a next step. These methods differ in their approach to wind speed extrapolation to hub height. The first one uses lidar measurements and wind turbine operational data to derive empirical wind profile parameters. The second approach determines a wind speed tendency at measurement height from consecutive lidar-based wind speed forecasts and applies it to SCADA-based wind speed at hub height. At this stage, we focus on eliminating systematic wind speed errors and therefore analyse deterministic wind speed forecasts instead of probabilistic power forecasts. We were able to draw these main conclusions addressing research question II:

- The main drivers of uncertainty related to wind speed extrapolation to hub height by means of a stability-corrected logarithmic wind speed profile are uncertainties in temperature measurements used to determine atmospheric stability and in wind speed.

- The stability-corrected logarithmic wind speed profile is based on many assumptions and, in many cases, not a good representation of observed profiles. For instance, kinks and reserved profiles can not be represented well and lead to uncertainty in particular during stable conditions. Further, Monin Obukhov Similarity Theory only holds in the surface layer, which could impact the applicability of the logarithmic profile at hub height particularly during very stable conditions. These effects can reduce forecast skill significantly.

- Extracting wind profile parameters by applying a profile fit to lidar measurements and wind turbine operational data allows an empirical representation of profiles. It can significantly reduce forecasting errors. These effects are most distinct during situations classified as stable by meteorological measurements that show a decrease or only small increases of wind speed with height.

- The consideration of a wind speed tendency forecast in combination with recent wind turbine operational data positively impacts forecast accuracy. While upstream lidar observations can still be considered, recent SCADA data provides a solid basis for the forecast, similar to persistence. Further, less weight is put onto absolute forecasted values and extrapolation across large height distances is avoided.

- The forecast accuracy of both lidar-based methods and the benchmark persistence is strongly dependent on atmospheric conditions. Stable conditions are advantageous for both the Lagrangian advection and the assumption of a persisting wind speed. Given the current status of the methodology, during stable conditions persistence cannot be outperformed.

- The accuracy of lidar-based forecasts is related to the magnitude of 5-minute wind speed increments and turbulence intensity. Situations with high increments and turbulence intensity can be predicted more accurately by lidar-based methods. They are, therefore, considered valuable to forecast ramp events, which are characterized by strong wind speed increments.

After significantly increasing forecast accuracy for deterministic wind speed forecasts of free-flow turbines, the introduced methodology was extended to the whole wind farm, transformed to power forecasts and evaluated in a probabilistic framework. We further extended the lidar-based forecast to an observer-based forecast by the integration of a SCADA-based forecast to increase forecast availability and skill. To improve the forecast's probabilistic characteristics, it was calibrated using Ensemble Model Output Statistics. Finally, individual turbines' probabilistic power forecasts were aggregated utilizing a copula approach. We state the main conclusions from this work, addressing research questions III and IV, below:

- The lidar-based forecast can predict free-flow turbines more accurately than wake-impacted ones. No systematic over- or underprediction is observed, which means it is able to represent the mean wake effect well. Uncertainty is mainly introduced by wind vector propagation over long distances and duration and in wake regions.

- The SCADA-based forecast is robust against missing data of individual wind turbines. Only with a significant reduction of turbine availability, forecast availability and skill are severely reduced.

- The SCADA-based forecast and lidar-based forecast complement each other well in terms of forecast availability. A combination of the two was beneficial for the forecast skill compared to the methods' individual use in all analysed situations. Overall, the extension of lidar-based forecasts to observer-based forecasts significantly improves forecast availability and skill. The effect is largest for turbines positioned further away from the lidar-scanned area that are most affected by long travel distances and duration of wind vectors and wakes.

- Forecast calibration can significantly improve probabilistic forecast skill for almost all analysed turbines. Still, during stable atmospheric conditions the observer-based forecast is not able to outperform persistence.

- A copula approach is a useful tool to aggregate probabilistic power forecasts, in our work shown for a small number of wind turbines. The empirical, exponential and

vine copula approaches show similar skill. Considering the high computational costs of the vine copula approach, an application of either the empirical or exponential copula is recommended.

While the previous work has shown the observer-based forecast's ability to outperform persistence during unstable atmospheric conditions, it also revealed that during stable stratification the opposite is true. This suggest the development of a hybrid method that considers both the observer-based forecast and persistence. We therefore developed and tested two such hybrid approaches to make use of the individual methods' benefits and further increase forecast skill. The main findings, addressing research question V, are summarized below:

- A combination of an observer-based forecast and persistence to a hybrid method benefits forecast skill mainly in unstable atmospheric conditions but also for several turbines during stable cases.
- The weighting approach outperforms the binary approach as it is able to consider both individual methods and has the possibility to reduce systematic errors.
- The given weight is mainly influenced by atmospheric conditions. Persistence is given a higher weight during stable conditions and for low power regimes, when absolute wind speed changes are low. The observer-based forecast is considered more during unstable cases and for wake-impacted turbines. For high power regimes the forecast skill of both methods converges and weights are spread more evenly.
- For longer periods of time, considering the mainly unstable atmospheric conditions at the site, we expect the observer-based forecast and both hybrid methods to be advantageous over persistence. Results indicate in particular the value of the weighting approach for an operational use.

6.2 Outlook

Our work aimed to further develop methods for remote sensing-based minute-scale power forecasting. Confirming the results of several studies (Valldecabres et al., 2018a,b; Würth et al., 2018; Valldecabres et al., 2020; Pichault et al., 2021a), this thesis has shown the potential of lidar-based approaches. We were able to advance the methodological development of lidar-based forecasts significantly. Driven by the promising results, further research now needs to aim at making the introduced methodologies more applicable in power system management and electricity trading. To achieve this, the following three

goals should be pursued, namely i) an improvement of the forecast's data basis also by the further development of measurement devices, ii) the further methodological development of the forecast and iii) the integration of lidar-based forecasts into operational forecasting systems.

Lidar device development mainly aims to increase measurement ranges, which would directly increase the maximal possible forecast horizon. Also, the spatial and temporal resolution of lidar measurements and data quality could be improved and are expected to increase forecast skill. More powerful lidar devices would further be able to provide wind speed measurements in unfavourable conditions with higher reliability, positively impacting not only on forecast accuracy but also availability. An increase in forecast skill, forecast availability and forecast horizon is expected to add value to lidar-based forecasts for end-users in trading and system operation. Increased lidar abilities would also pave the way to further improve lidar trajectories, for instance, allowing for multi-elevation scans that provide wind profile information and better resolve the rotor-swept area. Generally, an automated adaption of scanning trajectories to wind conditions should be implemented. A useful tool to support trajectory optimization are lidar simulators used in combination with wind fields generated by large eddy simulations. Another issue is low pointing accuracy of lidars for large ranges, mainly caused by the thrust-induced tilt of the device. In that regard, more work should be invested in the analysis and prevention of such tilts by installing additional inclination sensors or using a Cardan suspension. In particular, accurate wind profile information was found crucial for the forecast skill of lidar-based forecasts. In this context, meteorological measurements are typically used. Another option would be the additional deployment of a profiling lidar to extract accurate profile information. Alternatively, the scanning lidars could perform profile measurements in addition to horizontal long-range scans. In this work it also became clear that the deployment of one lidar device per wind farm is not sufficient. Depending on wind farm size, layout and the prevailing wind conditions, it might be meaningful to install several devices, for instance, one at each corner of the wind farm. Moreover, the possibility of dual-Doppler lidar measurements should be considered. With several lidars installed, certain inflow areas could be covered by two devices, i. e. dual-Doppler measurements, allowing to extract two dimensional wind field information without the assumptions related to, for instance, VAD-like fits. The development of more advanced wind field reconstruction methods for dual-Doppler lidar measurements could further improve temporal and spatial resolution of the wind field information. A more accurate derivation of the horizontal wind field could in turn have a positive impact on forecast skill. Further, additional consideration of operational data of surrounding wind farms for wind vector propagation

might be beneficial and should be investigated. All of the mentioned approaches need to be tested and evaluated in future campaigns. Generally, the benefits of these additional devices and measurements need to be weighed against their cost.

The further methodological development of the forecasting method should include a more in-depth analysis of advection models, which were found to be one main driver of uncertainty. Of high interest in this regard is the estimation of propagation uncertainty dependent on different atmospheric conditions. This will become increasingly important with the extension of forecast horizon. Closely related, a more accurate representation of wakes in the advection model needs to be investigated. Of particular importance is also an in-depth analysis of ramp events, possibly including the development of ramp event "warning reports" with increased lead times. Moreover, it might be rewarding to analyse how uncertainty information resulting from different parts of the forecasting chain can be considered in probabilistic forecasts, for instance, by adapting weights of contributing wind vectors or by including uncertainty information in the calibration. The implementation of hybrid models, for example a combination of persistence and observer-based forecasts, needs further investigation. Also the analysis of a combination with machine-learning approaches or higher-order statistical models is interesting.

In parallel to the methodological development of the forecast, an assessment of its value for electricity trading and power system management must take place. In this context, a cost-benefit analysis of lidar-based forecasts over a longer period of time but also a more detailed evaluation during ramp events are of interest. Finally, forecasts need to be implemented and tested in real-time. In general, an exchange with end-users on their requirements is necessary to drive the forecast's development to higher applicability and feasibility. Promising approaches would for instance be the integration of minute-scale lidar-based forecasts into existing operational forecasting systems that cover a whole range of lead times. Here, it is important to ensure consistency between the different time horizons of different forecasting methods and to make forecasts easily available and interpretable for different end-users. This includes also the provision of aggregated probabilistic power forecasts of individual wind turbines, i. e. a probabilistic forecast of wind farm power. In addition to an application in electricity trading and power system management, the requirements, methodology and benefits of an application of remote sensing-based forecasts for wind turbine and wind farm control need to be further investigated in the future.

References

50Hertz, Amprion, Tennet, and TransnetBW: Leitfaden zur Präqualikation von Windenergieanlagen zur Erbringung von Minutenreserveleistung im Rahmen einer Pilotphase, Tech. rep., German Transmission System Operators, 2016.

Aas, K., Czado, C., Frigessi, A., and Bakken, H.: Pair-Copula Constructions of Multiple Dependence, Insurance: Mathematics and Economics, 44, 182–198, https://doi.org/10.1016/j.insmatheco.2007.02.001, 2009.

Aitken, M. L., Rhodes, M. E., and Lundquist, J. K.: Performance of a Wind-Profiling Lidar in the Region of Wind Turbine Rotor Disks, Journal of Atmospheric and Oceanic Technology, 29, 347–355, https://doi.org/10.1175/jtech-d-11-00033.1, 2012.

Attya, A., Dominguez-Garcia, J., and Anaya-Lara, O.: A review on frequency support provision by wind power plants: Current and future challenges, Renewable and Sustainable Energy Reviews, 81, 2071–2087, https://doi.org/10.1016/j.rser.2017.06.016, 2018.

Beck, H. and Kühn, M.: Dynamic Data Filtering of Long-Range Doppler LiDAR Wind Speed Measurements, Remote Sensing, 9, 561, https://doi.org/10.3390/rs9060561, 2017.

Beck, H. and Kühn, M.: Temporal Up-Sampling of Planar Long-Range Doppler LiDAR Wind Speed Measurements Using Space-Time Conversion, Remote Sensing, 11, 867, https://doi.org/10.3390/rs11070867, 2019.

Bessa, R. J.: On the quality of the Gaussian copula for multi-temporal decision-making problems, in: 2016 Power Systems Computation Conference (PSCC), pp. 1–7, https://doi.org/10.1109/PSCC.2016.7541001, 2016.

Bird, L., Lew, D., Milligan, M., Carlini, E. M., Estanqueiro, A., Flynn, D., Gomez-Lazaro, E., Holttinen, H., Menemenlis, N., Orths, A., Eriksen, P. B., Smith, J. C., Soder, L., Sorensen, P., Altiparmakis, A., Yasuda, Y., and Miller, J.: Wind and solar energy

curtailment: A review of international experience, Renewable and Sustainable Energy Reviews, 65, 577–586, https://doi.org/10.1016/j.rser.2016.06.082, 2016.

Bleeg, J., Purcell, M., Ruisi, R., and Traiger, E.: Wind Farm Blockage and the Consequences of Neglecting Its Impact on Energy Production, Energies, 11, 1609, https://doi.org/10.3390/en11061609, 2018.

Bossanyi, E.: Optimising yaw control at wind farm level, Journal of Physics: Conference Series, 1222, 012 023, https://doi.org/10.1088/1742-6596/1222/1/012023, 2019.

Bromm, M., Rott, A., Beck, H., Vollmer, L., Steinfeld, G., and Kühn, M.: Field investigation on the influence of yaw misalignment on the propagation of wind turbine wakes, Wind Energy, 21, 1011–1028, https://doi.org/10.1002/we.2210, 2018.

Bundesnetzagentur: Quartalsbericht Netz- und Systemsicherheit - Gesamtes Jahr 2020, Tech. rep., 2021.

Cali, Ü.: Grid and Market Integration of Large-Scale Wind Farms Using Advanced Wind Power Forecasting: Technical and Energy Economic Aspects, vol. 17 of *Renewable Energies and Energy Efficiency*, Kassel University Press, 2011.

Chan, P. W. and Shao, A. M.: Depiction of complex airflow near Hong Kong International Airport using a Doppler LIDAR with a two-dimensional wind retrieval technique, Meteorologische Zeitschrift, 16, 491–504, https://doi.org/10.1127/0941-2948/2007/0220, 2007.

Chang, W.: A Literature Review of Wind Forecasting Methods, Journal of Power and Energy Engineering, pp. 161–168, https://doi.org/10.4236/jpee.2014.24023, 2014.

Coblenz, M.: MATVines: A vine copula package for MATLAB, SoftwareX, 14, 100 700, https://doi.org/10.1016/j.softx.2021.100700, 2021.

Cumming, G.: Inference by eye: Reading the overlap of independent confidence intervals, Statistics in Medicine, 28, 205–220, https://doi.org/10.1002/sim.3471, 2009.

Cutler, N., Kay, M., Jacka, K., and Nielsen, T. S.: Detecting, categorizing and forecasting large ramps in wind farm power output using meteorological observations and WPPT, Wind Energy, 10, 453–470, https://doi.org/10.1002/we.235, 2007.

Dörenkämper, M., Olsen, B. T., Witha, B., Hahmann, A. N., Davis, N. N., Barcons, J., Ezber, Y., García-Bustamante, E., González-Rouco, J. F., Navarro, J., Sastre-Marugán,

M., Sīle, T., Trei, W., Žagar, M., Badger, J., Gottschall, J., Sanz Rodrigo, J., and Mann, J.: The Making of the New European Wind Atlas – Part 2: Production and evaluation, Geoscientific Model Development, 13, 5079–5102, https://doi.org/10.5194/gmd-13-5079-2020, 2020.

Dowell, J. and Pinson, P.: Very-Short-Term Probabilistic and Wind Power Forecasts by Sparse Vector Autoregression, IEEE Transactions on Smart Grid, 7, 763–770, https://doi.org/10.1109/TSG.2015.2424078, 2016.

Durran, D. R.: Semi-Lagrangian Methods, pp. 303–333, Springer New York, New York, NY, https://doi.org/10.1007/978-1-4757-3081-4_6, 1999.

Efron, B.: Bootstrap Methods: Another look at the jackknife, The Annals of Statistics, 7, 1–26, https://doi.org/10.1214/aos/1176344552, 1979.

Emeis, S.: Wind Energy Meteorology, Springer International Publishing, 2nd Edn, Springer International Publishing AG, part of Springer Nature 2018, https://doi.org/10.1007/978-3-319-72859-9, 2018.

EPEXSPOT: Intraday Lead Times, available at: https://www.epexspot.com/en/basicspowermarket, last access: 17 April 2020, 2020.

European Commission and Directorate-General for Energy: Offshore renewable energy strategy, Publications Office, https://doi.org/10.2833/756349, 2020.

European Commission, Directorate-General for Climate Action: Stepping up Europe's 2030 climate ambition - Investing in a climate-neutral future for the benefit of our people, 2020.

Felder, M., Kaifel, A., Matthiss, B., Ohnmeiß, K., Schröder, L., Sehnke, F., Würth, I., Wigger, M., and Cheng, P. W.: Optimierung der Auslegung und Betriebsführung von Kombikraftwerken und Speichertechnologien mittels Kürzestfristvorhersagen der Wind- und PV-Leistung (VORKAST) : Abschlussbericht, Zentrum für Sonnenenergie- und Wasserstoff-Forschung Baden-Württemberg (ZSW), Stuttgart, Germany, https://doi.org/10.2314/GBV:1028384602, 2018.

Frehlich, R.: Scanning Doppler Lidar for Input into Short-Term Wind Power Forecasts, Journal of Atmospheric and Oceanic Technology, 30, 230–244, https://doi.org/10.1175/jtech-d-11-00117.1, 2013.

Gao, J., Xue, M., Lee, S.-Y., Shapiro, A., Xu, Q., and Droegemeier, K. K.: A three-dimensional variational single-Doppler velocity retrieval method with simple conservation equation constraint, Meteorology and Atmospheric Physics, 94, 11–26, https://doi.org/10.1007/s00703-005-0170-7, 2006.

Gendeel, M., Yuxian, Z., and Aoqi, H.: Performance comparison of ANNs model with VMD for short-term wind speed forecasting, IET Renewable Power Generation, 12, 1424–1430, https://doi.org/10.1049/iet-rpg.2018.5203, 2018.

Germann, U. and Zawadzki, I.: Scale-Dependence of the Predictability of Precipitation from Continental Radar Images. Part I: Description of the Methodology, Monthly Weather Review, 130, 2859–2873, https://doi.org/10.1175/1520-0493(2002)130⟨2859:SDOTPO⟩2.0.CO;2, 2002.

Giebel, G., Brownsword, R., Kariniotakis, G., Denhard, M., and Draxl, C.: The State-Of-The-Art in Short-Term Prediction of Wind Power: A Literature Overview, 2nd edition, ANEMOS.plus, https://doi.org/10.11581/DTU:00000017, 2011.

Gilbert, C., Browell, J., and McMillan, D.: Leveraging Turbine-Level Data for Improved Probabilistic Wind Power Forecasting, IEEE Transactions on Sustainable Energy, 11, 1152–1160, https://doi.org/10.1109/TSTE.2019.2920085, 2020.

Gneiting, T., Raftery, A. E., Westveld, A. H., and Goldman, T.: Calibrated Probabilistic Forecasting Using Ensemble Model Output Statistics and Minimum CRPS Estimation, Monthly Weather Review, 133, 1098–1118, https://doi.org/10.1175/MWR2904.1, 2005.

Gneiting, T., Balabdaoui, F., and Raftery, A. E.: Probabilistic forecasts, calibration and sharpness, Journal of the Royal Statistical Society, 69, 243–268, https://doi.org/10.1111/j.1467-9868.2007.00587.x, 2007.

Gonzalez, E., Stephen, B., Ineld, D., and Melero, J. J.: On the use of high-frequency SCADA and data for improved wind turbine performance monitoring, Journal of Physics: Conference Series, 926, 012 009, https://doi.org/10.1088/1742-6596/926/1/012009, 2017.

Good, S., Fiedler, E., Mao, C., Martin, M. J., Maycock, A., Reid, R., Roberts-Jones, J., Searle, T., Waters, J., While, J., and Worsfold, M.: The Current Configuration of the OSTIA System for Operational Production of Foundation Sea Surface Temperature and Ice Concentration Analyses, Remote Sensing, 12, 720, https://doi.org/10.3390/rs12040720, 2020.

Grachev, A. and Fairall, C.: Dependence of the Monin-Obukhov Stability Parameter on the Bulk Richardson Number over the Ocean, Journal of Applied Meteorology, 36, 406–414, https://doi.org/10.1175/1520-0450(1997)036⟨0406:DOTMOS⟩2.0.CO;2, 1997.

Grigonytė, E. and Butkevičiūtė, E.: Short-term wind speed forecasting using ARIMA model, ENERGETIKA, 62, 45–55, https://doi.org/10.6001/energetika.v62i1-2.3313, 2016.

Gryning, S.-E., Batchvarova, E., Brümmer, B., Jørgensen, H., and Larsen, S.: On the extension of the wind profile over homogeneous terrain beyond the surface boundary layer, Boundary-Layer Meteorology, 124, 251–268, https://doi.org/10.1007/s10546-007-9166-9, 2007.

Hamill, T. M.: Reliability Diagrams for Multicategory Probabilistic Forecasts, Weather and Forecasting, 12, 736–741, https://doi.org/10.1175/1520-0434(1997)012⟨0736:RDFMPF⟩2.0.CO;2, 1997.

Hau, E. and von Renouard, H.: Control Systems and Operation Sequence Control, pp. 357–387, Springer Berlin Heidelberg, Berlin, Heidelberg, https://doi.org/10.1007/3-540-29284-5_10, 2006.

Hirth, B. D., Schroeder, J. L., and Guynes, J. G.: Diurnal evolution of wind structure and data availability measured by the DOE prototype radar system, Journal of Physics: Conference Series, 926, 012 003, https://doi.org/10.1088/1742-6596/926/1/012003, 2017.

Hirth, L. and Ziegenhagen, I.: Balancing power and variable renewables: Three links, Renewable and Sustainable Energy Reviews, 50, 1035–1051, https://doi.org/10.1016/j.rser.2015.04.180, 2015.

Holtslag, A. A. M. and De Bruin, H. A. R.: Applied Modeling of the Nighttime Surface Energy Balance over Land, Journal of Applied Meteorology and Climatology, 27, 689–704, https://doi.org/10.1175/1520-0450(1988)027⟨0689:AMOTNS⟩2.0.CO;2, 1988.

Hu, X., Jaraitė, J., and Kažukauskas, A.: The effects of wind power on electricity markets: A case study of the Swedish intraday market, Energy Economics, 96, 105 159, https://doi.org/10.1016/j.eneco.2021.105159, 2021.

Huang, C.-J. and Kuo, P.-H.: A Short-Term Wind Speed Forecasting Model by Using Artificial Neural Networks with Stochastic Optimization for Renewable Energy Systems, Energies, 11, 2777, https://doi.org/10.3390/en11102777, 2018.

Högström, U.: Non-Dimensional Wind and Temperature Profiles in the Atmospheric Surface Layer: A Re-Evaluation, Boundary-Layer Meteorology, 42, 55–78, https://doi.org/10.1007/BF00119875, 1988.

IEC: IEC 61400-12-1:2017 Wind energy generation systems - Part 12-1: Power performance measurements of electricity producing wind turbines, 2017.

ISO: International Standard ISO 2533. Standard Atmosphere, 1987.

Joos, M. and Staffell, I.: Short-term integration costs of variable renewable energy: Wind curtailment and balancing in Britain and Germany, Renewable and Sustainable Energy Reviews, 86, 45–65, https://doi.org/10.1016/j.rser.2018.01.009, 2018.

Junk, C., Delle Monache, L., Alessandrini, S., Cervone, G., and von Bremen, L.: Predictor-weighting strategies for probabilistic wind power forecasting with an analog ensemble, Meteorologische Zeitschrift, 24, 361–379, https://doi.org/10.1127/metz/2015/0659, 2015.

Kalverla, P. C., Steeneveld, G.-J., Ronda, R. J., and Holtslag, A. A.: An observational climatology of anomalous wind events at offshore meteomast IJmuiden (North Sea), Journal of Wind Engineering and Industrial Aerodynamics, 165, 86–99, https://doi.org/10.1016/j.jweia.2017.03.008, 2017.

Kelly, M. and Jørgensen, H. E.: Statistical characterization of roughness uncertainty and impact on wind resource estimation, Wind Energy Science, 2, 189–209, https://doi.org/10.5194/wes-2-189-2017, 2017.

Koch, C. and Hirth, L.: Short-term electricity trading for system balancing: An empirical analysis of the role of intraday trading in balancing Germany's electricity system, Renewable and Sustainable Energy Reviews, 113, 109 275, https://doi.org/10.1016/j.rser.2019.109275, 2019.

Lacerda, M., Couto, A., and Estanqueiro, A.: Wind Power Ramps Driven by Windstorms and Cyclones, Energies, 10, 1475, https://doi.org/10.3390/en10101475, 2017.

Lange, M. and Focken, U.: Physical Approach to Short-Term Wind Power Prediction, Springer, Berlin, Heidelberg, https://doi.org/10.1007/3-540-31106-8, 2006.

Lenzi, A., Steinsland, I., and Pinson, P.: Benefits of spatiotemporal modeling for short-term wind power forecasting at both individual and aggregated levels, Environmetrics, 29:e2493, https://doi.org/10.1002/env.2493, 2018.

Leosphere: Scanning Windcube, available at: https://www.leosphere.com/products/scanning-windcube, last access: 17 April 2020, 2018.

Liang, Z., Liang, J., Wang, C., Dong, X., and Miao, X.: Short-term wind power combined forecasting based on error forecast correction, Energy Conversion and Management, 119, 215–226, https://doi.org/10.1016/j.enconman.2016.04.036, 2016.

Malvaldi, A., Weiss, S., Infield, D., Browell, J., Leahy, P., and Foley, A. M.: A spatial and temporal correlation analysis of aggregate wind power in an ideally interconnected Europe, Wind Energy, 20, 1315–1329, https://doi.org/10.1002/we.2095, 2017.

Mittelmeier, N. and Kühn, M.: Determination of optimal wind turbine alignment into the wind and detection of alignment changes with SCADA data, Wind Energy Science, 3, 395–408, https://doi.org/10.5194/wes-3-395-2018, 2018.

Møller, M., Domagalski, P., and Sætran, L. R.: Comparing Abnormalities in Onshore and Offshore Vertical Wind Profiles, Wind Energy Science, 5, 391–411, https://doi.org/10.5194/wes-5-391-2020, 2020.

Newsom, R.: Doppler Lidar (DL) Handbook, Tech. rep., Climate Research Facility, https://doi.org/10.2172/1034640, 2012.

Nygaard, N. G. and Newcombe, A. C.: Wake behind an offshore wind farm observed with dual-Doppler radars, Journal of Physics: Conference Series, 1037, 072 008, https://doi.org/10.1088/1742-6596/1037/7/072008, 2018.

Optis, M., Monahan, A., and Bosveld, F. C.: Moving Beyond Monin–Obukhov Similarity Theory in Modelling Wind-Speed Profiles in the Lower Atmospheric Boundary Layer under Stable Stratification, Boundary-Layer Meteorology, 153, 497–514, https://doi.org/10.1007/s10546-014-9953-z, 2014.

Optis, M., Debnath, N. B. M., and Doubrawa, P.: New methods to improve the vertical extrapolation of near-surface offshore wind speeds, Wind Energy Science, 6, 935–948, https://doi.org/10.5194/wes-6-935-2021, 2021.

Ortensi, M., Theuer, F., and Kühn, M.: Analysis of the effects of scanning trajectory parameters on minute-scale lidar forecasting, Journal of Physics: Conference Series, 2265, 022 002, https://doi.org/10.1088/1742-6596/2265/2/022002, 2022.

Paulson, C.: The Mathematical Representation of Wind Speed and Temperature Profiles in the Unstable Atmospheric Surface Layer, Journal of applied meteorology, 9, 857–861, https://doi.org/10.1175/1520-0450(1970)009⟨0857:TMROWS⟩2.0.CO;2, 1970.

Peña, A., Gryning, S.-E., and Hasager, C. B.: Measurements and Modelling of the Wind Speed Profile in the Marine Atmospheric Boundary Layer, Boundary-Layer Meteorology, 129, 479–495, https://doi.org/10.1007/s10546-008-9323-9, 2008.

Pichault, M., Vincent, C., Skidmore, G., and Monty, J.: Short-Term Wind Power Forecasting at the Wind Farm Scale Using Long-Range Doppler LiDAR, Energies, 14, 2663, https://doi.org/10.3390/en14092663, 2021a.

Pichault, M., Vincent, C., Skidmore, G., and Monty, J.: Characterisation of intra-hourly wind power ramps at the wind farm scale and associated processes, Wind Energy Science, 6, 131–147, https://doi.org/10.5194/wes-6-131-2021, 2021b.

Pinson, P., Madsen, H., Nielsen, H. A., Papaefthymiou, G., and Klöckl, B.: From probabilistic forecasts to statistical scenarios of short-term wind power production, Wind Energy, 12, 51–62, https://doi.org/10.1002/we.284, 2009.

Potisomporn, P. and Vogel, C. R.: Spatial and temporal variability characteristics of offshore wind energy in the United Kingdom, Wind Energy, 25, 537–552, https://doi.org/10.1002/we.2685, 2021.

Rechsteiner, R.: German energy transition (Energiewende) and what politicians can learn for environmental and climate policy., Clean Technologies and Environmental Policy, 23, 305–342, https://doi.org/10.1007/s10098-020-01939-3, 2021.

Rott, A., Schneemann, J., Trabucchi, D., Trujillo, J.-J., and Kühn, M.: Accurate deployment of long range scanning lidar on offshore platforms by means of sea surface leveling, available at: http://windtechconferences.org/wp-content/uploads/2018/01/Windtech2017_AnRott-Poster.pdf, last access: 15 July 2019, 2017.

Rott, A., Doekemeijer, B., Seifert, J. K., van Wingerden, J.-W., and Kühn, M.: Robust active wake control in consideration of wind direction variability and uncertainty, Wind Energy Science, 3, 869–882, https://doi.org/10.5194/wes-3-869-2018, 2018.

Rott, A., Petrović, V., and Kühn, M.: Wind farm flow reconstruction and prediction from high frequency SCADA Data, Journal of Physics: Conference Series, 1618, 062 067, https://doi.org/10.1088/1742-6596/1618/6/062067, 2020.

Rott, A., Schneemann, J., Theuer, F., Trujillo Quintero, J. J., and Kühn, M.: Alignment of scanning lidars in offshore wind farms, Wind Energy Science, 7, 283–297, https://doi.org/10.5194/wes-7-283-2022, 2022.

Saint-Drenan, Y.-M., Hagemann, S., Lange, B., and Tambke, J.: Uncertainty in the vertical extrapolation of the wind speed due to the measurement accuracy of the temperature difference, European Wind Energy Science Conference and Exhibition, Marseille, France, 2009.

Sanz Rodrigo, J., Cantero, E., García, B., Borbón, F., Irigoyen, U., Lozano, S., Fernandes, P., and Chávez, R.: Atmospheric stability assessment for the characterization of offshore wind condition, Journal of Physics: Conference Series, 625, 012 044, https://doi.org/10.1088/1742-6596/625/1/012044, 2015.

Scharff, R.: Design of Electricity Markets for Efficient Balancing of Wind Power Generation, Ph.D. thesis, KTH, Elektriska energisystem, Stockholm, Sweden, 2015.

Scheuerer, M.: Probabilistic quantitative precipitation forecasting using Ensemble Model Output Statistics, Quarterly Journal of the Royal Meteorological Society, 140, 1086–1096, https://doi.org/10.1002/qj.2183, 2014.

Schlipf, D.: Lidar-assisted control concepts for wind turbines, Ph.D. thesis, University of Stuttgart, Stuttgart, Germany, 2016.

Schlipf, D., Schlipf, D. J., and Kühn, M.: Nonlinear model predictive control of wind turbines using LIDAR, Wind Energy, 16, 1107–1129, https://doi.org/10.1002/we.1533, 2013.

Schneemann, J., Rott, A., Dörenkämper, M., Steinfeld, G., and Kühn, M.: Cluster wakes impact on a far-distant offshore wind farm's power, Wind Energy Science, 5, 29–49, https://doi.org/10.5194/wes-5-29-2020, 2020.

Schneemann, J., Theuer, F., Rott, A., Dörenkämper, M., and Kühn, M.: Offshore wind farm global blockage measured with scanning lidar, Wind Energy Science, 6, 521–538, https://doi.org/10.5194/wes-2020-124, 2021.

Schroeder, J., Hirth, B., and Guynes, J.: Final Technical Report: The Incubation of Next-Generation Radar Technologies to Lower the Cost of Wind Energy, https://doi.org/10.2172/1364776, 2017.

Schuhen, N., Thorarinsdottir, T. L., and Gneiting, T.: Ensemble Model Output Statistics for Wind Vectors, Monthly Weather Review, 140, 3204 – 3219, https://doi.org/10.1175/MWR-D-12-00028.1, 2012.

Sibson, R.: Interpreting Multivariate Data, chap. A brief description of natural neighbour interpolation, pp. 21–36, Chichester, New York : John Wiley and Sons, 1981.

Simley, E., Fleming, P., Girard, N., Alloin, L., Godefroy, E., and Duc, T.: Results from a wake-steering experiment at a commercial wind plant: investigating the wind speed dependence of wake-steering performance, Wind Energy Science, 6, 1427–1453, https://doi.org/10.5194/wes-6-1427-2021, 2021.

Smith, S. D.: Wind Stress and Heat Flux over the Ocean in Gale Force Winds, Journal of Physical Oceanography, 10, 709–726, https://doi.org/10.1175/1520-0485(1980)010⟨0709:WSAHFO⟩2.0.CO;2, 1980.

Späth, S., von Bremen, L., Junk, C., and Heinemann, D.: Time-consistent calibration of short-term regional wind power ensemble forecasts, Meteorologische Zeitschrift, 24, 381–392, https://doi.org/10.1127/metz/2015/0664, 2015.

Spodniak, P., Ollikka, K., and Honkapuro, S.: The impact of wind power and electricity demand on the relevance of different short-term electricity markets: The Nordic case, Applied Energy, 283, 116 063, https://doi.org/10.1016/j.apenergy.2020.116063, 2021.

Stull, R.: Atmospheric Boundary Layer, chap. 18, pp. 687–722, Springer Netherlands, https://doi.org/10.1007/978-94-009-3027-8, 2017.

Sun, J., Flicker, D. W., and Lilly, D. K.: Recovery of Three-Dimensional Wind and Temperature Fields from Simulated Single-Doppler Radar Data, Journal of Atmospheric Sciences, 48, 876–890, https://doi.org/10.1175/1520-0469(1991)048⟨0876:ROTDWA⟩2.0.CO;2, 1991.

Sweeney, C., Bessa, R. J., Browell, J., and Pinson, P.: The future of forecasting for renewable energy, WIREs Energy and Environment, 9:e365, https://doi.org/10.1002/wene.365, 2019.

Taylor, G. I.: The Spectrum of Turbulence, Proceedings of the Royal Society of London. Series A - Mathematical and Physical Sciences, 164, 476–490, https://doi.org/10.1098/rspa.1938.0032, 1938.

Theuer, F., van Dooren, M. F., von Bremen, L., and Kühn, M.: On the accuracy of a logarithmic extrapolation of the wind speed measured by horizontal lidar scans, Journal of Physics: Conference Series, 1618, 032 043, https://doi.org/10.1088/1742-6596/1618/3/032043, 2020a.

Theuer, F., van Dooren, M. F., von Bremen, L., and Kühn, M.: Minute-scale power forecast of offshore wind turbines using single-Doppler long-range lidar measurements, Wind Energy Science, 5, 1449–1468, https://doi.org/10.5194/wes-5-1449-2020, 2020b.

Theuer, F., van Dooren, M. F., von Bremen, L., and Kühn, M.: Lidar-based minute-scale offshore wind speed forecasts analysed under different atmospheric conditions, Meteorologische Zeitschrift, 31, 13–29, https://doi.org/10.1127/metz/2021/1080, 2021.

Theuer, F., Rott, A., Schneemann, J., von Bremen, L., and Kühn, M.: Observer-based power forecast of individual and aggregated offshore wind turbines, Wind Energy Science, 7, 2099–2116, https://doi.org/10.5194/wes-7-2099-2022, 2022a.

Theuer, F., Schneemann, J., van Dooren, M. F., von Bremen, L., and Kühn, M.: Hybrid use of an observer-based minute-scale power forecast and persistence, Journal of Physics: Conference Series, 2265, 022 047, https://doi.org/10.1088/1742-6596/2265/2/022047, 2022b.

Thorarinsdottir, T. L. and Gneiting, T.: Probabilistic forecasts of wind speed: ensemble model output statistics by using heteroscedastic censored regression, Journal of the Royal Statistical Society: Series A (Statistics in Society), 173, 371–388, https://doi.org/10.1111/j.1467-985X.2009.00616.x, 2010.

Torres, J., García, A., Blas, M. D., and Francisco, A. D.: Forecast of hourly average wind speed with ARMA models in Navarre (Spain), Solar Energy, 79, 65–77, https://doi.org/10.1016/j.solener.2004.09.013, 2005.

Ulazia, A., Nafarrate, A., Ibarra-Berastegi, G., Sáenz, J., and Carreno-Madinabeitia, S.: The Consequences of Air Density Variations over Northeastern Scotland for Offshore Wind Energy Potential, Energies, 12, 2635, https://doi.org/10.3390/en12132635, 2019.

Vali, M.: Model predictive control framework for power maximisation and active power control with load equalisation of wind farms, Ph.D. thesis, University of Oldenburg, Oldenburg, Germany, 2019.

Valldecabres, L., Nygaard, N., Vera-Tudela, L., von Bremen, L., and Kühn, M.: On the Use of Dual-Doppler Radar Measurements for Very Short-Term Wind Power Forecasts, Remote Sensing, 10, 1701, https://doi.org/10.3390/rs10111701, 2018a.

Valldecabres, L., Peña, A., Courtney, M., von Bremen, L., and Kühn, M.: Very short-term forecast of near-coastal flow using scanning lidars, Wind Energy Science, 3, 313–327, https://doi.org/10.5194/wes-3-313-2018, 2018b.

Valldecabres, L., von Bremen, L., and Kühn, M.: Minute-Scale Detection and Probabilistic Prediction of Offshore Wind Turbine Power Ramps using Dual-Doppler Radar, Wind Energy, 23, 1–23, https://doi.org/10.1002/we.2553, 2020.

Van Dooren, M. F., Trabucchi, D., and Kühn, M.: A Methodology for the Reconstruction of 2D Horizontal Wind Fields of Wind Turbine Wakes Based on Dual-Doppler Lidar Measurements, Remote Sensing, 8, 809, https://doi.org/10.3390/rs8100809, 2016.

Van Wijk, A., Beljaars, A., Holtslag, A., and Turkenburg, W.: Evaluation of stability corrections in wind speed profiles over the North Sea, Journal of Wind Engineering and Industrial Aerodynamics, 33, 551–566, https://doi.org/10.1016/0167-6105(90)90007-Y, 1990.

Vignaroli, A., Svensson, E., Courtney, M., Vasiljevic, N., Lea, G., Wagner, R., and Nygaard, N. G.: How accurate is the BEACon radar?, Wind Europe Conference and Exhibition, Amsterdam, Netherlands, 2017.

Werner, C.: Lidar: Range-Resolved Optical Remote Sensing of the Atmosphere, chap. 12 - Doppler Wind Lidar, pp. 325–354, Springer New York, New York, NY, https://doi.org/10.1007/0-387-25101-4_12, 2005.

Wilks, D.: Statistical Methods in the Atmospheric Sciences: An Introduction, chap. 8 - Forecast Verification, pp. 301–394, Academic Press, https://doi.org/10.1016/b978-0-12-385022-5.00008-7, 2011.

WindEurope: Wind energy in Europe - 2020 Statistics and the outlook for 2021-2025, Tech. rep., 2021.

Würth, I.: Minute-scale forecasting of wind power using a long-range lidar - PhD presentation, https://doi.org/10.5281/zenodo.5767778, 2021.

Würth, I., Ellinghaus, S., Wigger, M., J Niemeier, M., Clifton, A., and W Cheng, P.: Forecasting wind ramps: can long-range lidar increase accuracy?, Journal of Physics: Conference Series, 1102, 012 013, https://doi.org/10.1088/1742-6596/1102/1/012013, 2018.

Würth, I., Valldecabres, L., Simon, E., Möhrlen, C., Uzunoğlu, B., Gilbert, C., Giebel, G., Schlipf, D., and Kaifel, A.: Minute-Scale Forecasting of Wind Power - Results from the Collaborative Workshop of IEA Wind Task 32 and 36, Energies, 12, 712, https://doi.org/10.3390/en12040712, 2019.

Xin, L. and Reuter, G. W.: VVP Technique Applied to an Alberta Storm, Journal of Atmospheric and Oceanic Technology, 15, 587–592, https://doi.org/10.1175/1520-0426(1998)015⟨0587:VTATAA⟩2.0.CO;2, 1998.

Zhao, J., Duan, Y., and Liu, X.: Uncertainty Analysis of Weather Forecast Data for Cooling Load Forecasting Based on the Monte Carlo Method, Energies, 11, 1900, https://doi.org/10.3390/en11071900, 2018.

Zhou, K., Cherukuru, N., Sun, X., and Calhoun, R.: Wind Gust Detection and Impact Prediction for Wind Turbines, Remote Sensing, 10, 514, https://doi.org/10.3390/rs10040514, 2018.

Zieher, M., Lange, M., and Focken, U.: Variable Renewable Energy Forecasting - Integration into Electricity Grids and Markets - A Best Practice Guide, VRE Discussion Series, 2015.

List of Publications

Publications on which this thesis is based

Journal peer-reviewed publications

- Theuer, F., van Dooren, M. F., von Bremen, L., and Kühn, M.: Minute-scale power forecast of offshore wind turbines using long-range single-Doppler lidar measurements, Wind Energy Science, 5, 1449-1468, https://doi.org/10.5194/wes-5-1449-2020, 2020.

  Authors contribution: *FT performed the main research and wrote the paper. MFvD contributed to the scientific discussion, the outline and the review of the manuscript. LvB and MK supervised the research, contributed to the scientific discussion, the research concept, and the outline and thorough review of the manuscript.*

  The content of this paper is reproduced in Chapter 2.

- Theuer, F., van Dooren, M. F., von Bremen, L., and Kühn, M.: Lidar-based minute-scale offshore wind speed forecasts analysed under different atmospheric conditions, Meteorologische Zeitschrift, 31, 13–29, https://doi.org/10.1127/metz/2021/1080, 2021.

  Authors contribution: *FT conducted the main research and wrote the manuscript. MFvD contributed to the scientific discussion, the structure of the paper and its detailed review. LvB and MK supervised the work, contributed to the scientific discussion and the structure of the paper and thoroughly reviewed the manuscript.*

  The content of this paper is reproduced in Chapter 3.

- Theuer, F., Rott, A., Schneemann, J., von Bremen, L., and Kühn, M.: Observer-based power forecast of individual and aggregated offshore wind turbines, Wind Energy Science, 7, 2099-2116, https://doi.org/10.5194/wes-7-2099-2022, 2022.

Authors contribution: *FT conducted the main research and wrote the manuscript. JS conducted the measurement campaign, supported lidar data analysis, contributed to the scientific discussion and provided extensive feedback in the form of manuscript reviews. AR supported the development of the observer-based forecast, gave extensive feedback on copula and calibration methods and their mathematical formulation and reviewed the manuscript. LvB and MK supervised the work, contributed to the scientific discussion and the structure of the paper, and thoroughly reviewed the manuscript.*

The content of this paper is reproduced in Chapter 4.

Conference peer-reviewed publications

- Theuer, F., Schneemann, J., van Dooren, M. F., von Bremen, L., and Kühn, M.: Hybrid use of an observer-based minute-scale power forecast and persistence, Journal of Physics: Conference Series, 2265, 022047, https://doi.org/10.1088/1742-6596/2265/2/022047, 2022.

  Authors contribution: *FT performed the main research and wrote the paper. JS conducted the measurement campaign, supported lidar data analysis, contributed to the scientific discussion and reviewed the manuscript. MFvD supported the development of the forecasting methodology, contributed to the scientific discussion and reviewed the paper. LvB and MK supervised the work, contributed to the scientific discussion and the outline of the paper and thoroughly reviewed the manuscript.*

  The content of this paper is reproduced in Chapter 5.

Other journal peer-reviewed publications

- Rott, A., Schneemann, J., Theuer, F., Trujillo Quintero, J. J., and Kühn, M.: Alignment of scanning lidars in offshore wind farms, Wind Energy Science, 7, 283–297, https://doi.org/10.5194/wes-7-283-2022, 2022.

  Authors contribution: *AR initiated and directed the research, developed the methods, prepared the computational scripts, analysed the measured data, was heavily involved in funding acquisition and research discussion, prepared the figures, and was lead author of the article. JS assisted with data provision and data processing, as well as derivation of the methods, and provided extensive feedback in several reviews. FT assisted in the development of the computational scripts, verified the*

calculations, provided support in countless discussions and gave extensive feedback in several interactions. JJTQ supported with his rich experience of lidar systems, was instrumental in drafting the research question and helped with extensive review. MK was instrumental in acquiring funding, supervised the research, and provided support with valuable comments and good advice.

- Schneemann, J., Theuer, F., Rott, A., Dörenkämper M., Kühn, M.: Offshore wind farm global blockage measured with scanning lidar, Wind Energy Science, 6, 521–538, https://doi.org/10.5194/wes-6-521-2021, 2021.

  Authors contribution: *JS initiated the research; performed the measurement campaign; was heavily involved in the funding acquisition and the research discussion; wrote Sects. 1, 2.1, 2.2, 2.5.4, 4 and 5; and prepared Figs. 1, 2 and 3. FT performed the data analysis; was heavily involved in the research discussion; wrote Sects. 2.3, 2.4, 2.5 and 3; and made Figs.4, 5, 6, 7 and 8. AR was heavily involved in the research discussion and supported the writing of the paper. MD initiated the research and was heavily involved in the funding acquisition and the research discussion. MK was heavily involved in the funding acquisition and supervised the research. All authors contributed intensively to an internal review.*

Other conference peer-reviewed publications

- Ortensi, M., Theuer, F., and Kühn, M.: Analysis of the effects of scanning trajectory parameters on minute-scale lidar forecasting, Journal of Physics: Conference Series, 2265, 022002, https://doi.org/10.1088/1742-6596/2265/2/022002, 2022.

- Theuer, F., van Dooren, M. F., von Bremen, L., and Kühn, M.: On the accuracy of a logarithmic extrapolation of the wind speed measured by horizontal lidar scans, Journal of Physics: Conference Series, 1618, 032 043, https://doi.org/10.1088/1742-6596/1618/3/032043, 2020.

Conference presentations

- Ortensi, M., Theuer, F., Kühn, M.: Optimisation of long-range lidar trajectories for wind speed forecast using large eddy simulations (LES), 17th EAWE PhD Seminar, Porto, Portugal, 2021 (Oral presentation).

- Ortensi, M., Theuer, F., and Kühn, M.: Analysis of the effects of scanning trajectory parameters on minute-scale lidar forecasting, Science of making Torque from Wind 2022, Delft, The Netherlands, 2022 (Oral presentation).
- Schneemann, J., Theuer, F., Rott, A., Dörenkämper, M., Steinfeld, G., Kühn, M.: Measuring large scale offshore wind farm effects with scanning lidar, RAVE Workshop 2021, online event, 2021 (Oral presentation).
- Schneemann, J., Theuer, F., Rott, A., Centurelli, G., Dörenkämper, M., Steinfeld, G., Kühn, M.: Large scale offshore wind farm effects measured with scanning lidar, Wind Energy Science Conference 2021 web conference, Hannover, Germany, 2021 (Oral presentation).
- Schneemann, J., Theuer, F., Rott, A., Centurelli, G., Dörenkämper, M., Steinfeld, G., Kühn, M.: Assessing large scale offshore wind farm effects with scanning lidar, EERA JP Wind & SETWind Annual Event 2021, online event, 2021 (Oral presentation).
- Theuer, F., Valldecabres, L., von Bremen, L., Kühn, M.: Very short-term forecast of wind speed and power at the offshore wind farm Global Tech I using horizontal PPI lidar scans, Wind Energy Science Conference, Cork, Ireland, 2019 (Oral presentation).
- Theuer, F., von Bremen, L., Kühn, M.: Very short-term probabilistic wind speed and power forecasts based on lidar measurements at the offshore wind farm Global Tech I, European Meteorological Society Annual Meeting 2019, Lynbgy, Denmark, 2019 (Oral presentation).
- Theuer, F., van Dooren, M.F., von Bremen, L., Kühn, M.: Kürzestfrist-Prognose von Windgeschwindigkeit und Leistung des Offshore Windparks Global Tech I mittels langreichweitiger Lidarmessungen, 11. Industrie- und Forschungsplattform Prognose, Kassel, Germany, 2019 (Oral presentation).
- Theuer, F., van Dooren, M.F., von Bremen, L., Kühn, M.: On the accuracy of a logarithmic extrapolation of the wind speed measured by horizontal lidar scans, Science of making Torque from Wind 2020 Web-Conference, Delft, The Netherlands, 2020 (Poster presentation).
- Theuer, F., van Dooren, M.F., von Bremen, L., Kühn, M.: Lidar-based minute-scale wind speed and power forecast of free-stream and wake-influenced offshore

wind turbines, Wind Energy Science Conference 2021 web conference, Hannover, Germany, 2021 (Oral presentation).

- Theuer, F., Schneemann, J., Ortensi, M., Kühn, M.: WindRamp: Observer-based minute-scale power forecasts at the offshore wind farm Nordergründe – Measurement campaign and forecasting methodology, RAVE Workshop 2022, online event, 2022 (Oral presentation).

- Theuer, F., Schneemann, J., van Dooren, M. F., von Bremen, L., and Kühn, M.: Hybrid use of an observer-based minute-scale power forecast and persistence, Science of making Torque from Wind 2022, Delft, The Netherlands, 2022 (Oral presentation).

Acknowledgements

First of all, I would like to thank my supervisor Prof. Dr. Martin Kühn for supporting my research, his encouragement, guidance and feedback on this path. I am also thankful to Prof. Dr. Charlotte Bay Hasager for reviewing this thesis. Thanks to Lueder von Bremen for his valuable feedback and support throughout my PhD.

I thank my colleagues at ForWind in the Wind Energy Systems group for the nice working environment and the positive attitude that got us through the pandemic so smoothly. I am in particular grateful to Jörge and Stephan for executing all those measurement campaigns so perfectly, to Andreas for patiently answering all my Maths-related questions and to Marijn for his reliable support. Thanks to all of you for interesting discussions and collaborations, for many thorough reviews of many manuscript drafts, and for your support on numerous smaller and larger issues along the way. I also thank Arjun, Gerald, Lilén, Marcos, Hauke, Janna, Martin, Laura, Irene and Dagmar.

I am thankful to the German Federal Environmental Foundation (DBU) for funding my work within the scope of their PhD scholarship program (Grant Nr. 20018/582). I enjoyed the exchange within the DBU network and in particular within the *Promotionskolleg Umwelt-soziale Fragen der Energiewende*. I appreciate the funding of the German Federal Ministry for Economic Affairs and Climate Action on the basis of a decision by the German Bundestag in scope of the projects OWP Control (Ref. Nr. 0324131A), WIMS-Cluster (Ref. Nr. 0324005) and WindRamp (Ref. Nr. 03EE3027A). I acknowledge the wind farm operator Global Tech I Offshore Wind GmbH for providing SCADA data and thank them for supporting my work. I thank the Met Office for making the OSTIA data set available.

Finally, I am deeply thankful to my parents, and my sisters Nele and Gesa for their constant and loving support and encouragement. Thank you to Jannick for being there every step on the way and for all our adventures. And thanks to my friend Marie.

Curriculum Vitae

Personal:

Name	Frauke Theresa Theuer
Place of birth	Osnabrück, Germany

Education:

12/2018 - 04/2022	PhD student at ForWind, University of Oldenburg
01/2019 - 12/2021	PhD scholarship holder, German Federal Environmental Foundation (DBU)
10/2016 - 10/2018	M. Sc. Engineering Physics, University of Oldenburg, Germany
08/2015 - 01/2016	ERASMUS exchange, Lund university, Sweden
10/2013 - 09/2016	B. Eng. Engineering Physics, University of Oldenburg, Germany

Scientific Experience:

12/2018 - today	Research assistant, Wind Energy Systems, ForWind - Center for Wind Energy Research
02/2018 - 09/2018	Master student, WRD Management Support GmbH (ENERCON Group), Bremen, Germany

Erklärung

Ich erkläre hiermit, dass

- (a) eine Promotion zur Dr. rer. nat. angestrebt wird,
- (b) ich diese Arbeit selbständig verfasst und nur die angegebenen Hilfsmittel benutzt habe, und dass die Arbeit in Teilen bereits veröffentlicht bzw. zur Veröffentlichung eingereicht wurde,
- (c) diese Dissertation weder in ihrer Gesamtheit noch in Teilen einer anderen Hochschule zur Begutachtung in einem Promotionsverfahren vorgelegen hat.

Oldenburg, den 29.11.2022

.....

Frauke Theresa Theuer